COO-2245-29 TR

INTERFEROMETRIC INVESTIGATION OF TURBULENTLY FLUCTUATING TEMPERATURE IN AN LMFBR OUTLET PLENUM GEOMETRY

by

Ralph G. Bennett

and

Michael W. Golay

ERDA Research and Development

Contract AT(11-1)-2245

U.S. Energy Research and Development Administration

DISCLAIMER

INTERFEROMETRIC INVESTIGATION OF TURBULENTLY FLUCTUATING TEMPERATURE IN AN LMFBR OUTLET PLENUM GEOMETRY

by

Ralph Gregory Bennett

and

Michael W. Golay

A novel optical technique is developed for the measurement of turbulently fluctuating temperature in a transparent fluid flow. The technique employs a Mach-Zehnder interferometer of extremely short field and a simple photoconductive diode detector. The system produces a nearly linear D.C. electrical analog of the turbulent temperature fluctuations in a small, 1 mm^3 volume. The frequency response extends well above 2500 Hz, and can be improved by the choice of a more sophisticated photodetector.

The turbulent sodium mixing in the ANL 1/15-scale FFTF outlet plenum is investigated with a scale model outlet mixing plenum, using flows of air. The scale design represents a cross section of the ANL outlet plenum, so that the average recirculating flow inside the test cell is two dimensional. The range of the instrument is 120 ^{o}F above the ambient air temperature. The accuracy is generally +5 ^{o}F, with most of the error due to noise originating from building vibrations and room noise. The power spectral density of the fluctuating temperature has been observed experimentally at six different stations in the flow. A strong 300 Hz component is generated in the inlet region, which decays as the flow progresses along streamlines. The effect of the inlet Reynolds number and the temperature difference between the inlet flows on the power spectral density has also been investigated. Traces of the actual fluctuating temperature are included for the six stations.

TABLE OF CONTENTS

ACKNOWLEDGEMENTS

This research was conducted as part of the "Coolant Mixing in LMFBR Rod Bundles Project," contract AT(11-1)-2245 sponsored by the Energy Research and Development Administration. The authors gratefully acknowledge this support.

The first author gives special thanks to Mike Kelly of the MIT Physics Department for his help in the selection of the proper optical components for this work. The author would also like to thank Yi Bin Chen and Joe Chan of the MIT Nuclear Engineering Department for their unbounded patience.

NOMENCLATURE

D	diameter of the variable aperture that determines the beam diameter; 0.5 mm
I	intensity of light transmitted by the interferometer
I_o	the maximum interferometer throughput, expressed as an intensity
I_{max}	maximum value of I; equal to I_o
I_{min}	minimum value of I
L	test cell thickness inside; 0.64 cm
m	order of interference; an integer
n	index of refraction
$n(s)$	index of refraction at the path length, s
n_{test}	index of refraction in the test cell
n_{std}	index of refraction of the ambient air
R	distance from the test cell to the recombination intersection; about 5 cm
t	time; sec
$T(\underline{x},t)$	fluctuating temperature at point $\underline{x}$; ^oC
$v_i(\underline{x},t)$	fluctuating velocity in the $\underline{x}_i$ direction at point $\underline{x}$; cm/sec
$V(t)$	temperature analog; volts
$\mathcal{V}$	fringe contrast; assumes a value between 0 and 1
$\langle \ldots \rangle$	averaged in time
$\delta\theta$	angle of deflection of the test beam; radians
δD	separation distance of the two beams at the recombination intersection; mm
δx	extra distance traveled by the test beam; cm

ϵ_{Hij} eddy diffusivity of heat, a second rank tensor; cm^2/sec

λ_o wavelength of laser beam; 6328×10^{-8} cm

1. INTRODUCTION

1.1 Purpose and Scope of the Investigation

The conservative design of nuclear reactor structural components, guarding against thermal transients in the upper mixing plenum of liquid-metal-cooled fast breeder-reactors (LMFBR's), requires a predictive knowledge of the turbulent sodium mixing. Specifically, the eddy diffusivity of heat, ϵ_{Hij}:

$$\epsilon_{Hij}(\underline{x}) \equiv \langle T(\underline{x},t)v_i(\underline{x},t)\rangle \Big/ \langle \partial T(\underline{x},t)/\partial x_j \rangle \qquad (1.1)$$

embodies the turbulent mixing that lessens thermal shock on the structural components. The eddy diffusivity of heat is often expediently defined in terms of conveniently known quantities[1] that fall short of describing the true mixing. A calculation of the eddy diffusivity of heat from Eq. 1.1 demands the mapping out of the turbulently fluctuating temperature and velocity for any particular flow geometry.

This work approaches the LMFBR turbulent sodium mixing problem with a transparent fluid scale-model; measuring the fluctuating temperature with a novel optical method. The fluctuating velocity was not measured in this work, but could easily be found with standard Laser-Doppler Anemometry techniques. This combination of optical systems could achieve the extremely fast time response needed to faithfully

follow the turbulent fluctuations, while not intruding into the flow and disturbing its fine structure.

The optical method for temperature measurements implements a Mach-Zehnder interferometer[2] of extremely short field (about 0.5 mm) in real time. Due to the short field, and other considerations, the instrument defines a temperature sensitive volume of 1.25 mm^3. The system produces a nearly linear DC electrical analog of the fluctuating temperature over most of the 120 ^{o}F (67 ^{o}C) range of the instrument. The time response is ultimately limited only by the choice of the photodetector--which is greater than 10 kHz for the inexpensive detector used in this work. The average flow pattern in the scale model design is restricted to two dimensions to facilitate the temperature measurements. The average temperature is not currently available from the optical technique. The average temperature is measured mechanically at a symmetric, but remote, station in the flow.

The experiments reported seek to establish the capabilities of the technique, and to visualize the transport and mixing of heat in the scale model in preparation for future investigations. The characterization of the turbulent temperature proceeds with photographic studies of the electrical analog, leading to the computation of an autocorrelation of the temperature. Fourier analysis of the temperature signal yields curves of the power spectral density of the

fluctuating temperature.

1.2 Results and Importance of the Work

The results show the method to be a potentially accurate and appropriate companion to Laser-Doppler Anemometry for combined velocity and temperature correlations. The accuracy of the temperature analog in this work is about ± 5 °F (3 °C). However, this is not the ultimate accuracy of the technique. A mapping out of the temperature analog and its power spectral density at six stations in the flow illustrates their strong position dependence in the test cell. The temperature upset between the inlet flows does not measurably affect the turbulent mixing in the cell at the low Reynolds numbers ($Re \leq 10\ 000$) investigated. The experiments did not extend to the high Reynolds number values which would be observed in the LMFBR outlet plenum.

1.3 Alternate Methods and Related Work

Several of the established methods for fast response temperature measurements in liquid sodium, and for alternate optical temperature measurement methods are surveyed here. Fast response temperature measurements in high temperature liquid sodium is a developing art. Hayes[3] reports that the conventional thermocouples for liquid sodium of 0.5 mm diameter can achieve about 50 Hz response and good accuracy.

Smaller diameter thermocouples are lacking in the required ruggedness and strength. The more promising eddy current probes--which measure the liquid sodium electrical resistivity by an electromagnetic induction method--of Hughes[4], extend the frequency response to nearly 1 kHz. The effects of impurities and gases in the flows on the probes are not well known.

For measurements in alternate fluid mock-ups, thermocouples can draw on a well-developed art of their own. The careful preparation and electronic augmentation of platinum wire thermocouples with diameters as small as 0.25 microns by LaRue, Deaton, and Gibson[5], extends their frequency response to 10 kHz in air flows. Of course, all of the measurements discussed above will disturb the fluid flows that they measure.

Two recently developed optical temperature measurement techniques that are very different from the one developed in this work are described here. Both methods, like the one in this work, are essentially restricted to two dimensional measurements. Oliver and Stott[6] have selected an appropriate thermometric solution--one whose absorbance of light at 520 nm varies linearly with temperature. The working fluid is aqueous 3,5 dinitro salicylic acid, which could compose the flowing fluid. An absorbance measurement at 520 nm will then coincide with the local fluid temperature. The frequency

response is not yet known.

A second method suggested for optical temperature measurements is the laser-Raman spectroscopy method of Hickman and Liang[7]. The absolute temperature is found from the rotational spectrum of the fluid at a point inside a laser cavity. The fluid must be a pure gas--air has too many overlapping rotational bands. The accuracy is limited to 3-8 ^{o}C (5-15 ^{o}F), and the results must be carefully sorted out by a computer.

The method in this work has been published nearly simultaneously by Bennett and Golay[8], and Miller, Hussmann, and McLaughlin.[9] The latter paper is not concerned with the measurement of turbulent fluid flows, but investigates the pulsed beta-ray heating of an aqueous system. It is interesting to note that the paper achieves a 5 megahertz frequency response simply by the choice of a more sophisticated photodetector.

2. METHODOLOGY

2.1 General View of the Technique

The index of refraction of air varies, most importantly, with its temperature and pressure. The variation is quite small, being about 1×10^{-6} per ^{o}C with temperature[10], and about 2×10^{-5} per psi with pressure.* The index of refraction of air is normally around unity, and so these variations are miniscule in comparison. Any direct observation of the effect of temperature or pressure on the index of refraction of air is a very serious task, with little hope of realization in real time.

In the wide class of instruments available for measuring the index of refraction, the refractometers, are a subset that measure only differences in the index of refraction between two media, the so-called differential refractometers.[11] In this work, the Mach-Zehnder interferometer[2] is used as a differential refractometer. The design of the experiments carried the responsibility for insuring that the temperature fluctuations always induced a much larger effect than the pressure fluctuations.

---

* This is the value of the derivative of the Biot and Arago formula[10] with respect to pressure at STP.

2.2 Mach-Zehnder Interferometer Applied to Temperature Measurements

2.2.1 Principle of the Mach-Zehnder Interferometer

The Mach-Zehnder interferometer is an important system for visualization and quantification of air flows, because of its simple geometry and straightforward principle of operation. The interferometer is idealized in Fig. 2.1. The incident monochromatic light ray divides in amplitude in the first beamsplitter; the rays reflect in their own mirrors, and recombine at the second beamsplitter. If the rays encounter different conditions in the two cells, their phases will generally differ, and they will interfere when recombined. All of the mirrors and beamsplitters are mutually parallel, and the two arms are of equal <u>geometrical</u> length. The <u>optical</u> path lengths experienced by the rays are governed by the refractive index as $\int_{OAB} n(S)\,dS$ or $\int_{OA'B} n(S)\,dS$. With ideal components, total destructive interference of the two rays occurs when the condition:[12]

$$\oint_{OABA'O} n(S)\,dS = \pm m\,\frac{\lambda_o}{2} \qquad (2.1)$$

is satisfied, where odd integer values of m are the "order of interference." The transmitted intensity generally obeys the relation:

$$I = I_o \cos^2\left\{\frac{\pi}{\lambda_o}\oint n(S)\,dS\right\} \qquad (2.2)$$

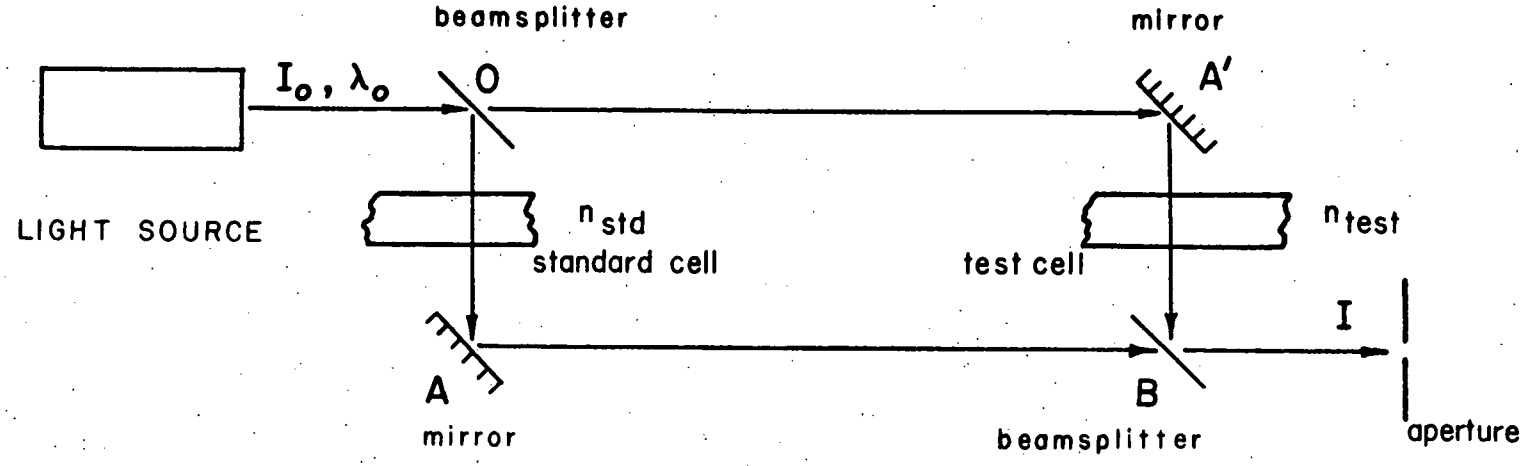

Fig. 2.1
MACH - ZEHNDER INTERFEROMETER

This result will govern the design of the test cell in Section 2.4.2.

2.2.2 Relaxation of the Exacting Geometry

The requirements on the geometry of the interferometer may be greatly relaxed. First, the mirrors and beamsplitters need not be mutually parallel. The most general Mach-Zehnder interferometer places the mirrors on the surface of a three-dimensional ellipsoid.[13] The shape of the ellipsoid is determined by assuming that the beamsplitters are at the foci, and a few particular vectors define the parameters necessary to define the surface. Second, the arms do not have to have the same geometrical length, due to the extremely long coherence length of the light source. In practice, these freedoms allow the interferometer to be aligned very quickly with little more than a cursory positioning of the four optical components in a rectangle on the bench.

2.2.3 Optical Components

The choice of the optical components shown in Fig. 2.1 is not subject to any stringent restrictions about quality or performance. The four central components--two mirrors and two beamsplitters--that form the interferometer naturally need to be optically flat, but only over the very small area of the laser beam (about 1 mm^2). The mirrors are $\lambda/4$ flat,

front-silvered plane mirrors. The beamsplitters are $\lambda/30$ (uncoated) fused silica wedged flats. The 1^{o} wedging of the two flat faces forces any back reflections out of the primary beam. The absence of any optical coatings results in the loss of fully 85 % of the laser output into stray reflections. In spite of this, the detector is suitably matched to the reduced laser throughput.

Additional optical components inside the interferometer are the plexiglass walls of the test assembly. Since the plexiglass is not optically flat, a slight variation of phase exists across the output beam. The variation is much less than one fringe over the 0.5 mm beam diameter, and it accounts for a small, yet observable, degradation of fringe contrast. In practice, this has no important effect on the results (see Section 3.1).

A second effect on the phase of the output laser beam originates from the small bubbles and hairline scratches in the plexiglass. Here, however, the phase variation across the output beam is so great that many finely spaced fringes are observed over the 0.5 mm diameter. These fringes, like any fringes, are simply a redistribution of electromagnetic energy into preferred directions. Concentrating all of the energy in the output beam before detection (illustrated in the next section) essentially integrates these particular fringes over an infinitely large area, and they produce no

noticeable effect on the results. The two effects mentioned here are most easily investigated by sending the output beam through a double convex lens, and forming an image for study, 1 ft (0.3 m) in diameter, on black paper about 10 ft (3 m) distant.

2.2.4 Output Intensity Detector

The output intensity detector features a few simple optical components, and an equally simple battery-powered circuit. The optical arrangement is sketched in Fig. 2.2. Only the central 0.5 mm diameter of the laser beam is admitted through the aperture. This fixes the field of the interferometer at 0.5 mm, with the implication that the instrument is sensitive to temperature in the flow only over this small diameter. The light is collected by a double convex lens, and focused on the photoconductive diode. The entire detection system rests on the optical bench, and the vibrations that it experiences are not large enough to deleteriously affect its operation.

The laser detection circuit is drawn in Fig. 2.3. An illustration of the detector characteristic is included on the left hand side of Fig. 2.4. The circuit normally develops an output between 0 and 10 volts. No experimental verification of the detector linearity is offered. The frequency response has been experimentally verified with a homemade

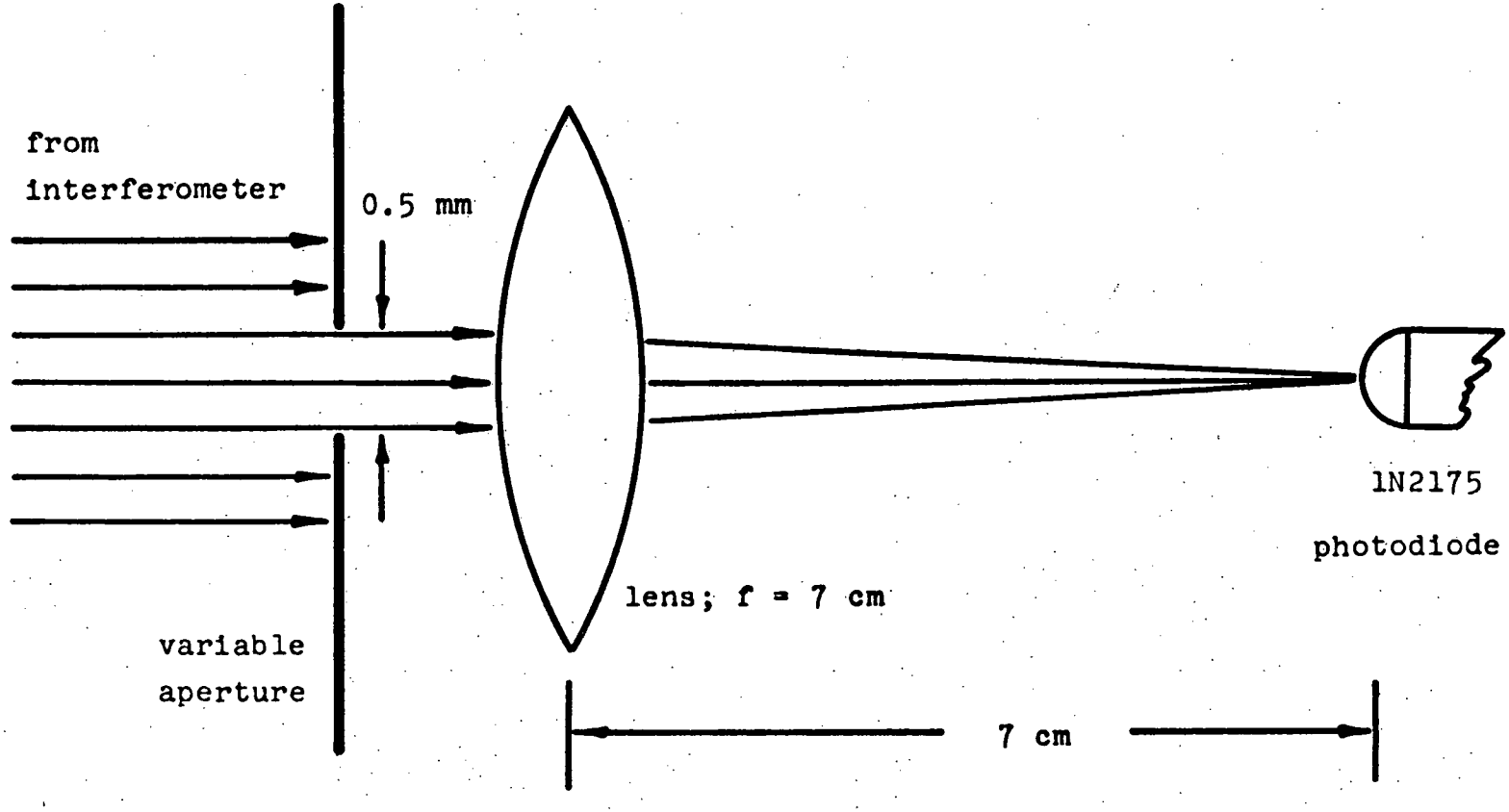

Fig. 2.2 Laser detection optics.

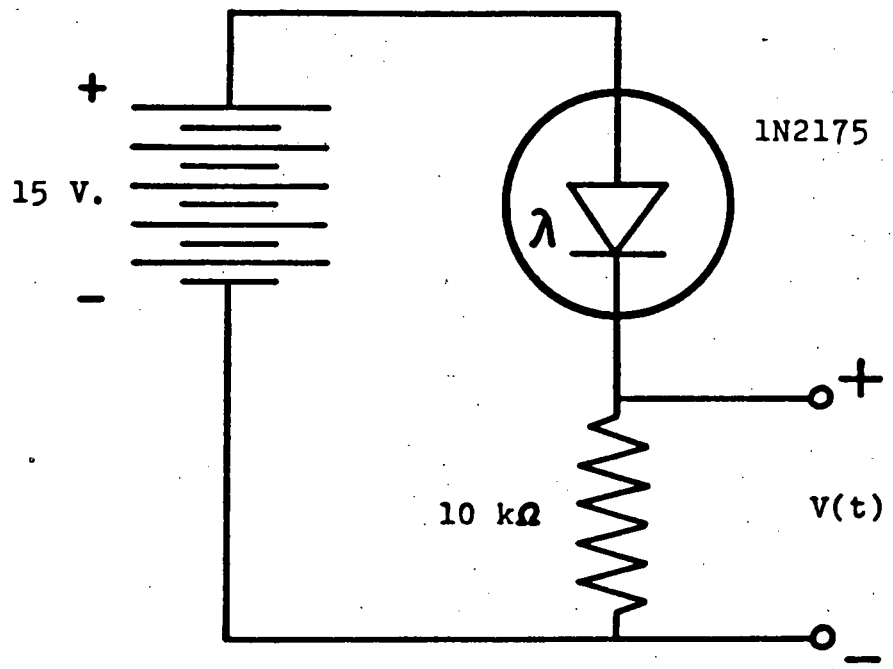

Fig. 2.3 Laser detection circuit; the 1N2175 is a photoconductive diode.

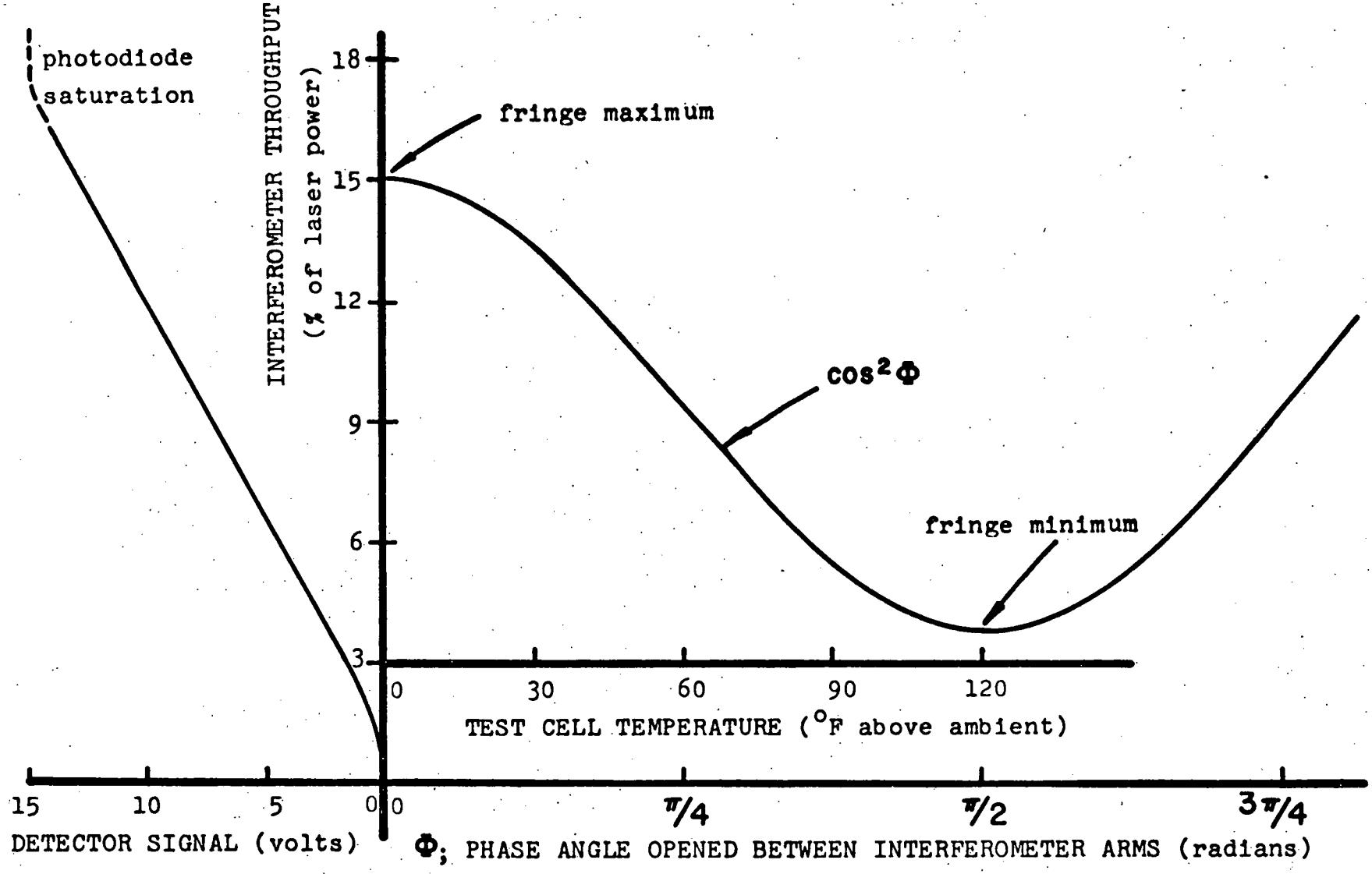

Fig. 2.4 Visualization of parameters for interferometric temperature measurements. Left: detector characteristic curve. Right: interferometer characteristic curve.

beam chopper to be at least 2 500 Hz. At 2 500 Hz, the circuit is able to accurately reproduce a 10 volt waveform corresponding to the covering and uncovering of the laser beam--with no noticeable signal distortion. The frequency response probably extends out considerably farther than 2 500 Hz, but this has not been verified.

2.2.5 Elimination of the Standard Cell

In practice, it is found that the standard cell of Fig. 2.1 may be omitted from the experiments entirely. The long coherence length of the laser[14] makes it unnecessary to compensate for the large delays in the wave trains that pass through the walls of the test cell. In this state the interferometer is said to be uncompensated.

2.2.6 Attenuation of Light in the Arms

Unmatched attenuation of the two laser beams in the arms will decrease the fringe contrast. An important source of constant attenuation in the test arm is the reflection of light off of the four air-plexiglass boundaries (due to the discontinuity of the index of refraction). The treatment of the detector voltage signal in Section 3.1 entirely surmounts this effect.

2.2.7 Schlieren Effects

The refraction of the laser beam in the test cell by

strong refractive index gradients normal to the beam will result in a misalignment of the interferometer. An approximate (yet conservative) solution of this situation serves to show when and what schlieren effects are important. Fig. 2.5 illustrates the important quantities. A gradient of the index of refraction, $\partial n/\partial y$, will bend the light ray through the angle:[15]

$$\delta\theta = \frac{L}{n}\frac{\partial n}{\partial y} \tag{2.3}$$

where $L \approx 0.25$ in. (0.64 cm), $n \approx 1$, and the gradient, $\partial n/\partial y$, can be split up for convenience as:

$$\frac{\partial n}{\partial y} = \frac{\partial n}{\partial T}\cdot\frac{\partial T}{\partial t}\cdot\frac{\partial t}{\partial y} \tag{2.4}$$

Because of this bending, the two effects illustrated in Figs. 2.6 and 2.7 are important. First, in Fig. 2.6, the bent ray must travel a longer path, by the amount:

$$\delta x = R(\sec\delta\theta - 1) \simeq \frac{R}{2}(\delta\theta)^2 \tag{2.5}$$

causing a fractional fringe shift:

$$\frac{\delta x}{\lambda_o/2} = \frac{R}{\lambda_o}(\delta\theta)^2 \tag{2.6}$$

Each 1 % of this fractional fringe shift corresponds roughly to an error of 1 ^{o}F in the signal. Limiting this fractional fringe shift to be less than 1 % requires:

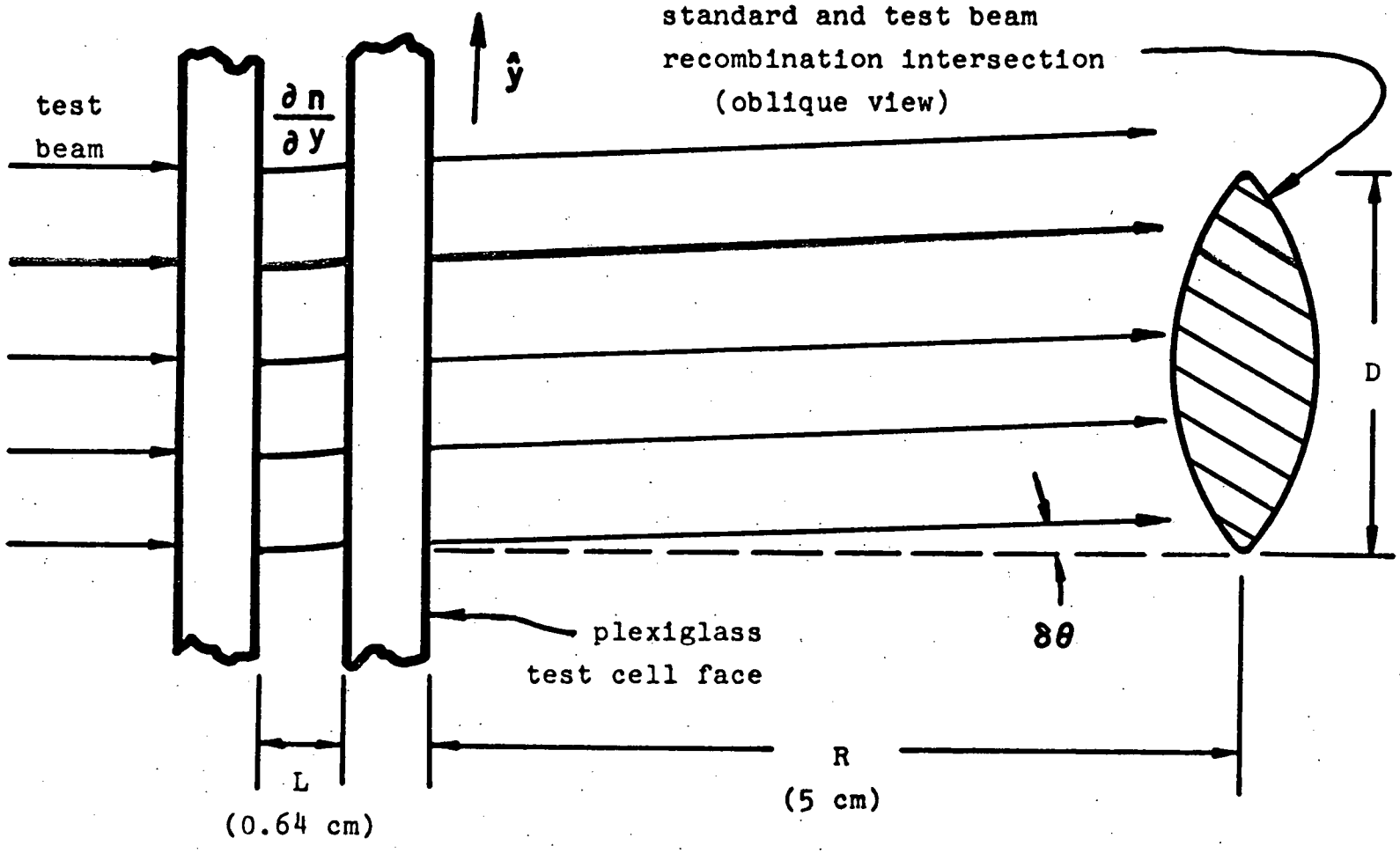

Fig. 2.5 Idealized geometry of schlieren effects. The test beam is bent by a refractive index gradient in the test cell.

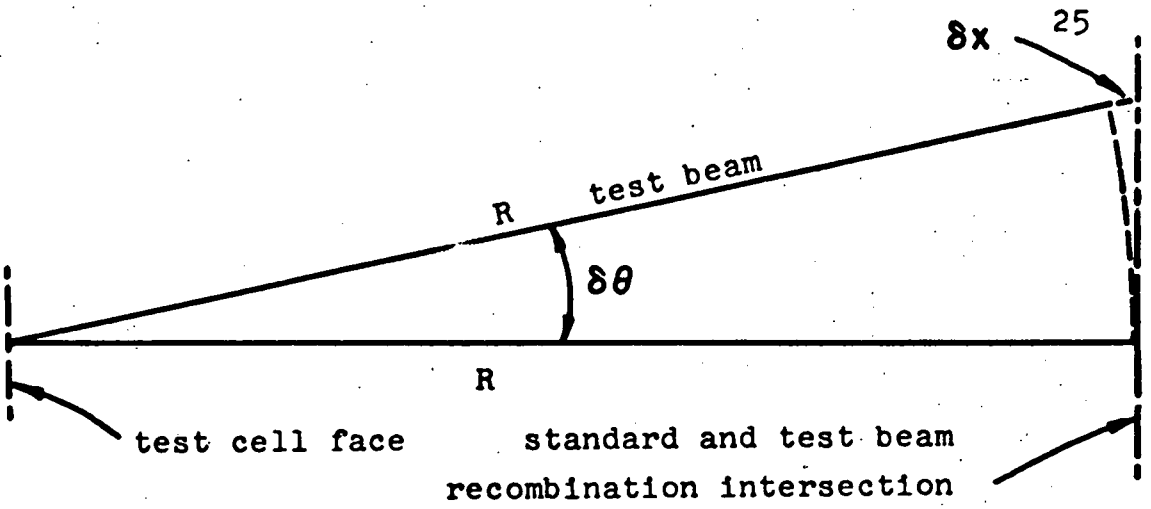

Fig. 2.6 Idealized geometry of the first schlieren effect considered in the text. The test beam travels slightly farther to the recombination intersection.

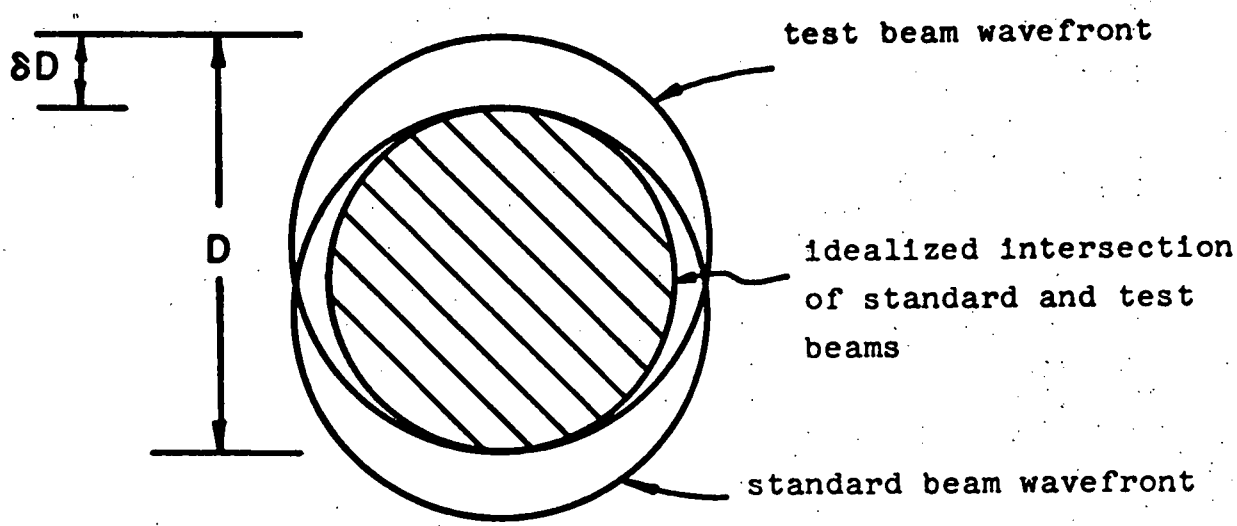

Fig. 2.7 Idealized geometry of the second schlieren effect considered in the text. The test beam is bent upward, and fails to completely overlap the standard beam when they recombine.

$$\frac{100R(\delta\theta)^2}{\lambda_o} = \frac{100RL^2\left(\frac{\partial n}{\partial T}\frac{\partial T}{\partial t}\right)^2}{\lambda_o\left(\frac{\partial y}{\partial t}\right)^2} < 1 \qquad (2.7)$$

Secondly, in Fig. 2.7, the bent ray will not completely overlap its partner at the far beamsplitter. Only an area of about $\frac{\pi}{4}(D-\delta D)^2$ will be bright,* which corresponds to a reduced intensity at the photodetector of approximately $1-\delta D/D$. Again limiting this error to be less than 1 % requires that:

$$\frac{100R\,\delta\theta}{D} = \frac{100RL\left(\frac{\partial n}{\partial T}\frac{\partial T}{\partial t}\right)}{D\left(\frac{\partial y}{\partial t}\right)} < 1 \qquad (2.8)$$

Eqs. 2.7 and 2.8 can be evaluated for the strongest turbulence found in the experiments by using the values:

$R \approx 5$ cm

$L \approx 0.64$ cm

$D \approx 0.05$ cm

$\lambda_o = 6328 \times 10^{-8}$ cm

$\frac{\partial n}{\partial T} \approx 10^{-6}$ per ^{o}C

---

* The geometry of Fig. 2.7 has been greatly simplified; also, any light outside of the central disc is disregarded, as is any lateral displacement of the bent beam by the plexiglass wall.

$$\partial T/\partial t \approx 10^{+5}\ ^{\circ}C/sec \text{ (observed in Fig. 4.4)}$$

$$\partial y/\partial t \approx 3.2 \times 10^{+3} \text{ cm/sec (at Re = 20 000)}$$

Eq. 2.7 yields the criterion:

$$\frac{100R}{\lambda_o} L^2 \left(\frac{\partial n}{\partial y}\right)^2 = 0.003 << 1 \qquad (2.9)$$

and from Eq. 2.8, one obtains the criterion:

$$\frac{100RL}{D} \left(\frac{\partial n}{\partial y}\right) = 0.2 < 1 \qquad (2.10)$$

Note that either of these effects will cause the temperature analog to fluctuate slightly more sharply, which justifies the deduction of $\partial T/\partial t$ from the experimental data of Fig. 4.4.

2.2.8 Nonuniformities of Temperature in the Sensitive Volume

The sensitive volume of the technique is a cylinder, 0.25 in. (0.64 cm) long and 0.5 mm in diameter. Any <u>axial</u> temperature profile is uniformly weighted* and averaged in the interference process. Recall Eq. 2.2:

---

* Uniformly weighted inasmuch as the index of refraction is a linear function of temperature--which is not a problem for the small temperature range in this work.

$$I = I_0 \cos^2 \left\{ \frac{\pi}{\lambda_0} \oint n(T(s))\, ds \right\} \qquad (2.2)$$

where the implicit dependence of the index of refraction on the temperature profile is written out, and the path length integration is carried out along the cylinder's axis. Any radial temperature profile is uniformly weighted and averaged by the double convex lens and photodiode in the detector optics (see Fig. 2.2).

The axial temperature profile is assumed to be uniform throughout this work, and the radial temperature profile is experimentally shown to be very nearly constant. There is a serious lack of information about the local plexiglass wall temperature--the walls continually heat up and cool down at odd intervals during the experiments. Largely because of this, a universal temperature profile cannot be established. If a temperature profile could be established, however, it could easily be included into Eq. 2.2. As an indication of the radial temperature variation, consider the radius vector that points upstream at the laser station; along the vector it is seen that:

$$\frac{\partial T}{\partial x} = \left(\frac{\partial T}{\partial t}\right)\left(\frac{\partial x}{\partial t}\right)^{-1} = \frac{10^5\ ^\circ C/sec}{3.2 \times 10^3\ cm/sec} \qquad (2.11)$$

$= 3\ ^\circ C$ per mm $= 3\ ^\circ F$ over the 0.5 mm beam diameter.

The values are taken from the most extreme cases considered in Section 2.2.7, so that this is the largest radial temperature profile that has been observed.

2.2.9 Important Features of the Temperature Analog

Two important features of the temperature analog are bound up in Eq. 2.2. First, the heating of the plexiglass walls will introduce a large phase angle between the two arms. The rate of variation of the index of refraction of plexiglass with temperature is several orders of magnitude larger than that for air. This slow (but large) variation completely masks the variation of the average temperature in the flow. The turbulence produces a smaller, but much faster variation in the transmitted intensity. This work seeks only this rapidly fluctuating analog, rejects the central moment of the analog as spurious information--since it includes the wall heating, and implements a separate measurement of the average temperature in Section 2.4.4 to replace the central moment.

The second important feature of the analog is closely related to the first. The large phase angle developed by the wall heating causes the analog to drift slowly up or down through many fringes. The analog may operate on a single fringe for 5 seconds to several minutes, but eventually it drifts in phase by $\pi/2$ radians, which puts the analog on the next fringe over. As the phase angle increases by $\pi/2$, say

from $\pi/4$ to $3\pi/4$ in Fig. 2.4, the slope of the analog with temperature changes sign. The effect is to lose sight of whether the analog is upside down or right side up with respect to temperature. None of the analog traces plotted in this work can state the issue absolutely--any number of them can be upside down!

2.3 Optical Bench and Environment

The interferometer must rest on an extremely quiescent surface to isolate the physical lengths of the arms from vibrational distortion. Further, the optical bench must allow the turbulent flow to rise up through the test arm of the interferometer. The optical bench aimed at satisfying these two requirements is drawn in Fig. 2.8. The positions of the optical components are diagrammed on its surface. The long slot, 5 in. x 53 in. (13 cm x 135 cm), accepts the upright test cell without touching it. The test cell rests in a separate jig that allows the cell to be freely moved about in the slot between the two wide-flange beams. The temperature measurements originate in the flow at the intersection of the laser beam $\overline{A'B}$ and the test cell. Moving the test cell in its jig moves the measuring station accordingly.

The optical bench consists of two 10 in. x 12 in. (25 cm x 30 cm) steel wide-flange beams that are firmly clamped onto two thick steel crossmembers and two short 6 in. x 6 in.

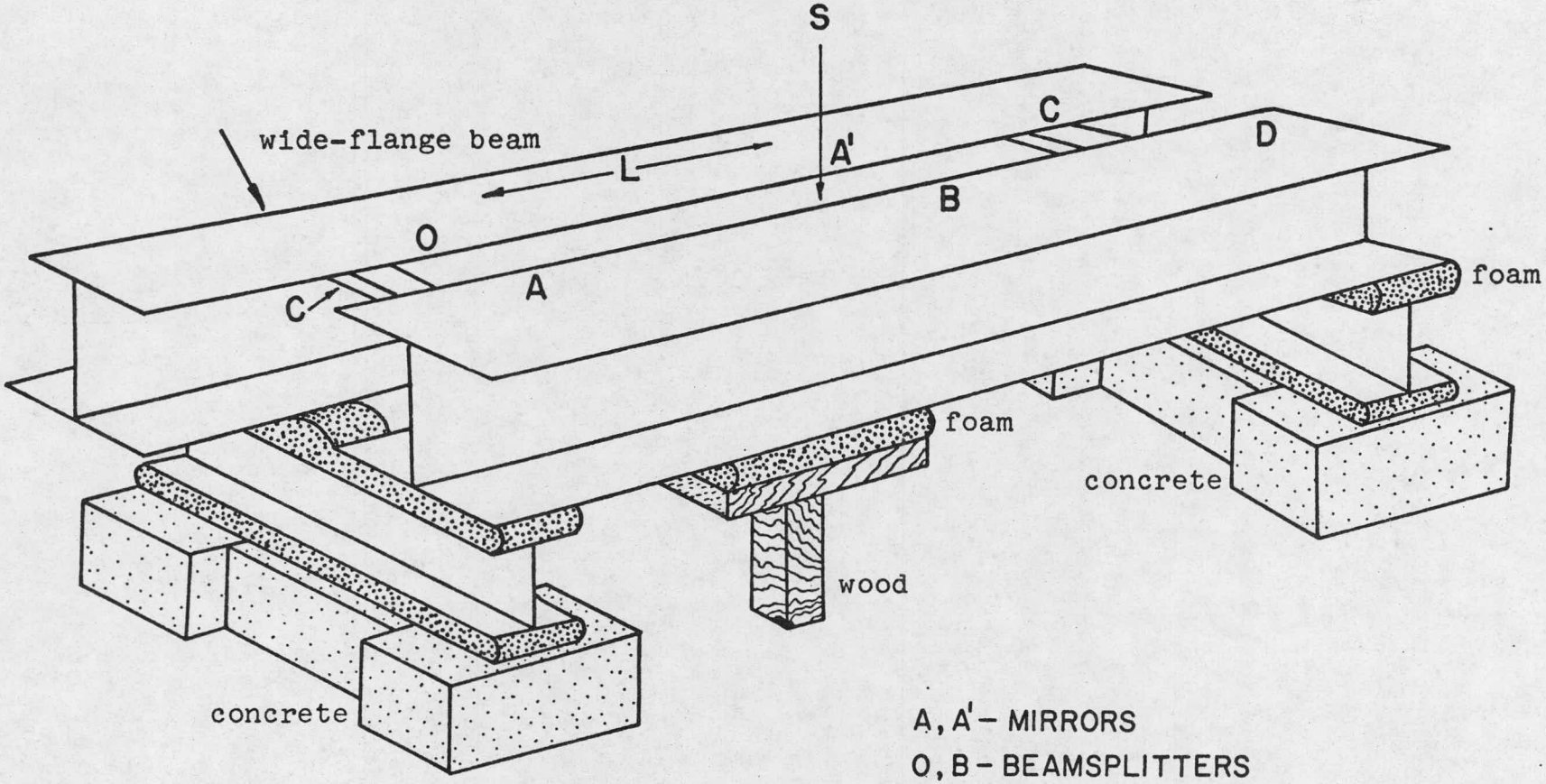

A, A' – MIRRORS
O, B – BEAMSPLITTERS
L – LASER
D – DETECTOR
S – SLOT
C – CROSSMEMBERS

Fig. 2.8 OPTICAL BENCH

BENCH MASS = 1000 lb_m

(15 cm x 15 cm) steel I-beams. Stiff foam isolates this rigid steel frame from the concrete block foundation. Each long wide-flange beam is further isolated with a wood and foam "shock absorber"--not much damping is afforded, but the fundamental modes of the beams are broken up. A dozen concrete blocks are loaded onto the lower flanges of the wide-flange beams at irregular intervals with the purpose of further distorting the fundamental modes of the beams. The entire bench mass is about 1 000 lb_m (455 kg).

The experiments are set up in the basement of Bldg. NW-13 in Cambridge. The building's machine shop and the outside street traffic greatly disturb the system, so the experiments are always performed at night or on Sunday. Even so, a few incessant building pumps are present, producing noise in the several hundred Hz range. Low frequency building vibrations of about 6 Hz are present at approximately the same amplitude. The actual noise signals are demonstrated in the discussion of the results in Section 4.1.1.

The optical bench and the basement workspace are only marginally satisfactory for these experiments. It is hopeful to note that extremely sophisticated benches are commercially available, which would set the vibrations problems to rest. An alternate and inexpensive sand-box bench design investigated earlier at MIT[16] proved to be just as marginally satisfactory.

2.4 Test Cell Design

2.4.1 Test Cell Scaling

The Argonne National Lab (ANL) 1/15-scale Fast Flux Test Facility (FFTF) liquid sodium test loop is the standard geometry for the flow experiments. It is sketched in cross-section in Fig. 2.9, where several pertinent Reynolds numbers are developed. Note that the inlet Reynolds number is just twice the outlet Reynolds number. The test assembly that simulates this flow in air seeks to recreate this condition.

The cross-section of the cylindrical ANL test loop is represented by the thin test assembly of Fig. 2.10. The test assembly is slightly enlarged (with a simple arithmetic scaling) to accomodate the large Reynolds numbers while decreasing the large flow rates. Even so, an entrance velocity of air of 390 ft/sec (119 m/sec) is needed to match the ANL turbulence. The flows of air investigated are about 10 times smaller than this.

2.4.2 Test Cell Thickness

The inside test cell thickness, L, is chosen so that the highest expected temperature in the assembly will just bring the transmitted intensity down to its first minimum:

$$\oint n(s)\,ds = (-1)\frac{\lambda_o}{2} \qquad (2.12)$$

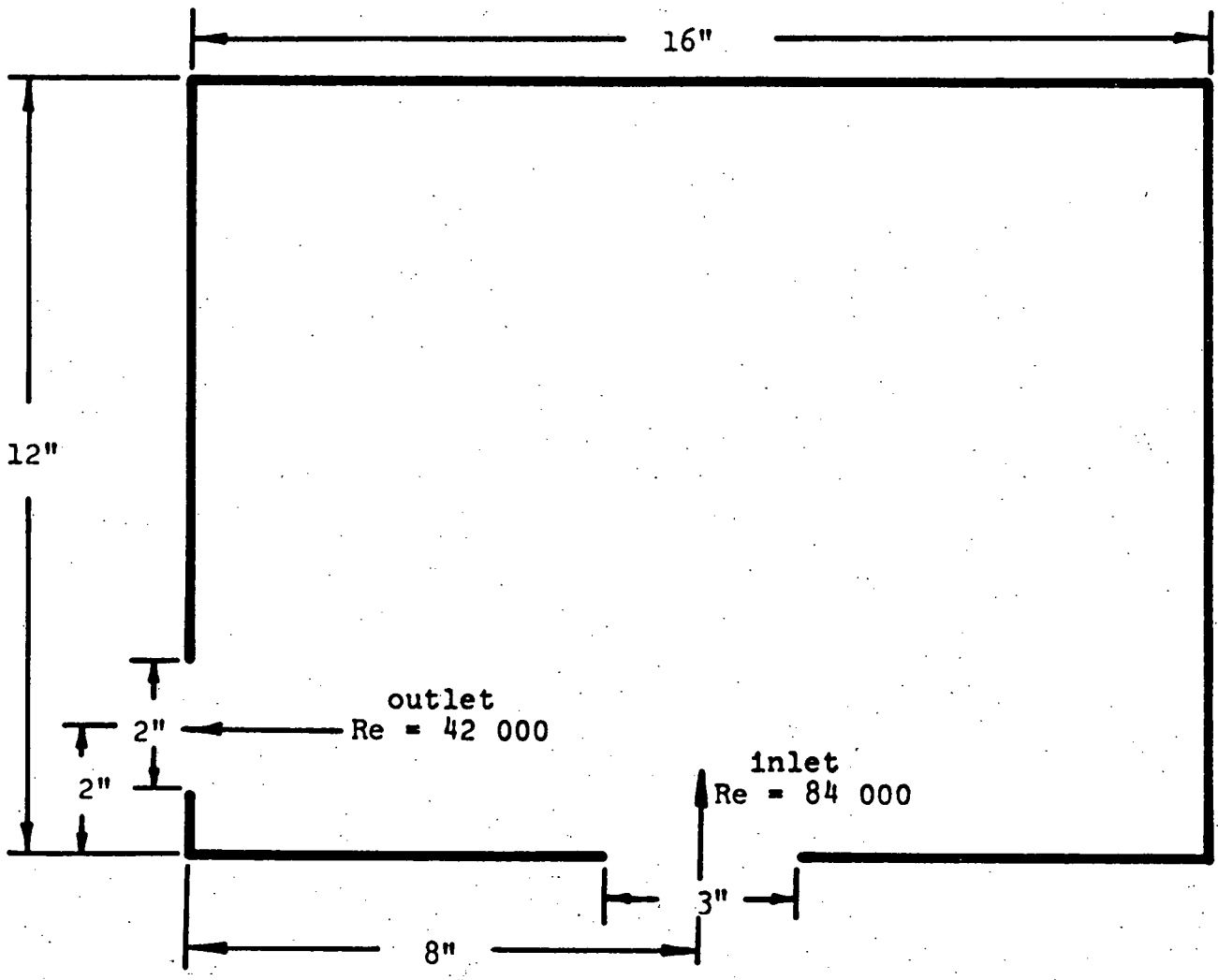

Fig. 2.9 Cross section of the ANL 1/15-scale FFTF outlet plenum. The cylindrical plenum has three 2". diameter outlet nozzles.

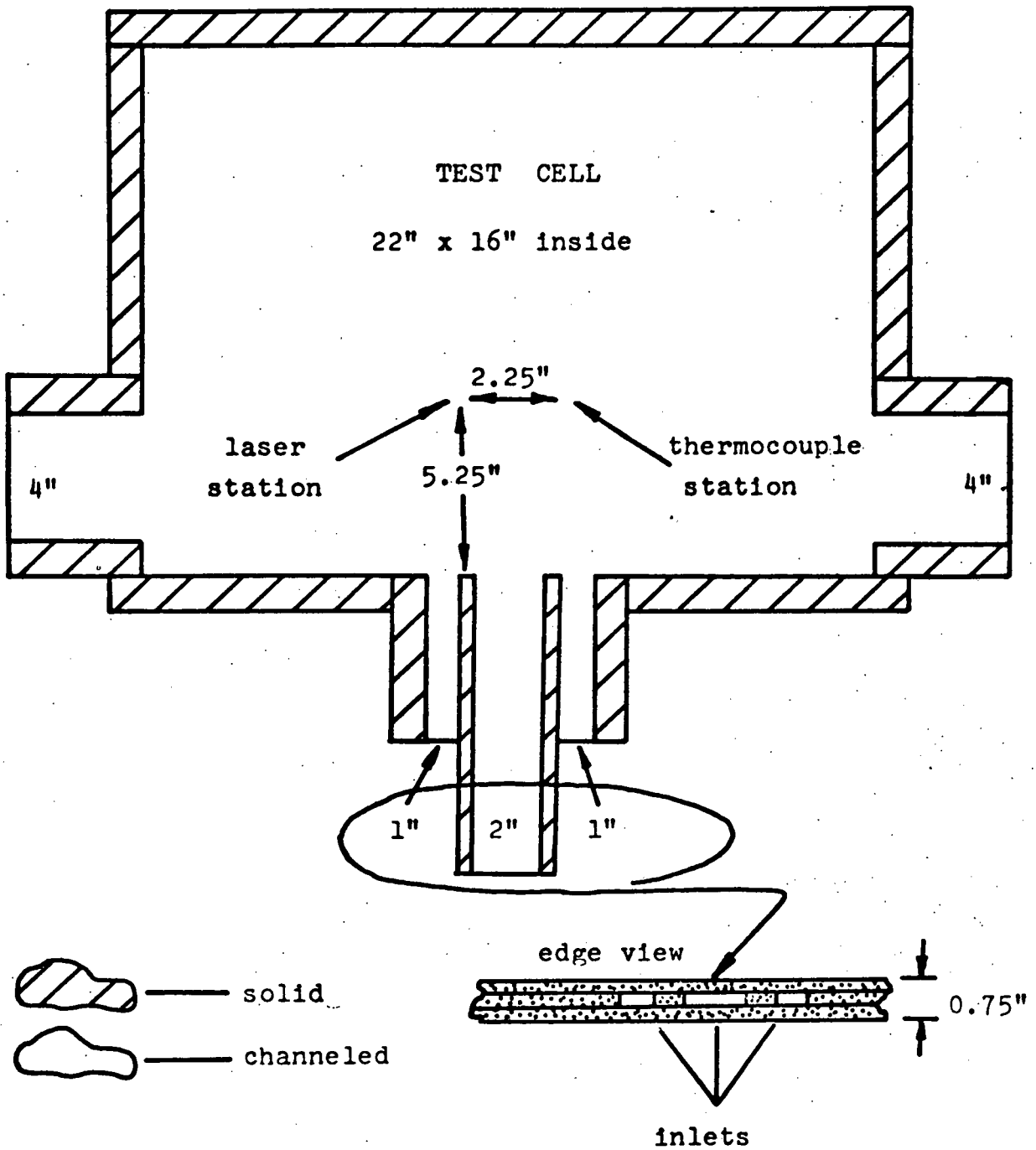

Fig. 2.10 Test cell dimensions.

The integral is simply evaluated to be:

$$\int_0^L n_{test}\, ds + \int_L^0 n_{std}\, ds = L(n_{test} - n_{std}) \qquad (2.13)$$

For this experiment, L should be approximately 9/32 in. (0.71 cm), assuming a uniform temperature profile across the assembly. The assembly is fabricated of 1/4 in. (0.64 cm) laminated plexiglass, making L = 1/4 in. (0.64 cm). Sources of variation in the measurable thickness are nonuniformities in the plexiglass stock, and bowing of the assembly under the pressure conditions of the flow. These errors have been found not to be important in comparison to the noise generated by vibrations. The major source of error in the test cell design calculation of Eq. 2.12 is the temperature deviating from a flat profile, discussed in Section 2.2.8.

2.4.3 Flow Preparation

The hot and cold inlet flows are prepared from ambient air, and they are not directly recirculated after mixing. A single "squirrel cage" blower maintains the entire flow in a single 2 in. (5 cm) ID hose. The flow enters a moderately sized chamber that isolates the test cell from undesirable pressure pulses and vorticity imparted by the "squirrel cage." Half of the flow is drawn off in a 2 in. (5 cm) ID hose, and sent about 6 ft. (2 m) to a flow shaping plenum directly underneath the test assembly. The ambient flow is

symmetrically distributed into the two outer inlets labeled "ambient" in Fig. 2.11. The other half of the flow in the isolation chamber flows through an uncontrolled heater (in fact an enclosed toaster set for very dark toast) and into another chamber to completely mix the heated air. The hot flow is drawn off in another 2 in. (5 cm) hose and sent about 6 ft. (2 m) directly into the inlet labeled "heated" in Fig. 2.11.

Before the turbulent mixing experiments, with the heater turned off, the velocity of the flows is measured with a hot wire anemometer. By constricting the cold leg flow, the hot and cold leg flows are matched within a few percent. The entire flow is controlled by choking the "squirrel cage" inlet. The hot wire probe is left to monitor the velocity and temperature in the hot leg, and no further changes are made in the flow geometry.

As the hot leg flow gradually heats up, the increase in specific volume of air causes the hot leg velocity to increase, i.e., the mass flow stays constant along with the pressure drop. The cold leg flow retains its former value, and the flows begin to shear in the assembly. No flow visualization experiments were carried out to study the effect of this shear on the average recirculating flow, but the effect must be kept in mind while weighing the results--especially where the hot leg temperature is taken as an

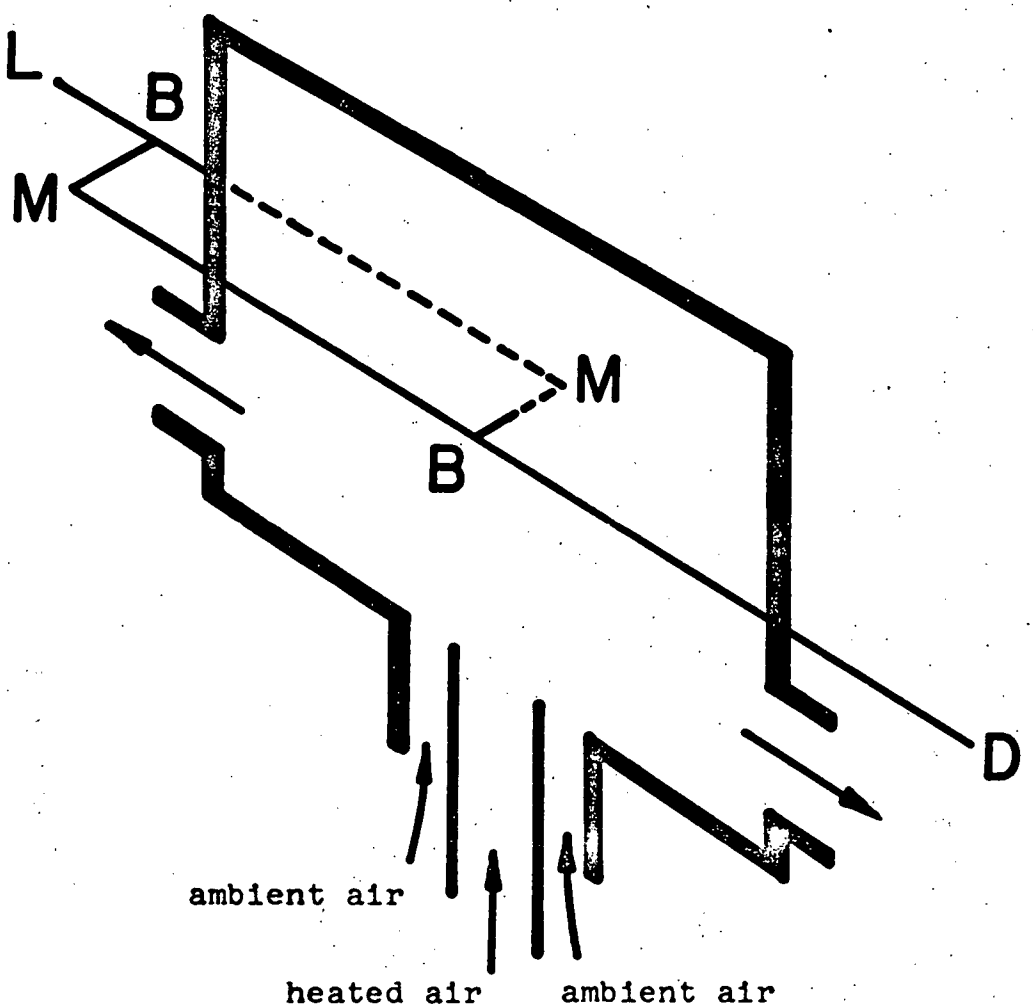

Fig. 2.11 Isometric View of inlet flows and interferometer optics in the test cell. L--laser; B--beamsplitters; M--mirrors; D--detector.

independent parameter.

2.4.4 Monitoring the Average Temperature

Owing to the inability of the system in its primitive form to follow the average temperature of the flow (discussed in Section 2.2.1), extra instrumentation is needed. The symmetry of the test cell is exploited by placing a thin thermocouple in the flow at a station that is symmetric with respect to the laser station (see Fig. 2.10). A fine chromel-alumel thermocouple protrudes into the middle of the test cell through a 1/16 in. (1.6 mm) diameter hole in the cell's front face. The thermocouple wires are 28-gauge, or 0.0156 in. (0.40 mm) in diameter. A digital microvoltmeter displays the electromotive force developed at the junction. A measured characteristic curve of the installed thermocouple is found in Fig. 2.12. The temperature standard is the hot wire probe. The reference juction sits in air, spaced several feet away from any heat sources, including hands.

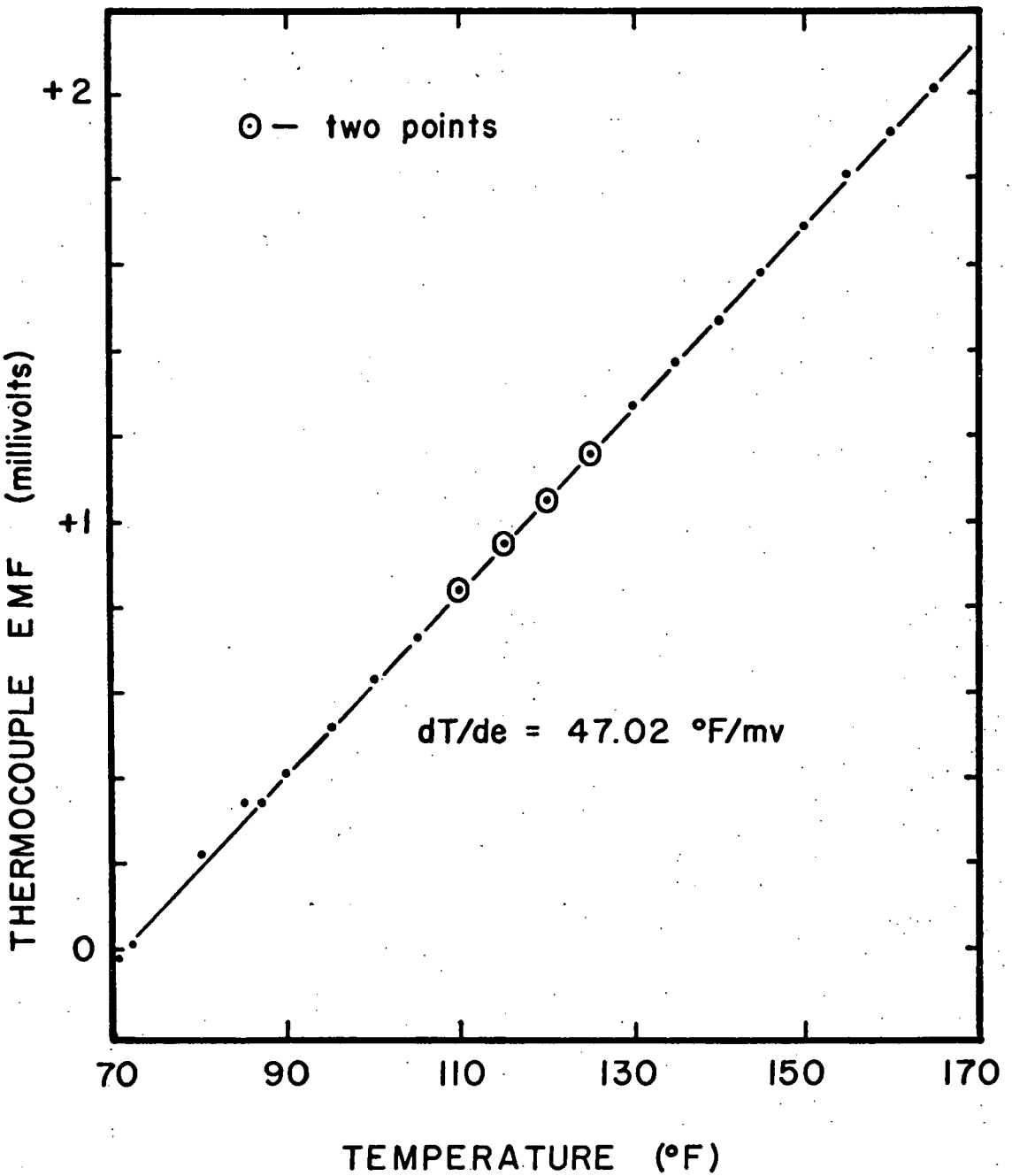

Fig. 2.12 Plot of the thermocouple characteristic. The reference junction is kept in ambient air.

3. TREATMENT OF DATA

3.1 Displaying and Storing the Temperature Analog

The equipment that displays and stores the temperature signal is listed in Table 3.1, and illustrated in Fig. 3.1. The heart of the experiment is the storage oscilloscope. Consider the fringe contrast, $\mathcal{V}$, defined in terms of the maximum and minimum intensities developed at the photodiode:

$$\mathcal{V} \equiv \frac{I_{max} - I_{min}}{I_{max} + I_{min}} \tag{3.1}$$

A straightforward extension of Eq. 2.2 that accounts for non-ideal fringe contrast is:

$$I = I_{min} + (I_{max} - I_{min}) \cos^2 \left\{ \frac{\pi}{\lambda_0} \oint n(s)\, ds \right\} \tag{3.2}$$

To display a signal, the vertical position control on the oscilloscope is set to entirely suppress the constant term, I_{min}, and the vertical gain controls are adjusted to display the coefficient, $I_{max} - I_{min}$, at the top of the vertical scale. In this way, for any observable fringe contrast, the oscilloscope displays only a full scale waveform of:

$$\cos^2 \left\{ \frac{\pi}{\lambda_0} \oint n(s)\, ds \right\}$$

Occasional drifts in fringe contrast, battery voltage, etc., are counteracted with the oscilloscope.

The analytic inversion of this relation that yields the

Table 3.1

EQUIPMENT FOR ANALOG TEMPERATURE MEASUREMENTS

1. Storage oscilloscope: Hewlett-Packard model 141B oscilloscope
   --single trace triggered manually
   --sweep generated internally
   --amplifier in DC mode

2. Laser light source: Spectra-Physics model 125A 50 mW He-Ne laser

3. Digital voltmeter: Thermo-Systems Inc. model 1076 voltmeter
   --DC mode; 10 volts full scale

4. Thermocouple monitor: Keithley model 160 Digital Multimeter
   --DC mode; 2 mV full scale

5. Camera: Nikkormat model FT2, 35 mm camera
   --135 mm f3.5 lens
   --M2 extender ring

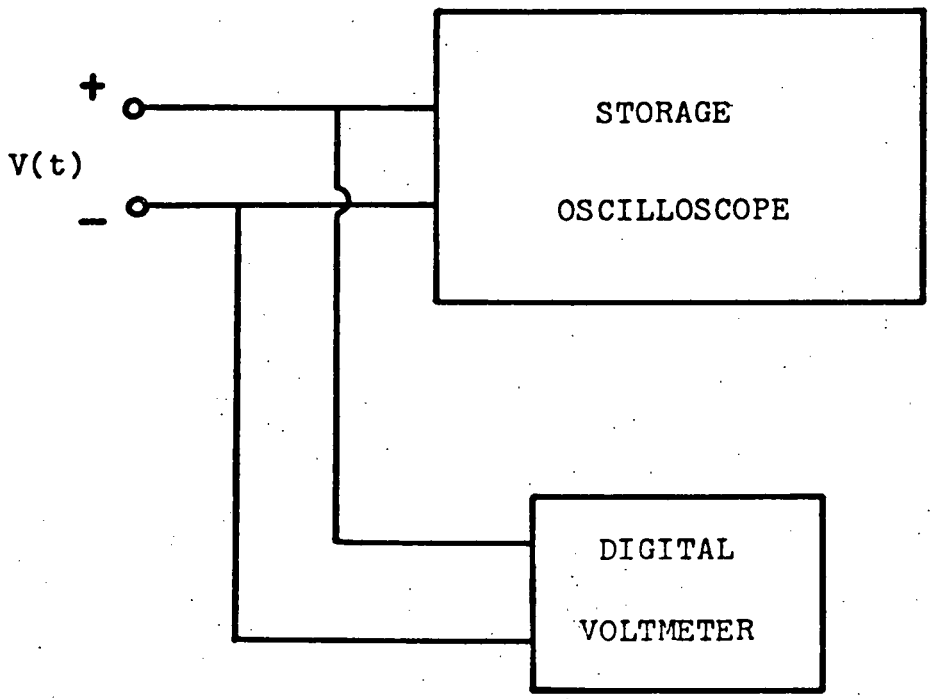

Fig. 3.1 Schematic diagram of the electronics for sampling the temperature analog, V(t).

temperature is shown in Fig. 3.2. The solid curve is a plot of the $\cos^2$ term versus the fluctuating temperature. As explained in Section 2.2.9, the average temperature and the sign of the fluctuating temperature are not known. This must be reflected in the choice of an ordinate for the analog. In all of the temperature-time traces of Section 4.1, the curve in Fig. 3.2 is the basis for the construction of the non-linear temperature scales on the ordinates. The temperature measurements are practical in real time only as far as the solid curve in Fig. 3.2 is linear.* Several schemes are developed in the figure for linearizing the system's response. Simply matching the slope of the response in its most linear region, i.e., about its half-maximum, gives excellent agreement over a small 50 ^{o}F range. A least-squares fit of the response gives a less accurate agreement, but extends the range to 100 ^{o}F. Only the power spectral density measurements in this work are performed in real time, where it is assumed that the temperature analog is linear. The discussion of the strategy for the interpretation of the system's response is only added for completeness.

Note that the temperature waveform is always sampled when it is near the half-maximum because the technique is

* Otherwise the analog would have to undergo an instantaneous "arccos $\sqrt{V(t)}$" operation--presumably in some strikingly nonlinear amplifier.

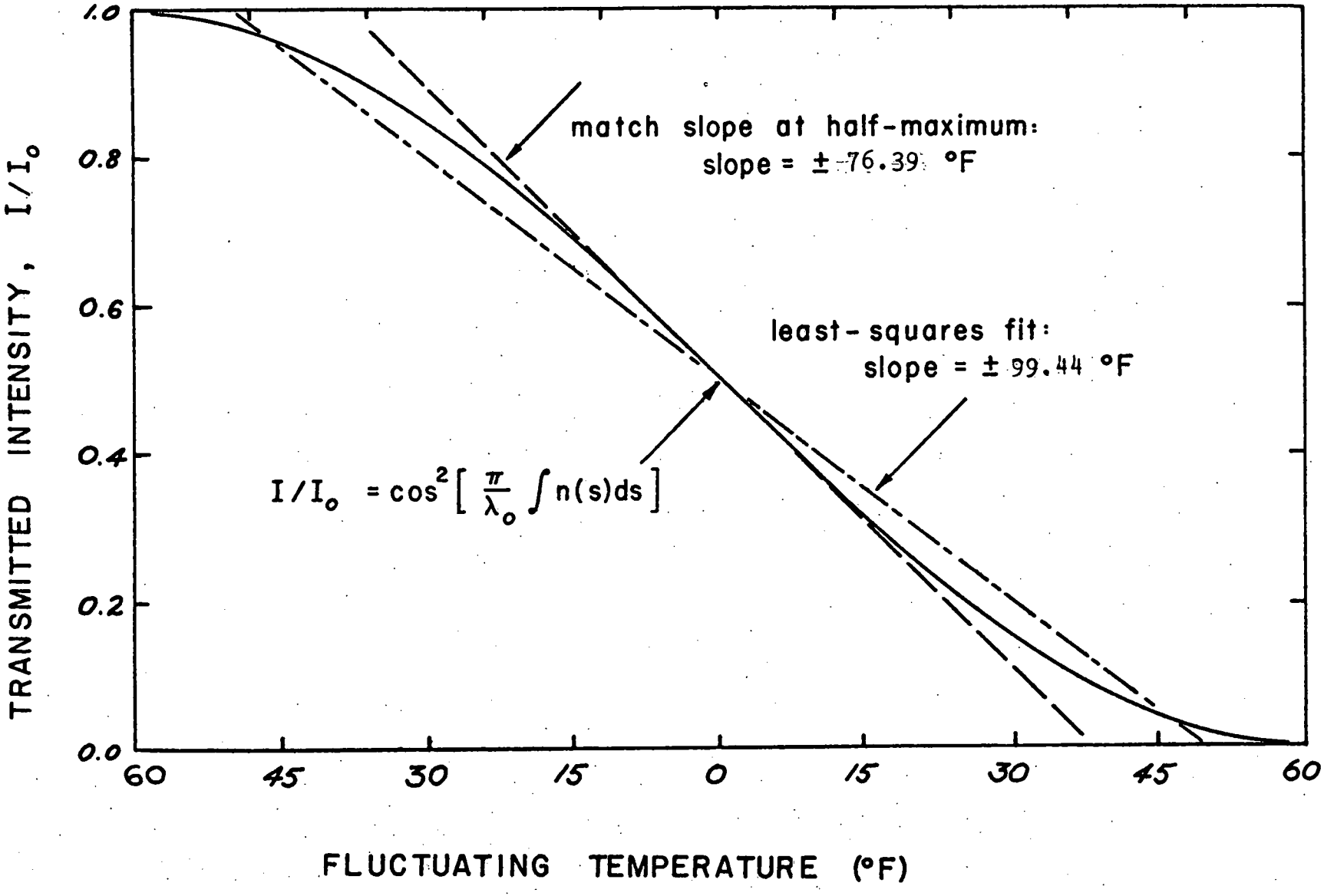

Fig. 3.2 Plot of the system response to fluctuating temperature. The dashed curves are linearizations of the system response.

most sensitive at the half-maximum. Experimental verification of this is presented with the results in Section 4.1.1.

A single sweep of the oscilloscope can be stored on the special screen of the cathode ray tube for a few minutes. A single lens reflex camera records the trace on the oscilloscope in 35 mm format. The negative is mounted as if it were a slide, and projected with an enlarger. The projection is traced in pencil, inked, and labeled. The traces that appear with the results are all generated this way, and are fair representations of the actual temperature waveforms.

3.2 Fourier Analysis of the Temperature Signal

The equipment that Fourier-analyzes the temperature signal is listed in Table 3.2, and illustrated in Fig. 3.3. The heart of the experiment is the plug-in analyzer, which can slowly sweep through a preset range of frequencies, or hold at a single frequency to sample the Fourier component indefinitely. The analyzer must be calibrated for its frequency display and its RMS amplitude display, i.e., both abscissa and ordinate are calibrated. A frequency generator performs both of these tasks by generating standard frequencies and amplitudes--both of which are verified on an oscilloscope. An actual frequency calibration is shown in Fig. 3.4. The analyzer frequency display is first matched at 2 kHz and 10 kHz with standard inputs. The frequency

Table 3.2

EQUIPMENT FOR POWER SPECTRAL DENSITY MEASUREMENTS

1. Frequency analyzer: Hewlett-Packard model 141B oscilloscope with Nelson-Ross model 032 Plug-in Analyzer
   --range attenuation at 0 DB
   --input attenuation and gain adjustable
   --50 sec scan
   --video filter IN
   --LOG mode IN
   --Auto Scan IN
   --High resolution

2. Frequency generator: Wavetek model 134 Sweep Generator
   --variable amplitude; 0.1 to 10 volts
   --variable frequency
   --sine wave mode

3. Temperature analog display: Tektronix model 541 Oscilloscope with type L Plug-in Amplifier

4. Laser light source: Spectra-Physics model 125A 50 mW He-Ne laser

5. Digital voltmeter: Thermo-Systems Inc. model 1076 voltmeter
   --DC mode; 10 volts full scale

6. Thermocouple monitor: Keithley model 160 Digital Multimeter
   --DC mode; 2 mV full scale

7. Camera: Nikkormat model FT2, 35 mm camera
   --135 mm f3.5 lens
   --M2 extender ring

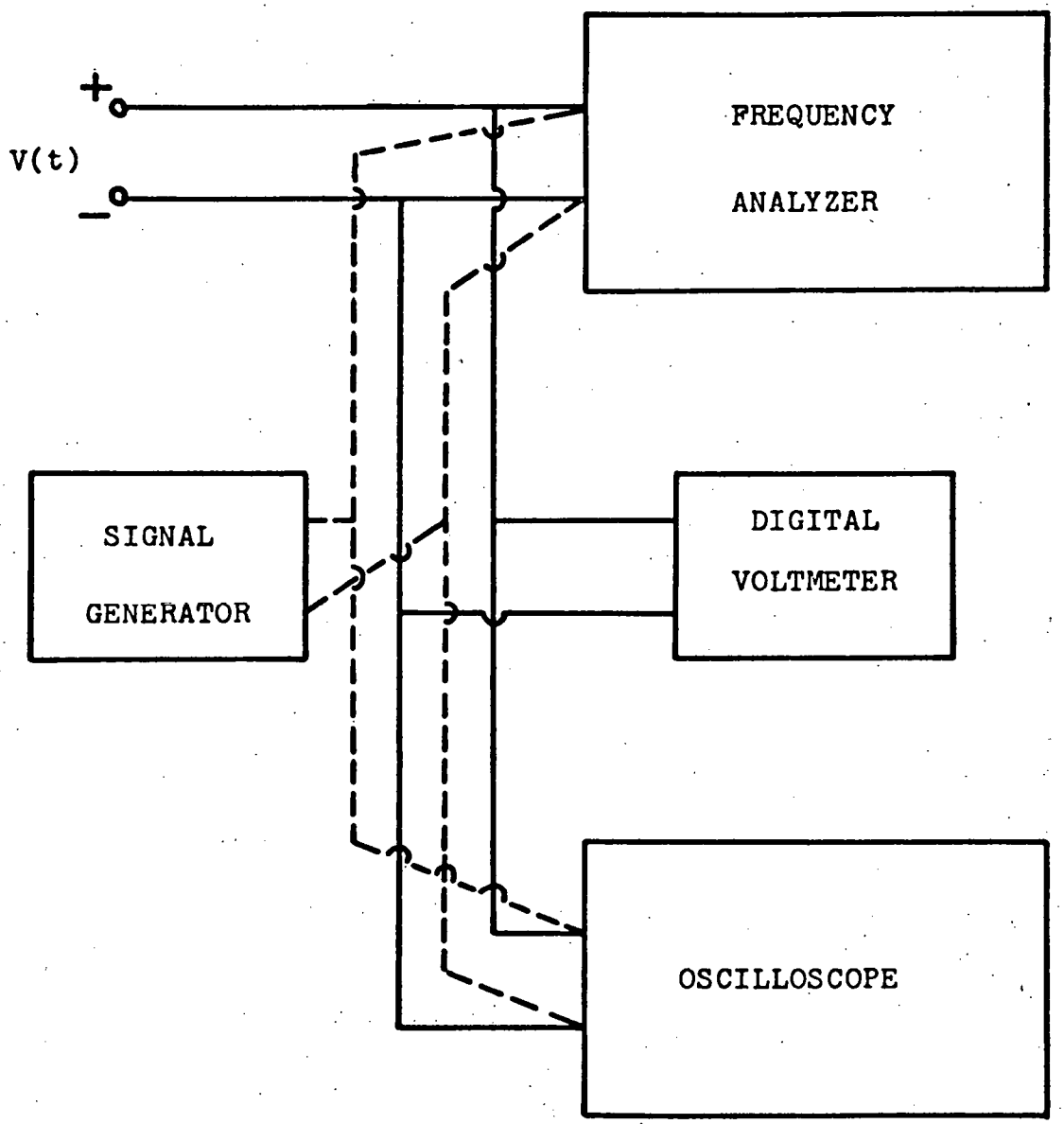

Fig. 3.3 Schematic diagram of the electronics for power spectral density measurements. V(t) is the temperature analog. Dashed lines--calibration mode; solid lines--Fourier analysis mode.

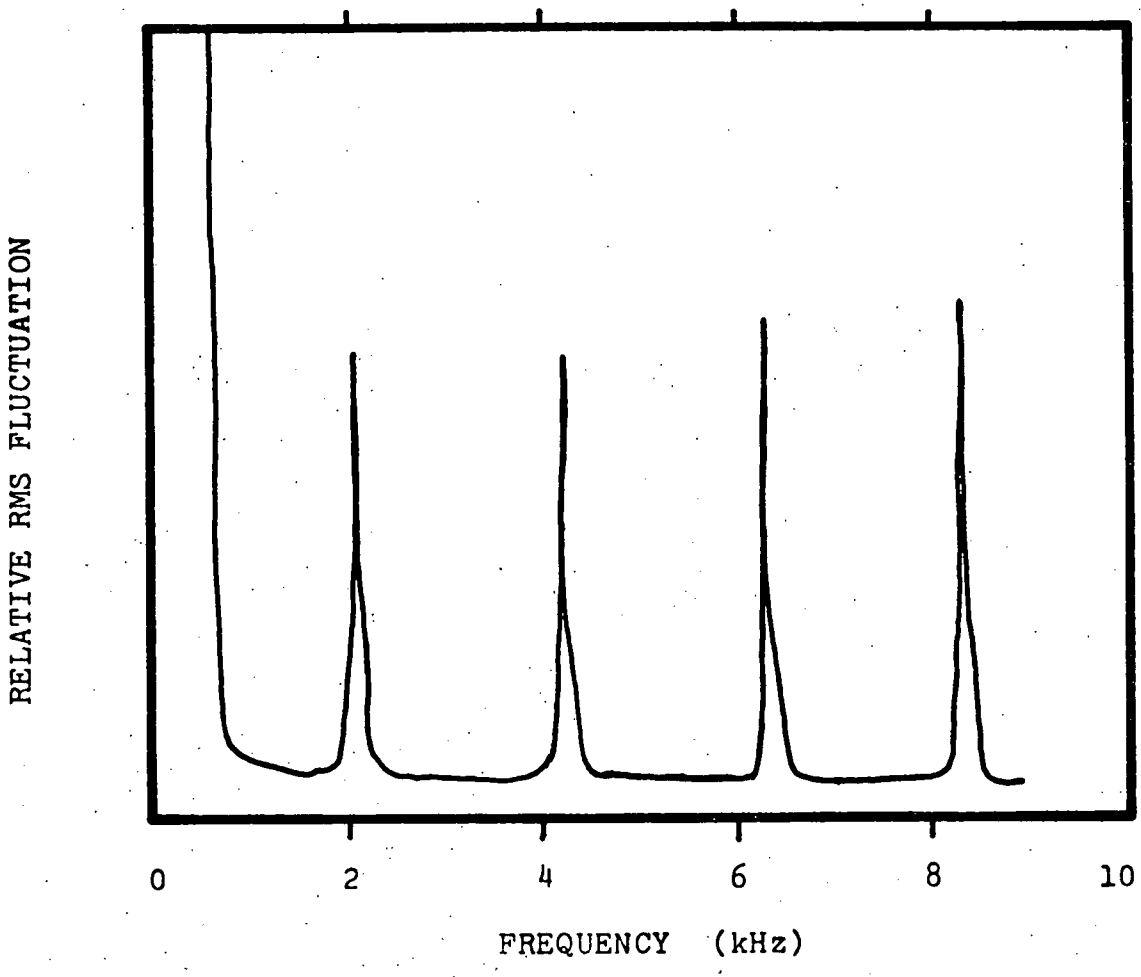

Fig. 3.4 Frequency analyzer output with four sine-wave inputs of equal amplitude at 2, 4, 6, and 8 kHz. The analyzer is calibrated to correctly display 2 kHz and 10 kHz signals.

display is linear within a few percent against the four input sine waves of the figure. The vertical display of RMS amplitude is always set in the LOG mode, except in the experiment that produces Fig. 4.32, where it is set in the LINEAR display mode. The vertical gain of the analyzer may be varied continuously with a fine vernier, or discontinuously with input attenuators of 20 DB (tenfold) increments. In practice, the fine vernier is never altered, and the 20 DB gain increments are available for use without disturbing the calibration. The total RMS amplitude range of the analyzer is about 3 decades, i.e., a factor of 1000.

In order to compare the results from day to day, the detector output voltage "window," corresponding to $I_{max} - I_{min}$, must be the same. This preserves the absolute magnitude of a given temperature fluctuation. Scaling $I_{max} - I_{min}$ with the variable gain on the oscilloscope cannot be allowed, since it does not alter $I_{max} - I_{min}$. Instead, the variable aperture in the detector optics is opened or closed very slightly to recreate the same $I_{max} - I_{min}$ in every experiment. Once or twice an hour, the aperture is again articulated to correct for any drift in the system. Typically this voltage "window" is 4 volts, plus or minus 5 %.

Additionally, the waveform must be centered on the half-maximum. This insures that the sensitivity of the measurement is preserved during the frequency analysis. This

constraint requires a feedback system that can identify and counteract the slow wall heating while the analyzer is sampling the signal. The author has volunteered himself as a (human) feedback system. By keeping an eye on the temperature analog displayed on a separate oscilloscope, and by placing a finger on the optical bench, the signal is centered on the half-maximum by continuously adjusting the pressure of the finger on the bench. In effect, an elastic distortion of the interferometer counteracts the slow optical path length changes. The feedback only occurs in the very low Hz range, and has no effect on the Fourier analysis in the kHz range. It is not an elegant method, but it works. Alternate electro-mechanical feedback systems could be implemented, of course.

A typical analyzer output appears in Fig. 3.5. The output is recorded in exactly the same way as the temperature analogs are recorded in Section 3.1. The entire sweep of information takes 50 seconds, and for the most part, the scatter in the curve is due to insufficient sampling by the analyzer. The scatter of the curve appears normally distributed on the log scale. Thus, the errors are assumed to be lognormal. A simple smoothing of the log display is thereby justified, and it appears as the dashed curve in Fig. 3.5. To calculate a power spectral density curve, the RMS data is squared to give relative mean-square fluctuation data, a

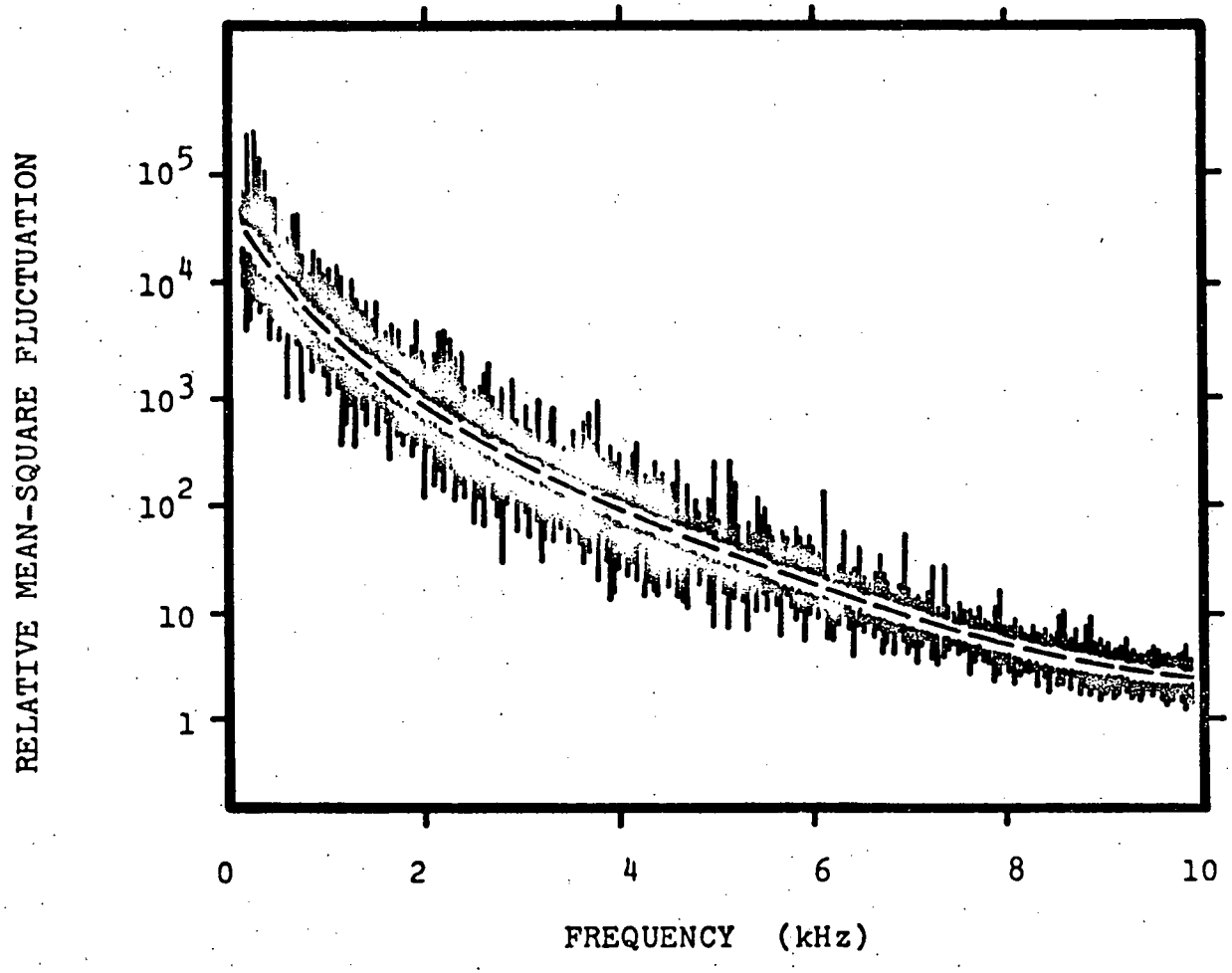

Fig. 3.5 Typical spectral analyzer output at Re = 19100; heated inlet at 148°F. The superimposed (dashed) line represents a smoothed curve of the data.

background mean-square curve is subtracted, and the curve is normalized to unit area. An illustration of the steps is included in Section 4.2.

3.3 Autocorrelations of the Temperature Analog

The autocorrelations of the temperature signals are calculated on a computer. The temperature signal is digitalized by hand at two hundred points, $\mathcal{T}$. The computer sweeps through the data, picking the points out in pairs that are separated in time by τ. The autocorrelation function, $\rho(\tau)$, is calculated from:

$$\rho(\tau) = \sum_{t=1}^{\mathcal{T}-\tau} \frac{T(t)T(t+\tau)}{\mathcal{T}-\tau} \Bigg/ \sum_{t=1}^{\mathcal{T}} \frac{T^2(t)}{\mathcal{T}} \qquad (3.3)$$

The computer program is listed in the Appendix. Near $\tau = \mathcal{T}$, very few pairs are available for the averaging, and $\rho(\tau)$ becomes meaningless for τ of the order of the analog sampling duration. Electronic implementation of $\rho(\tau)$ on the temperature analog would provide more accurate results that would extend far beyond this premature limit.

4. RESULTS

4.1 Analog Temperature Studies

4.1.1 Noise and Errors

The noise traces presented in this section are representative of all of the noise traces observed in the experiments. Noise traces are presented for the two groups of inlet Reynolds numbers--Re = 5 000 and Re = 10 000--that are provided by two different pumps used in the experiments. Noise at Re = 20 000 is shown to be unacceptably high due to an inlet flow vibration that is particular to the plexiglass test cell. Fig. 4.1 shows one second of building noise with the 1/30 HP blower turned off. Fig. 4.2 shows the effect of the pump, which adds a 120 Hz ripple to the noise trace. Fig. 4.2 is representative of the noise in the Re = 5 000 results. Fig. 4.3 shows the effect of the large 1/4 HP blower. The blower adds a large, high frequency noise component to the trace. This effect is corrected by isolating the blower in thick fiberglass insulation, and choking its flow down to Re = 10 000. Two temperature traces are shown in Fig. 4.4, for comparison with the noise in Figure 4.3. Figs. 4.5 and 4.6 are representative of the noise at Re = 10 000. Generally, the noise accounts for a ± 5 ^{o}F (3 ^{o}C) error in the temperature signal, which is somewhat dependent upon the duration of the trace. The longer traces show slightly more noise than

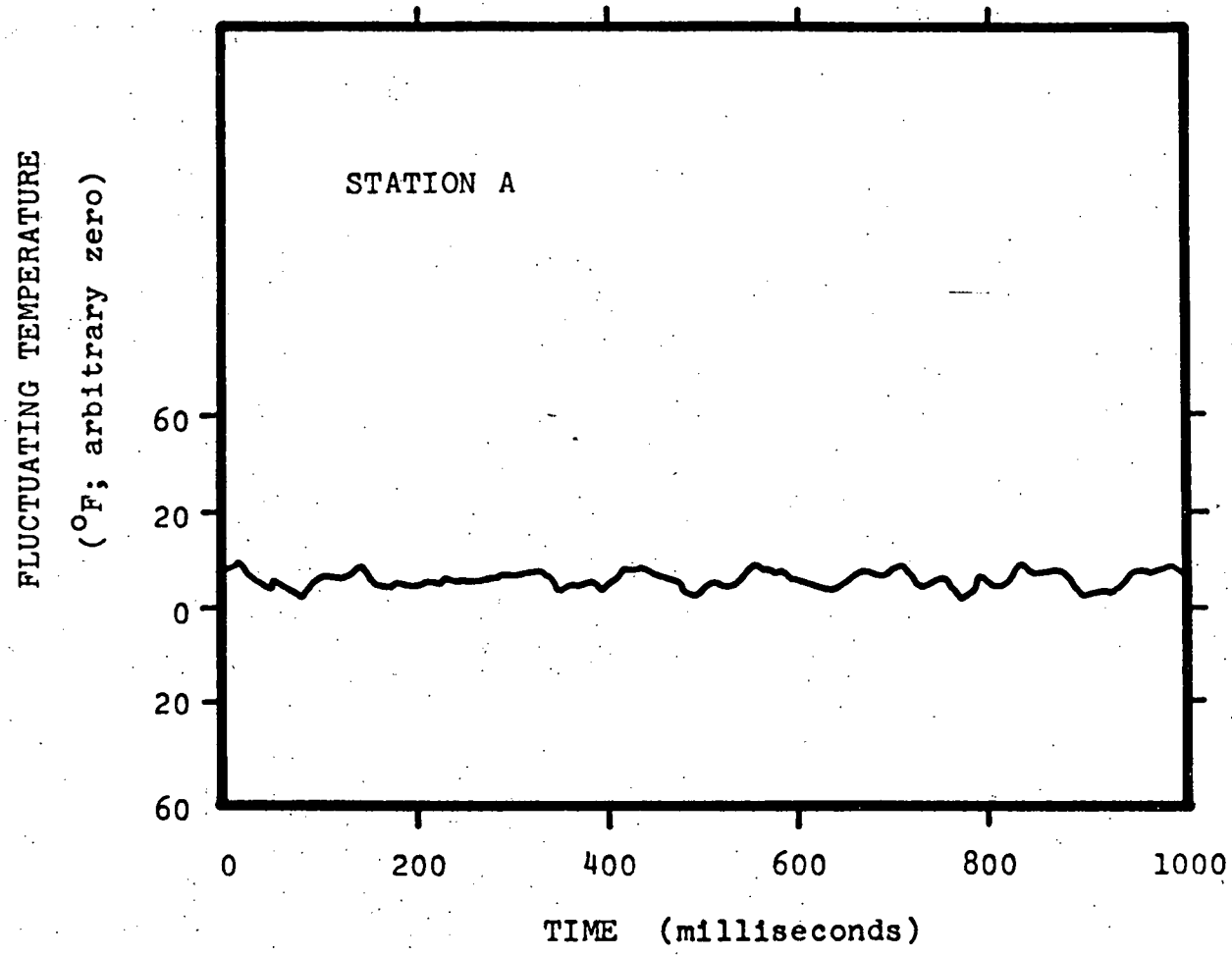

Fig. 4.1 Noise in the temperature analog; Re = 0; no heating.

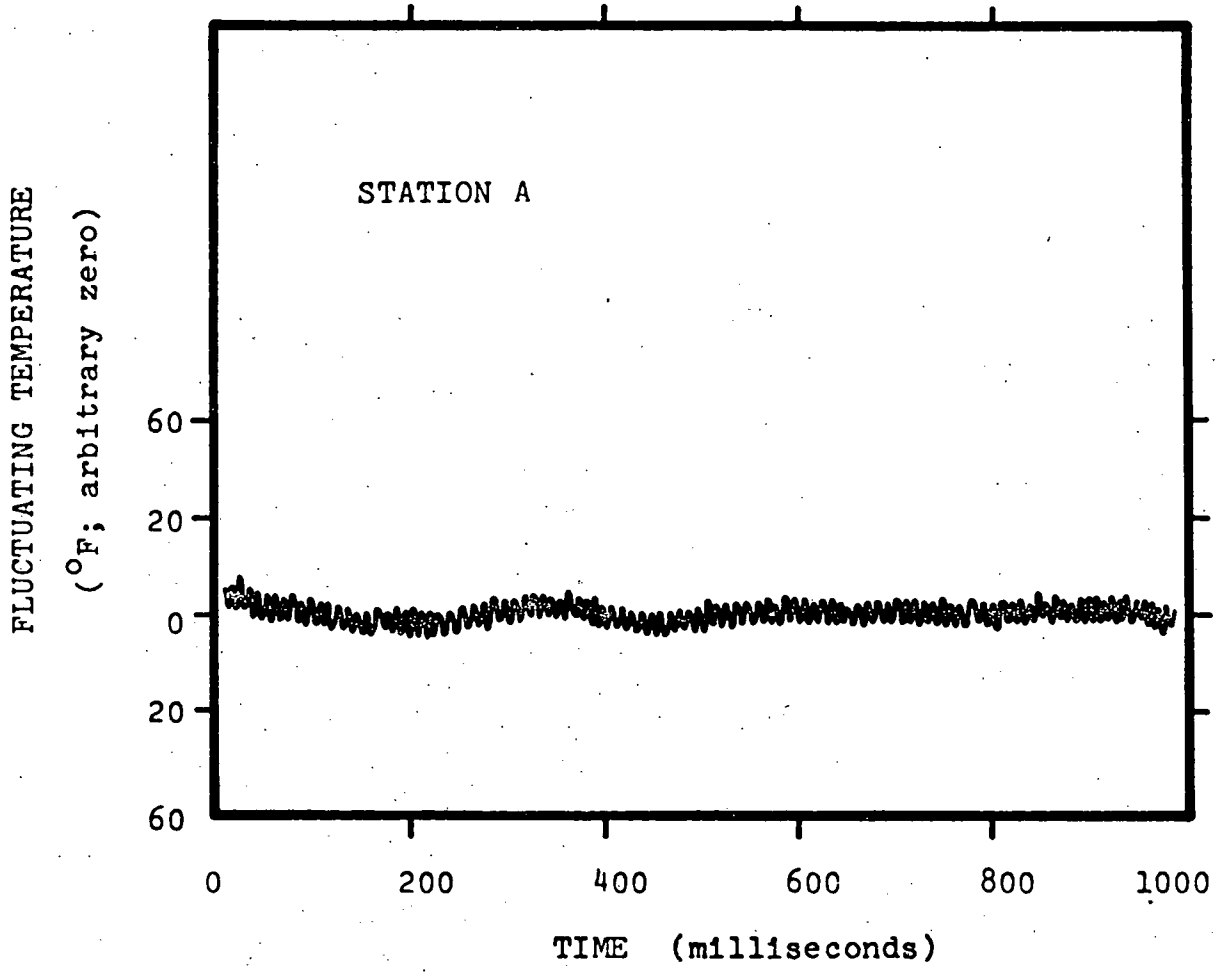

Fig. 4.2 Noise in the temperature analog; Re = 3800; no heating.

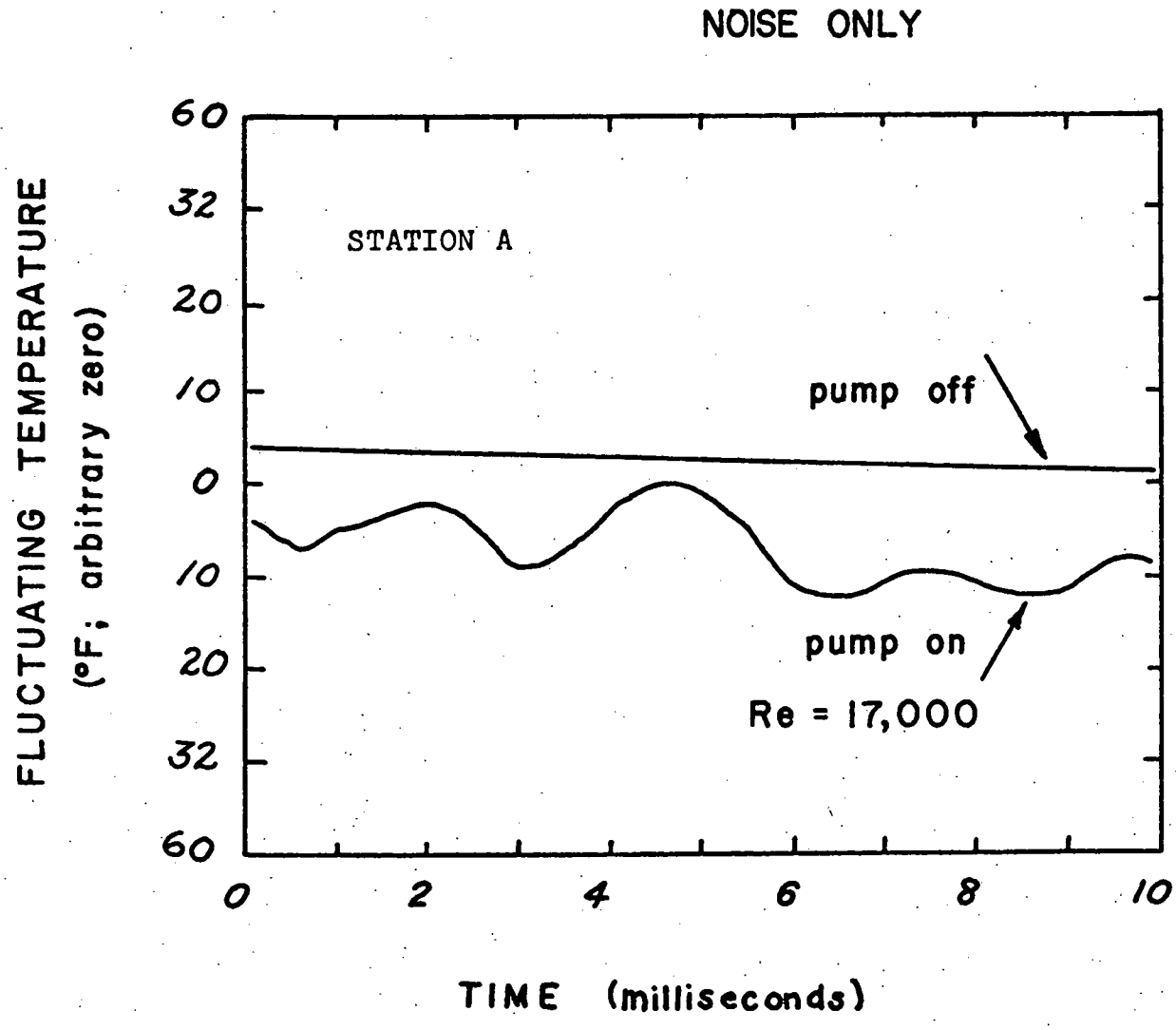

Fig. 4.3 The effect of the "squirrel cage" blower on the temperature trace at Re = 17000.

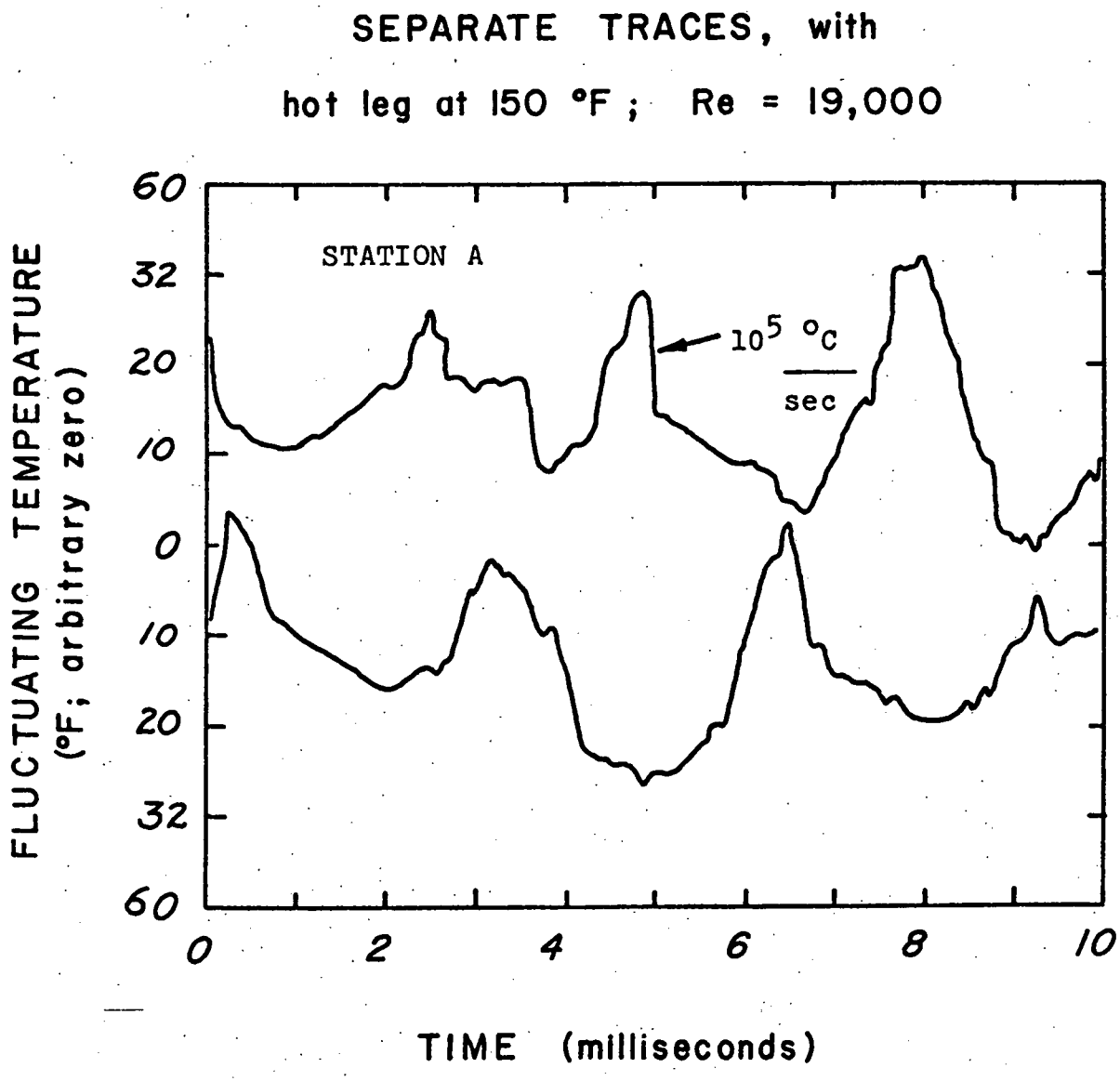

Fig. 4.4 Temperature traces at Re = 19000, for comparison with Fig. 4.3.

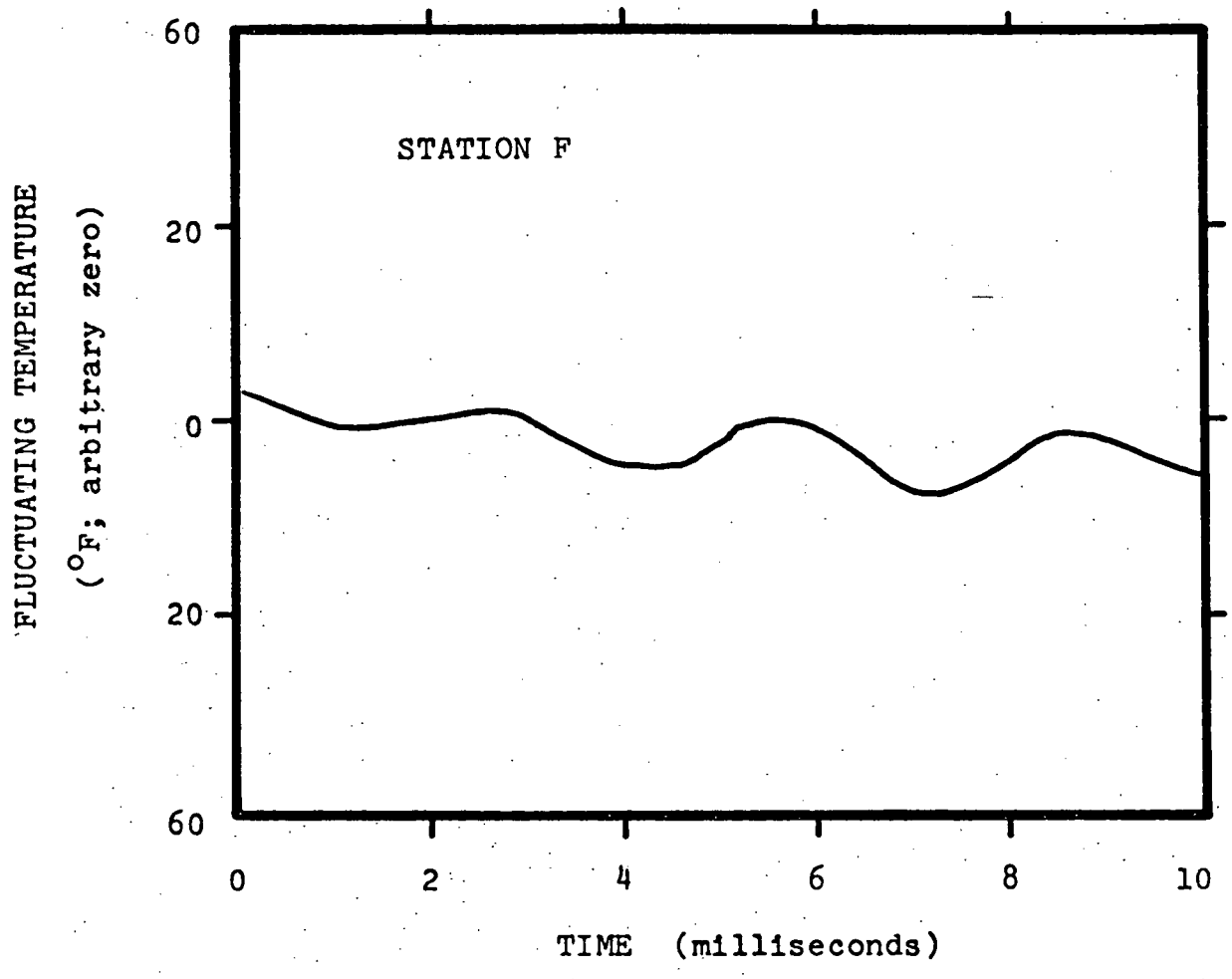

Fig. 4.5 Noise in the temperature analog; Re = 8300; no heating.

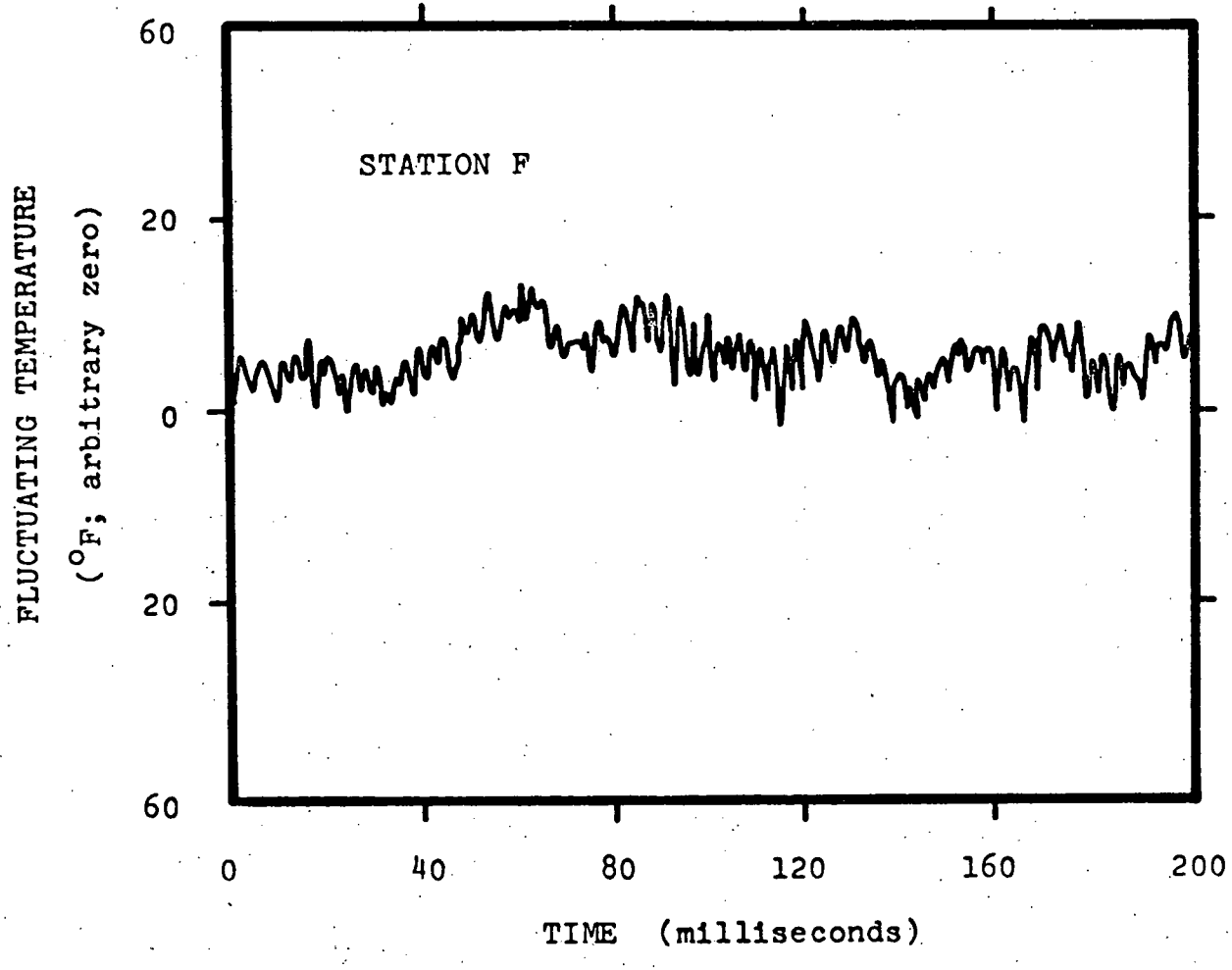

Fig. 4.6 Noise in the temperature analog; Re = 8300; no heating.

the shorter traces--compare Figures 4.5 and 4.6.

Fig. 4.7 illustrates the variable sensitivity of the measurement. A fringe maximum is represented by the top of the vertical scale; a fringe minimum is represented by the bottom of the vertical scale. The system is virtually insensitive to the temperature fluctuations when the signal hovers near the fringe maximum (or minimum) condition. It is most sensitive when the signal drifts down to the half-maximum condition, which occurs at 800 milliseconds on the trace.

4.1.2 Shear Layer Behavior

The temperature analog at Re = 5 000 is found to have a strong position dependence in the flow. The test cell is moved laterally 0.25 in. (0.64 cm) between stations A and A' on Fig. 4.8, which produces the traces of Figures 4.9 and 4.10. Fig. 4.10 has substantially more high frequency character than Figure 4.9. This illustrates that the flow possesses turbulent structure, at least in the shearing region. The traces of Figs. 4.9 and 4.10 have been observed on several independent runs. Evidence of the position dependence of the turbulent temperature structure at Re = 10 000 is presented in Section 4.1.3.

4.1.3 Flow Mapping at Re = 10 000

Figs. 4.11 through 4.17 show a flow mapping in the FFTF

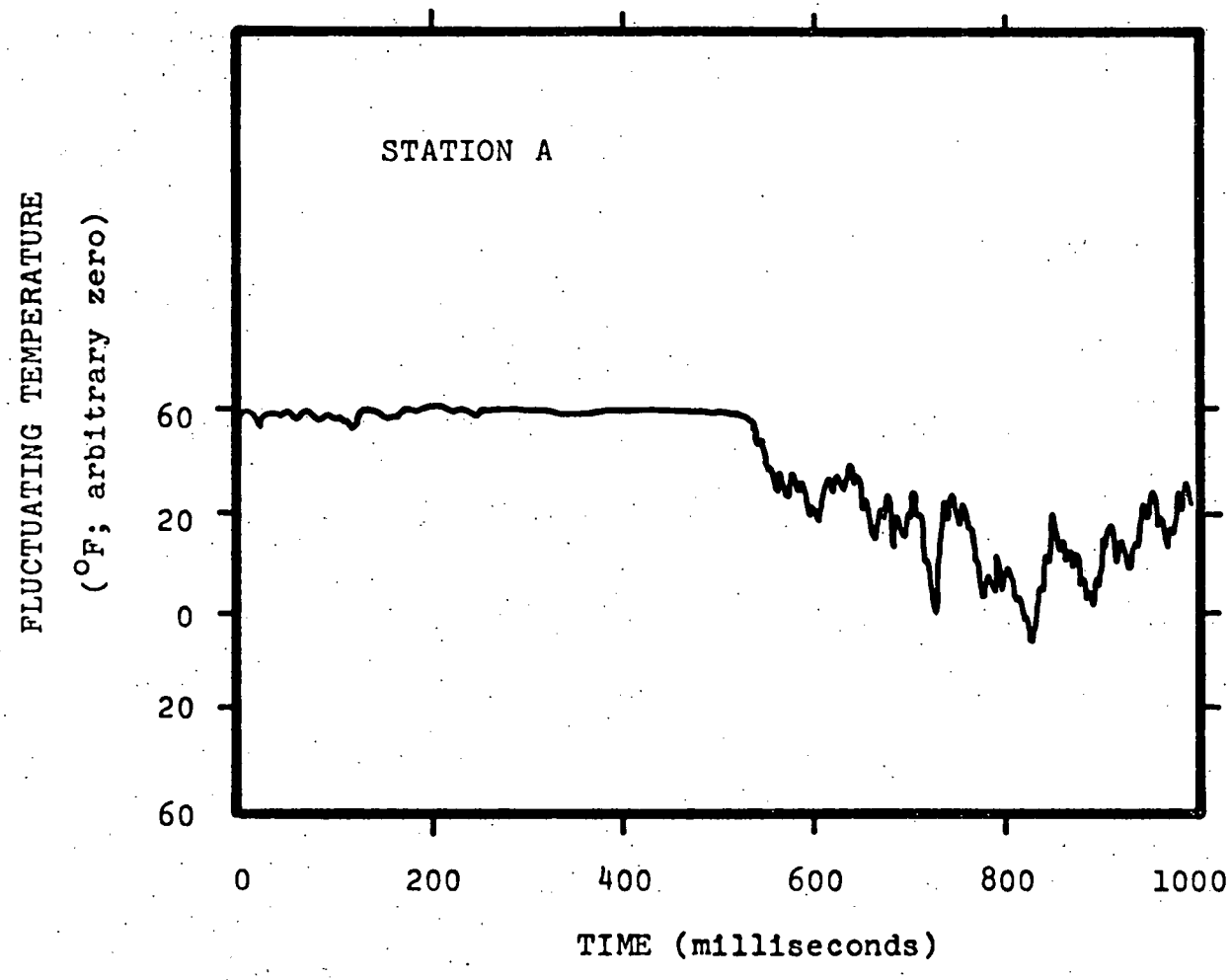

Fig. 4.7 Temperature trace showing low sensitivity near a fringe maximum (left hand side of trace), and high sensitivity at the half-maximum condition (right hand side of trace). Re = 4800; heated inlet at 165 °F.

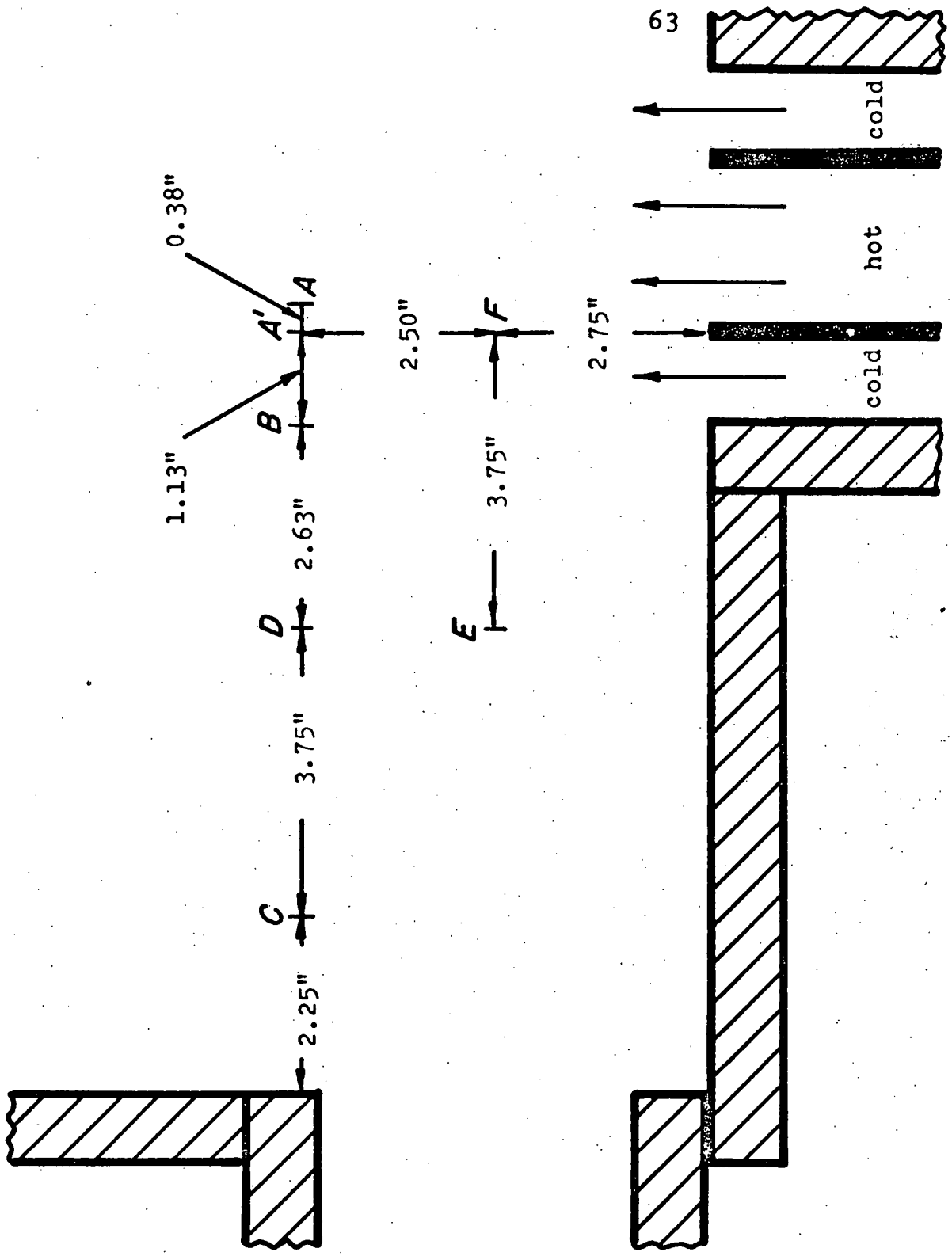

Fig. 4.8 Interferometric temperature measurement stations in the test cell.

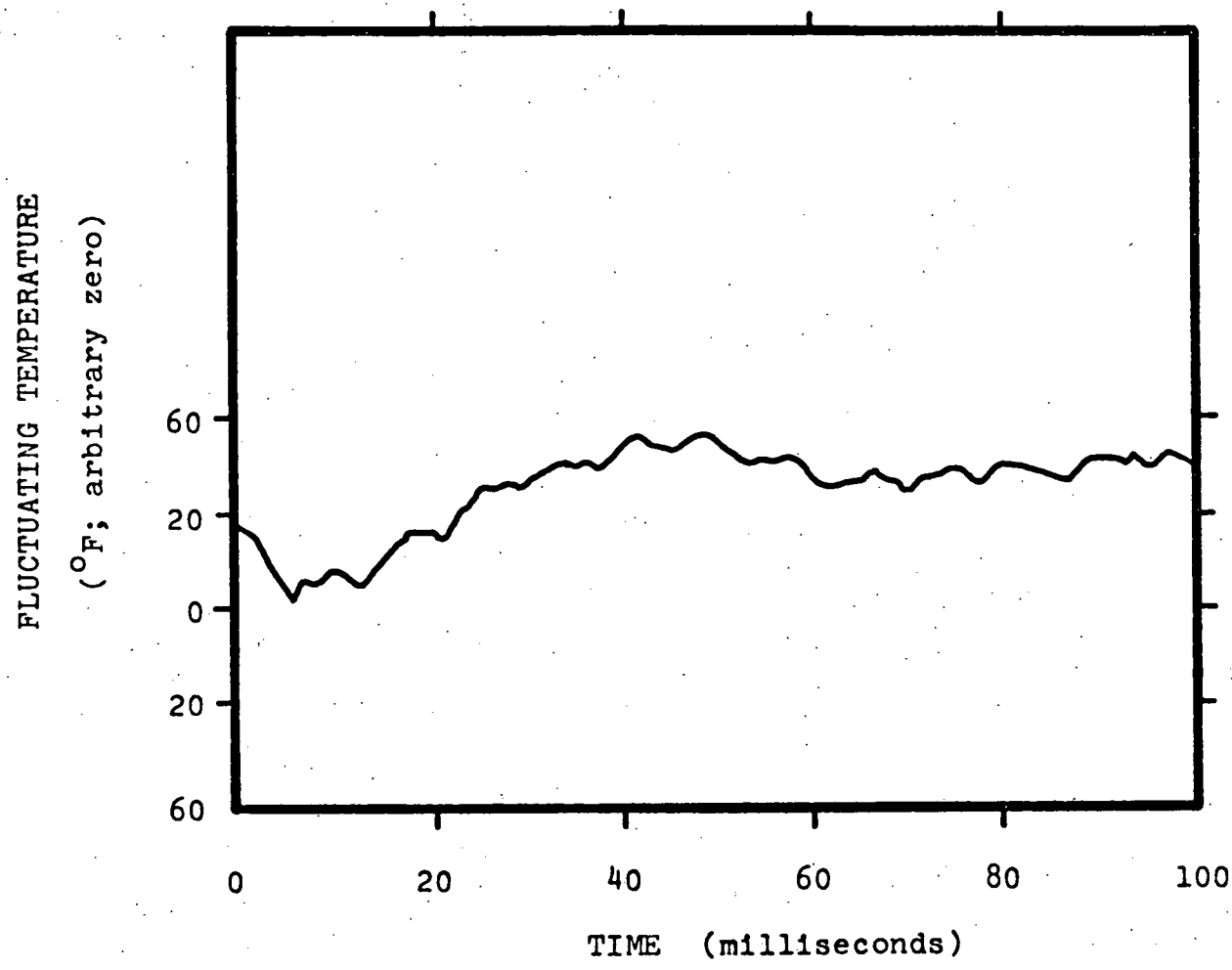

Fig. 4.9 Temperature trace at station A; Re = 5000; heated inlet at 155 °F.

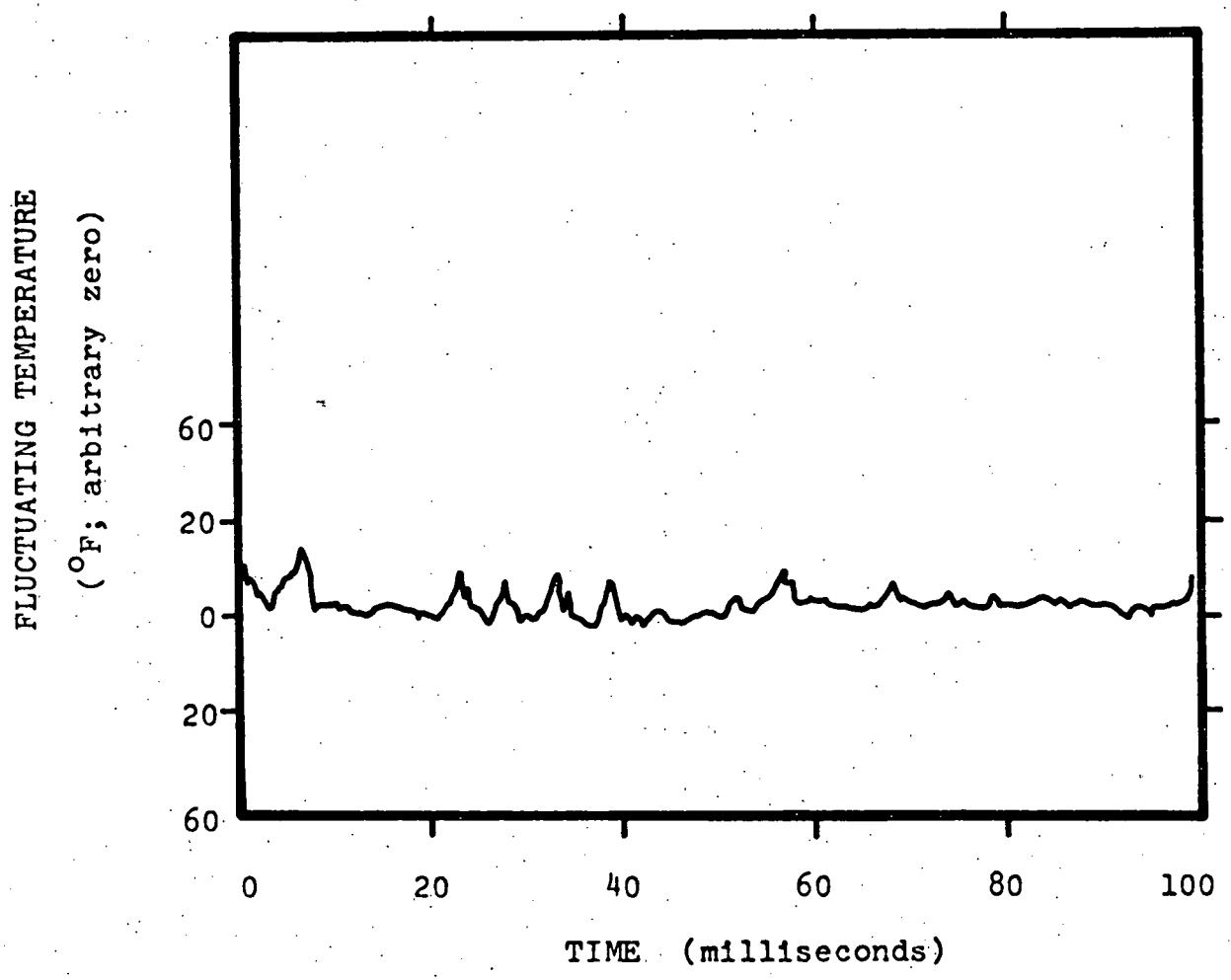

Fig. 4.10 Temperature trace at station A'; Re = 5400; heated inlet at 175 °F.

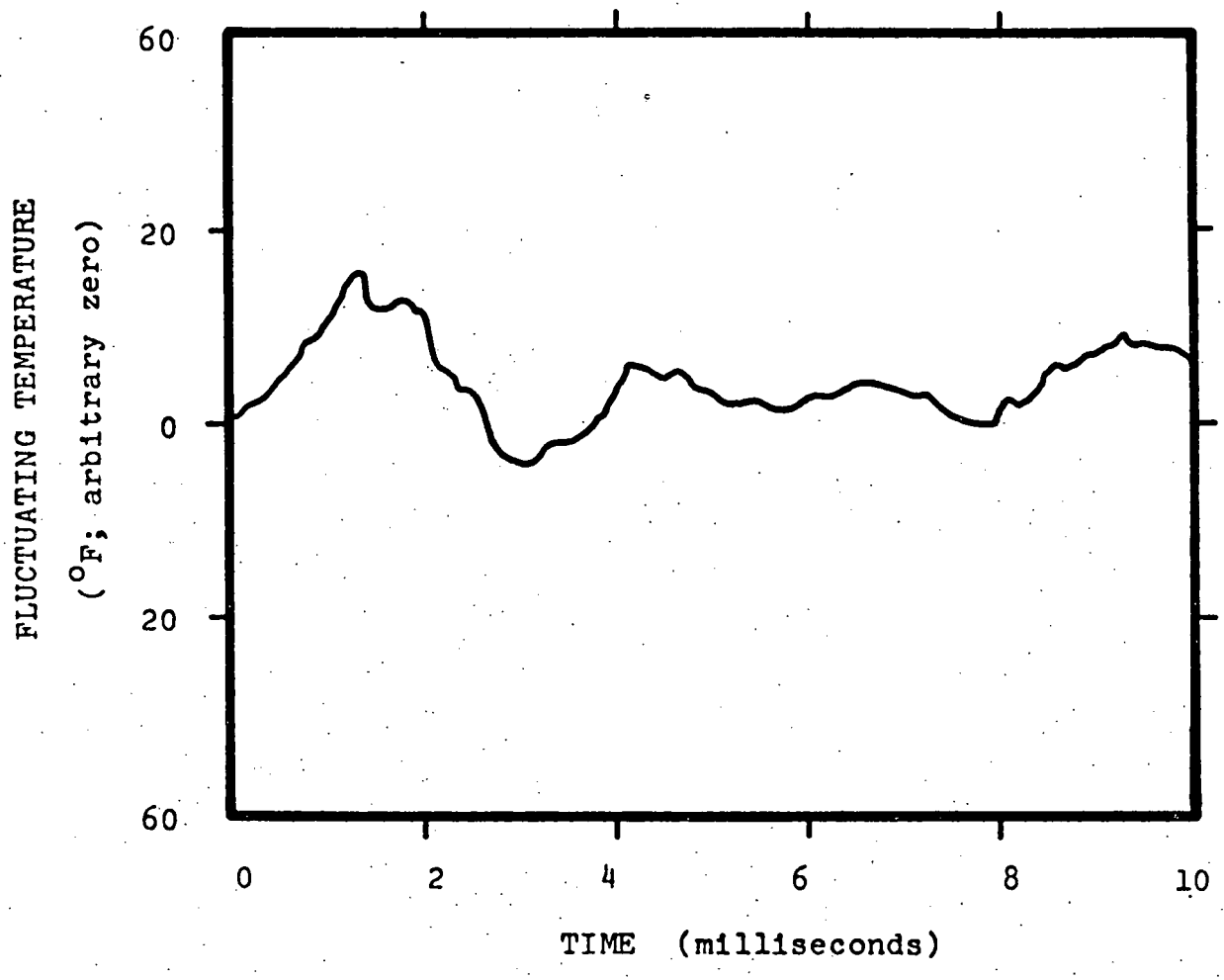

Fig. 4.11 Temperature trace at station A; Re = 8800; heated inlet at 140 °F.

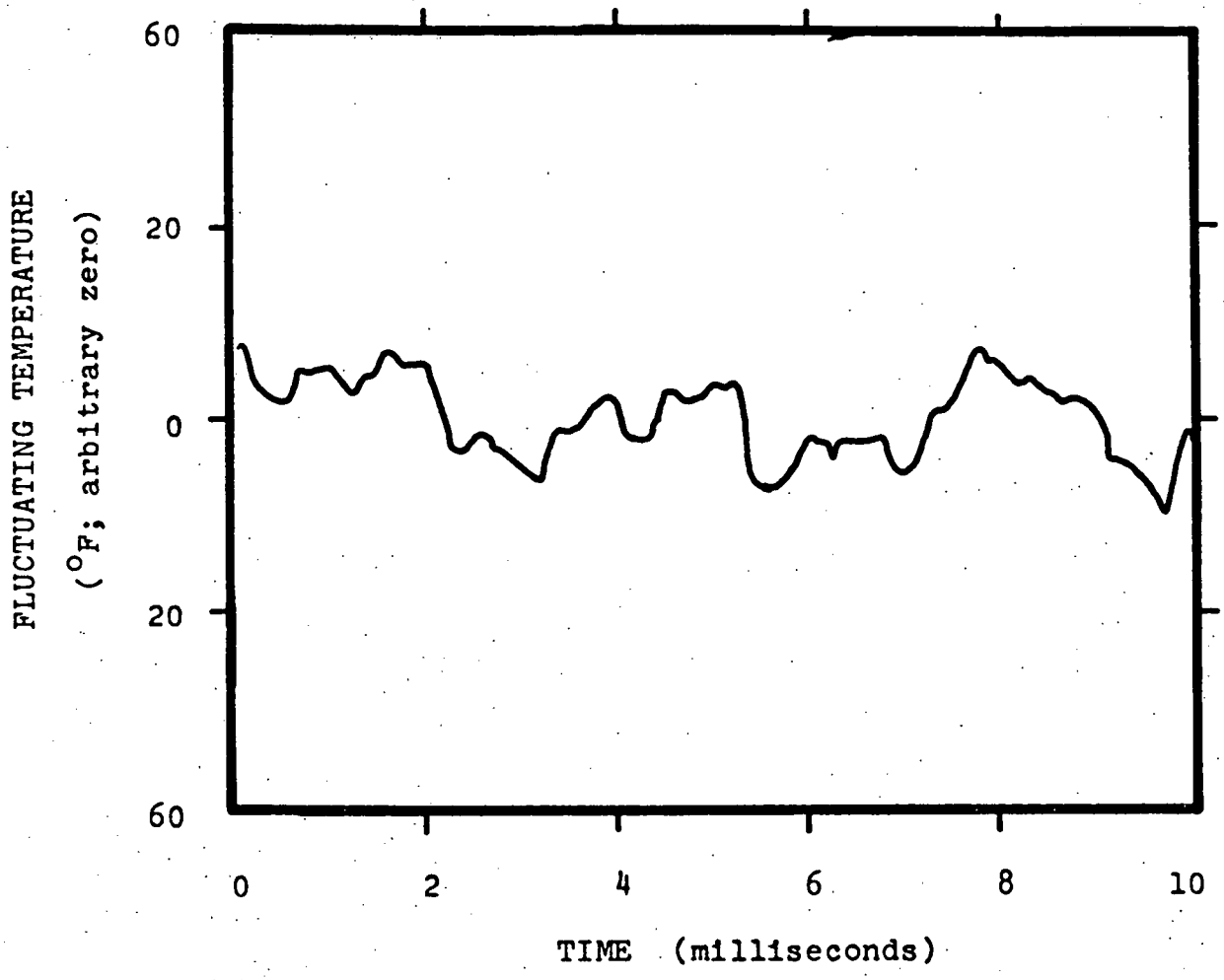

Fig. 4.12 Temperature trace at station B; Re = 9300; heated inlet at 150 ^{o}F.

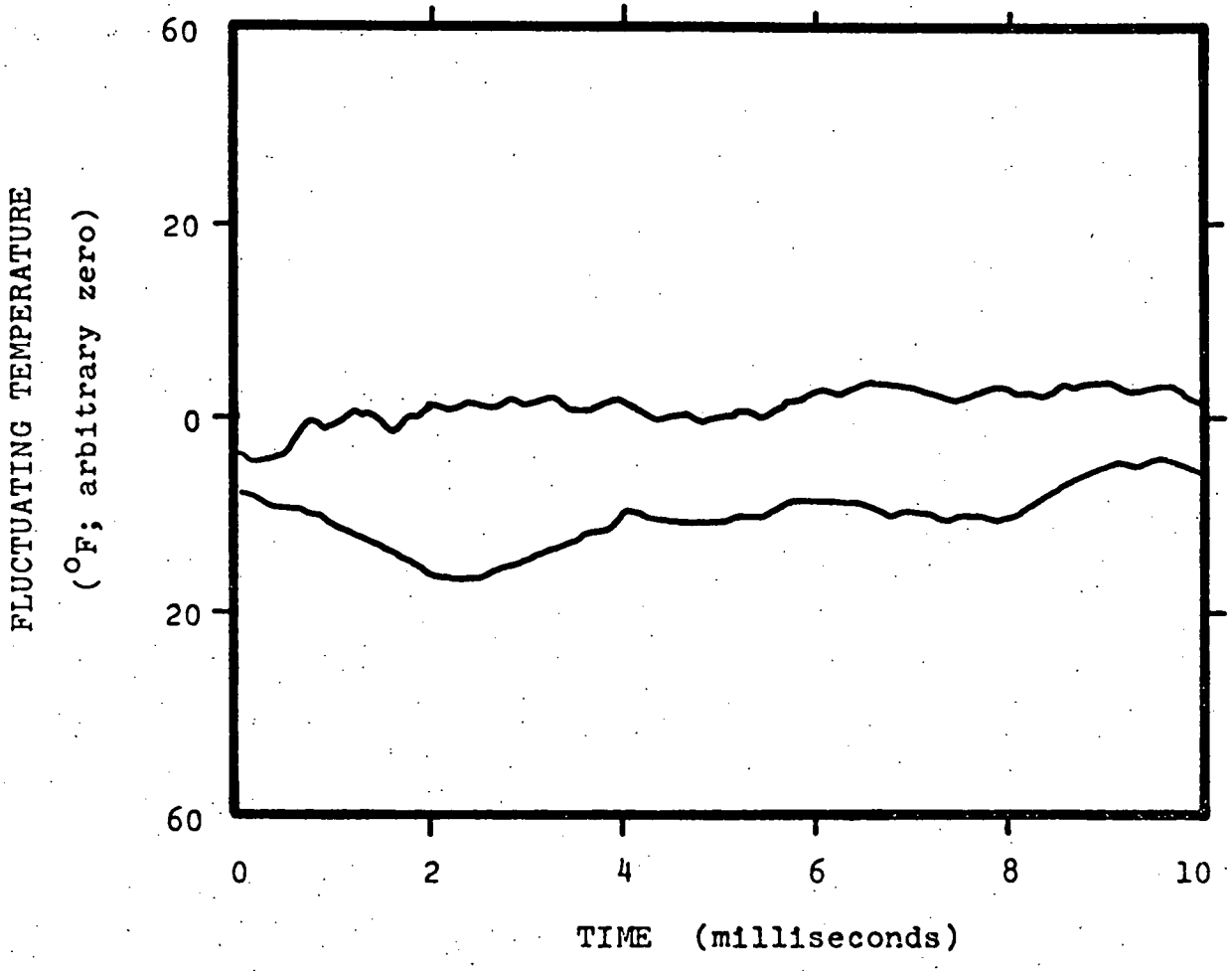

Fig. 4.13 Temperature trace at station C; Re = 9100; heated inlet at 155 °F.

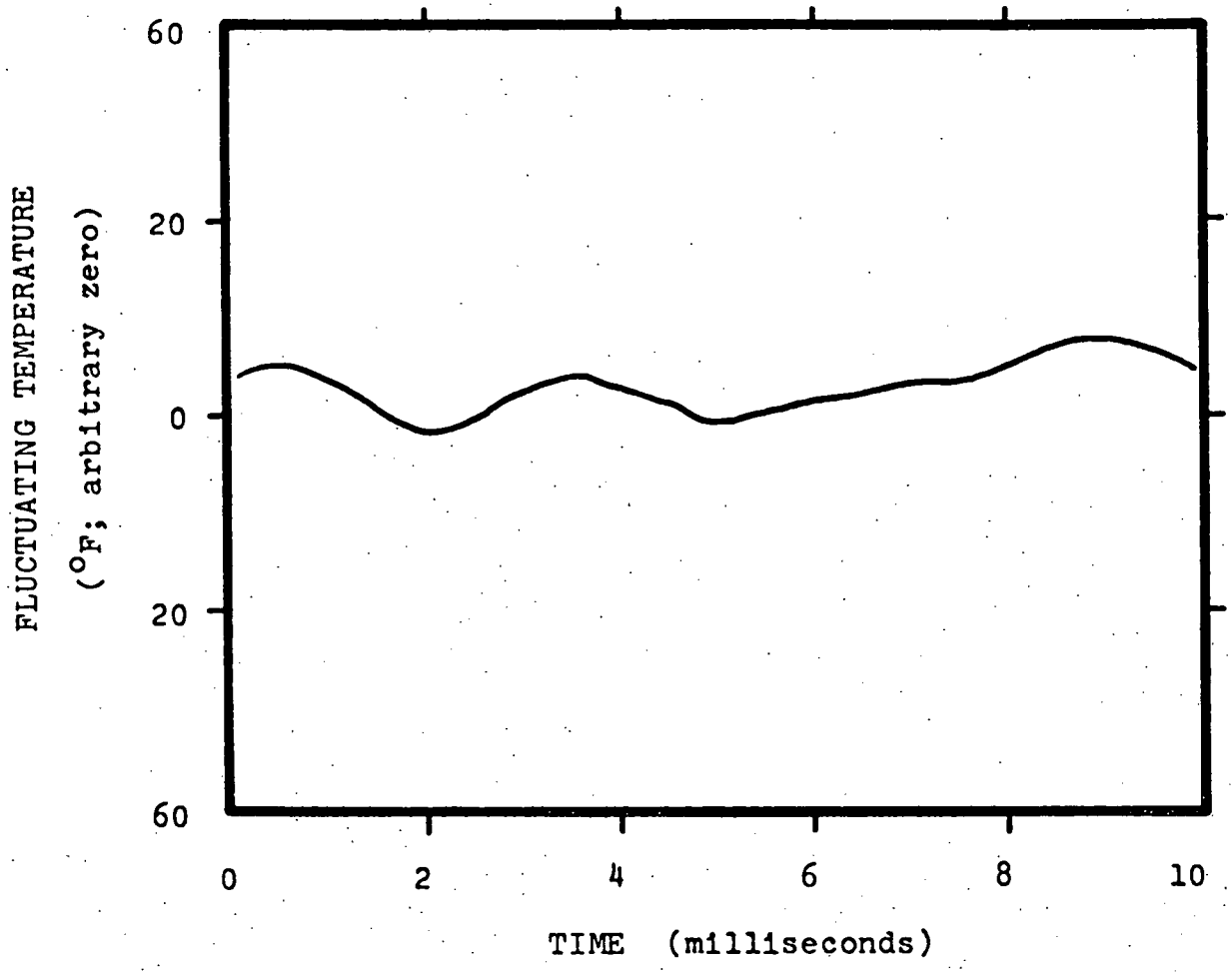

Fig. 4.14 Temperature trace at station D; Re = 8800; heated inlet at 150 °F.

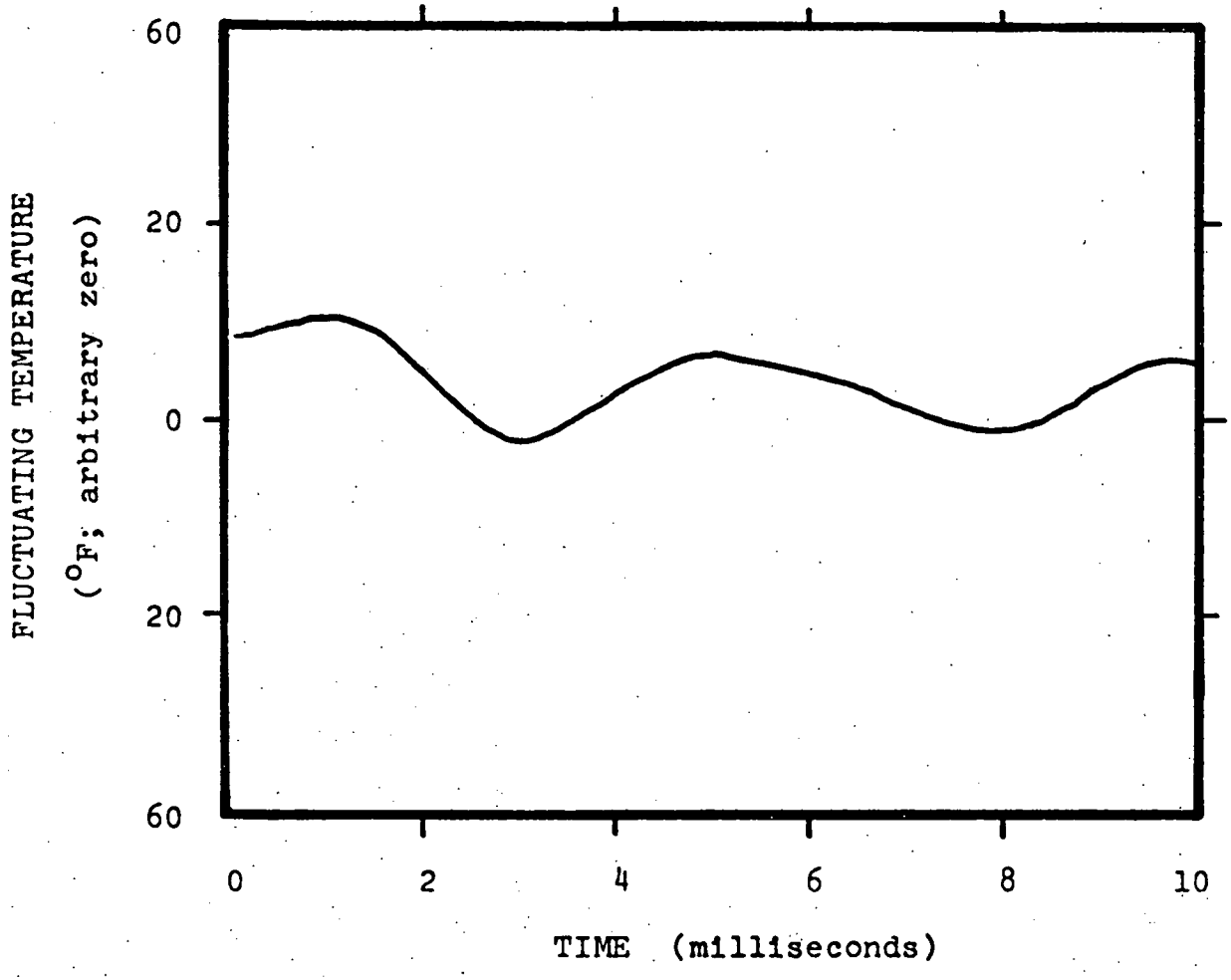

Fig. 4.15 Temperature trace at station E; Re = 9300; heated inlet at 150 ^{o}F.

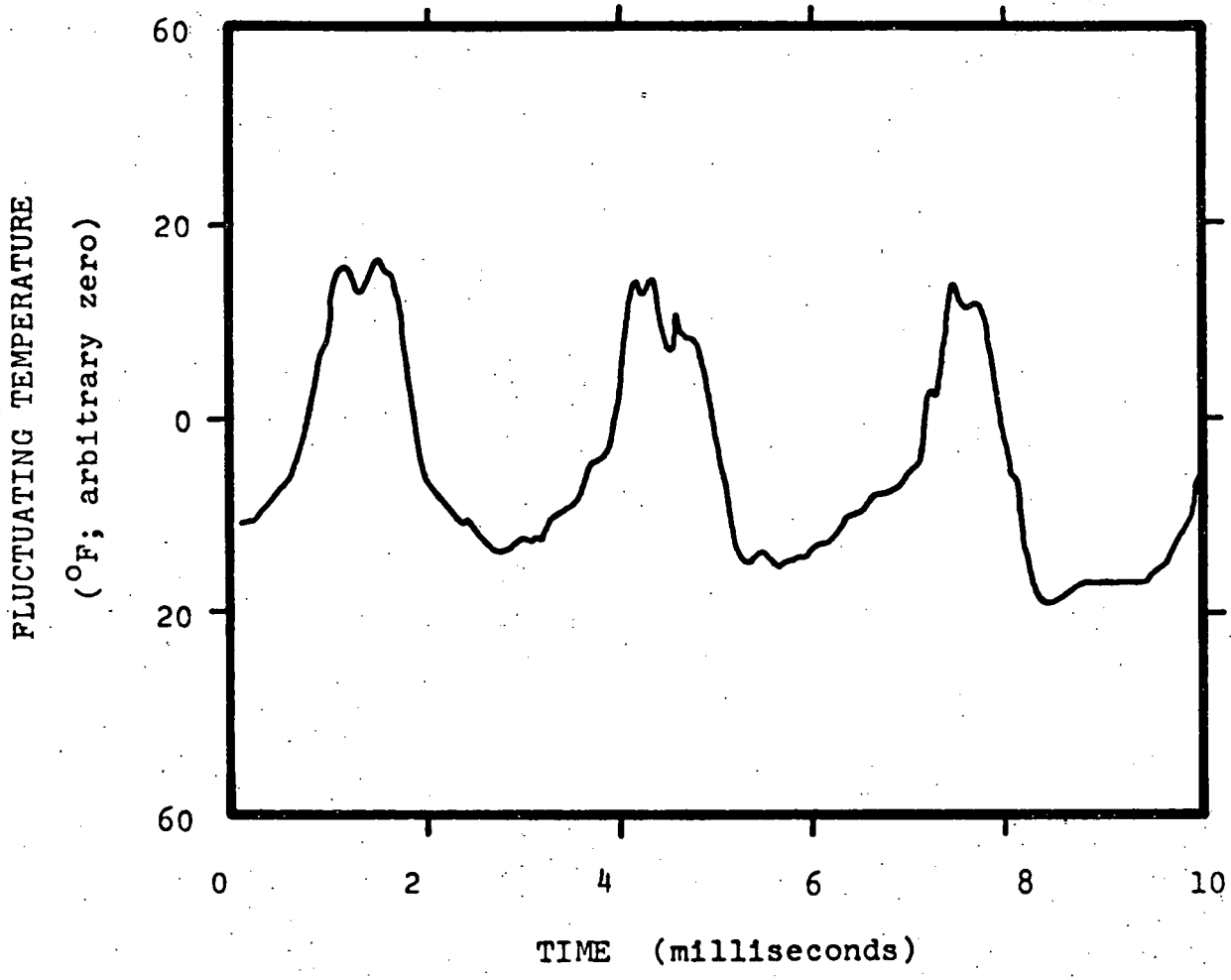

Fig. 4.16 Temperature trace at station F; Re = 8800; heated inlet at 150 °F.

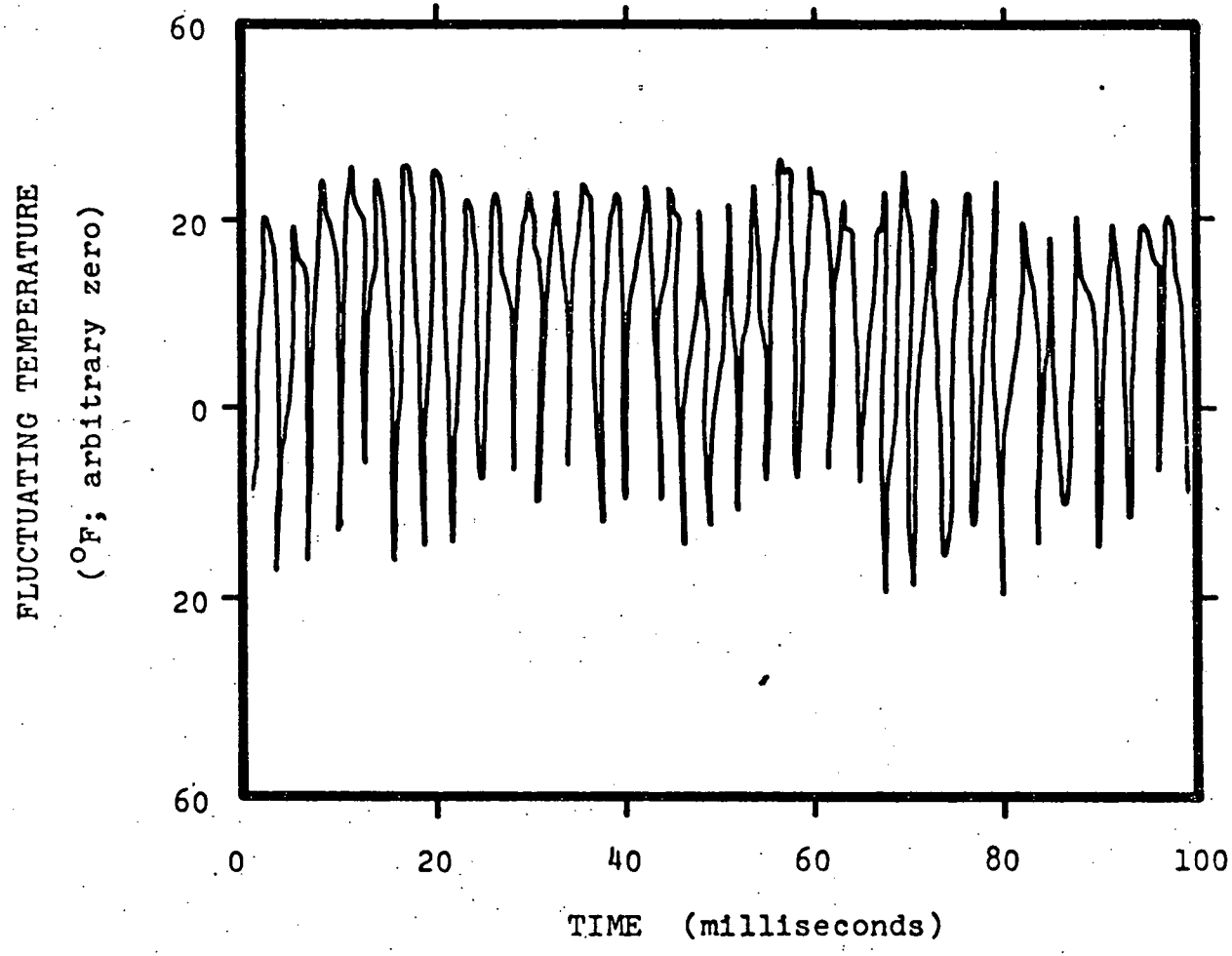

Fig. 4.17 Temperature trace at station F; Re = 9300; heated inlet at 150 °F.

model test cell at Re = 10 000. Fig. 4.8 serves as a key to the six measurement stations, A through F. Points A and B exhibit a large amount of turbulent mixing above the inlets. Point C, the next station along the streamlines of the recirculating flow, exhibits far less turbulence, and the next station, point E, shows no fluctuations above the background noise. Point D, in the "eye" of the recirculating flow, also exhibits no signal above background. Point F, which lies directly beneath point A', exhibits a remarkably strong component at about 300 Hz. The traces at station F are suggestive of the (initially) regular breakup of a shear flow. The traces of points A and B, just 2.5 in. (6.4 cm) above point F, are examined further for their residual 300 Hz component in Section 4.2.2.

4.1.4 Forced and Free Convection

A simple demonstration of forced versus free convection is presented here. The natural convection flow is established in the following way. After the hot leg is heated in the normal way, the blower is turned off. The result is that a reservoir of hot, still air exists at the heated inlet, with cool, still air at the ambient inlets. The flow is driven solely by bouyant forces, and the temperature analog is recorded in the usual way. The traces of Figs. 4.18 and 4.19 at station A in the flow illustrate the very different time

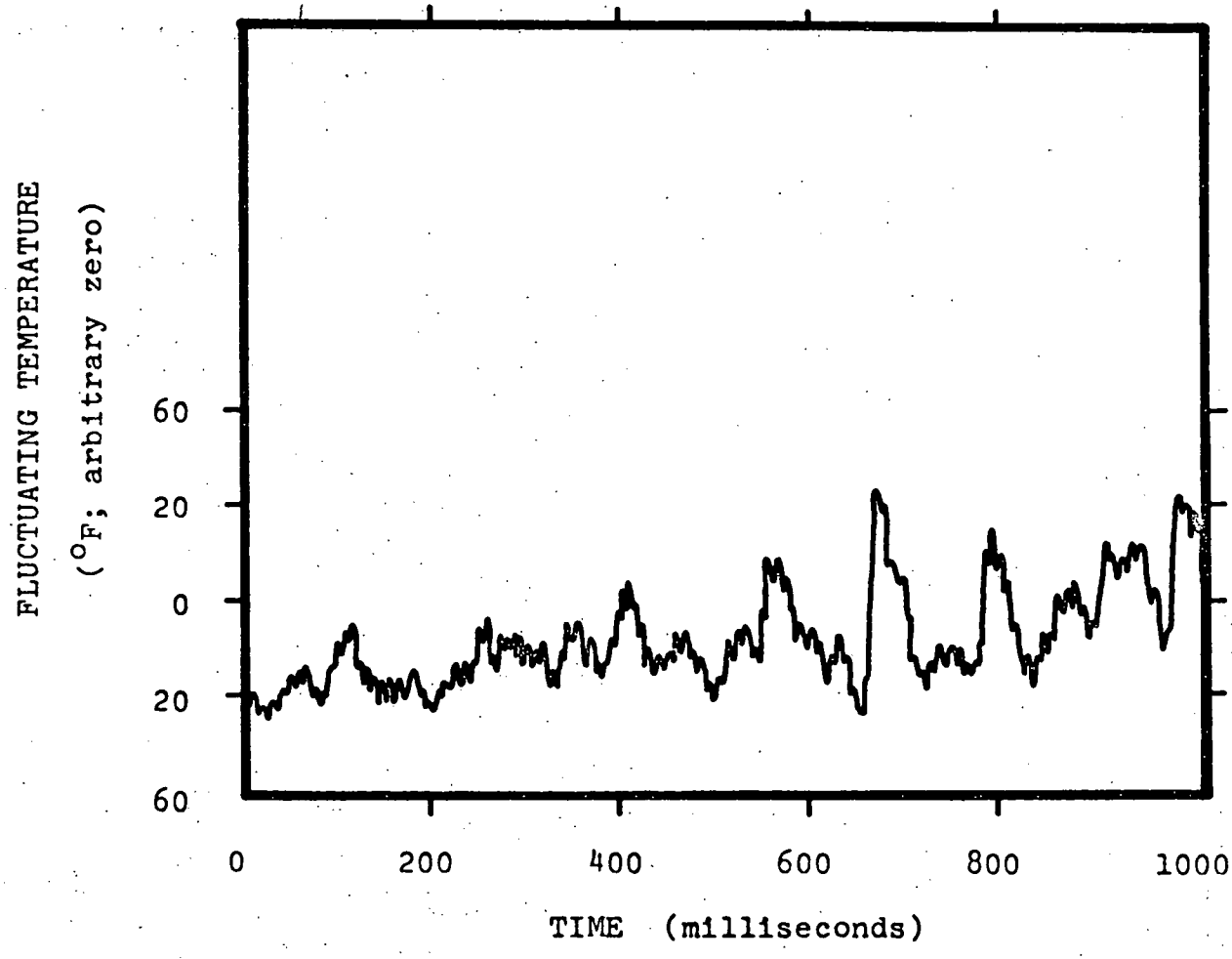

Fig. 4.18 Temperature trace during forced convection; Re = 4800.

Compare with Figure 4.19. This data is from station A'.

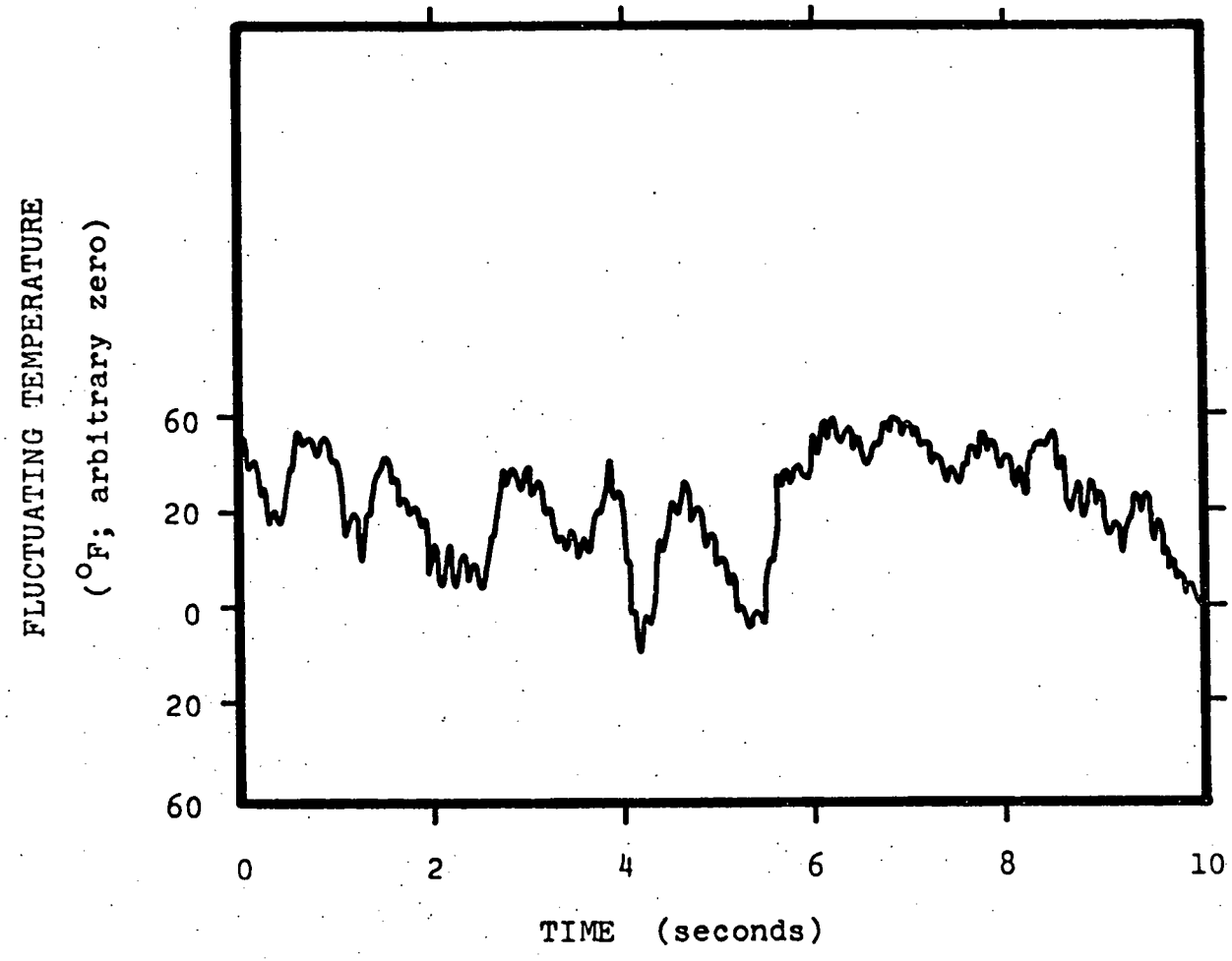

Fig. 4.19 Temperature trace during free convection; Re = 0. Note the extremely long 10 second duration of the trace, and compare with Figure 4.18. This data is from station A'.

scales of mixing in forced and free convection. Although the traces appear to be very similar, the free convection trace is fully ten times slower than the forced convection trace. Incidentally, the slight ripple in the trace of Fig. 4.18 is the 120 Hz motor noise, and the slight ripple in Fig. 4.19 is the regular shaking of the building.

4.1.5 Autocorrelations

The autocorrelation of the temperature trace in Fig. 4.10 appears in Figure 4.20. The most prominent feature of Fig. 4.20 is the ringing in the autocorrelation. It is indicative of a strong single frequency--about 300 Hz--in the signal. The scatter of the data of Fig. 4.20 at times greater than 90 milliseconds is discussed in Section 3.3. This technique for constructing an autocorrelation is not considered sufficiently accurate, due to insufficient sampling, to warrant the deduction of an integral time scale; this is made difficult because of the strong ringing. Similarly, the autocorrelation technique is not accurate enough to warrant the deduction of the microscale of time, which depends upon the second derivative of the autocorrelation function at $\tau \rightarrow 0$.[17] Recall that the autocorrelation and the power spectral density form a Fouier transform pair; they contain the same information in different form.

4.2 Power Spectral Density Studies

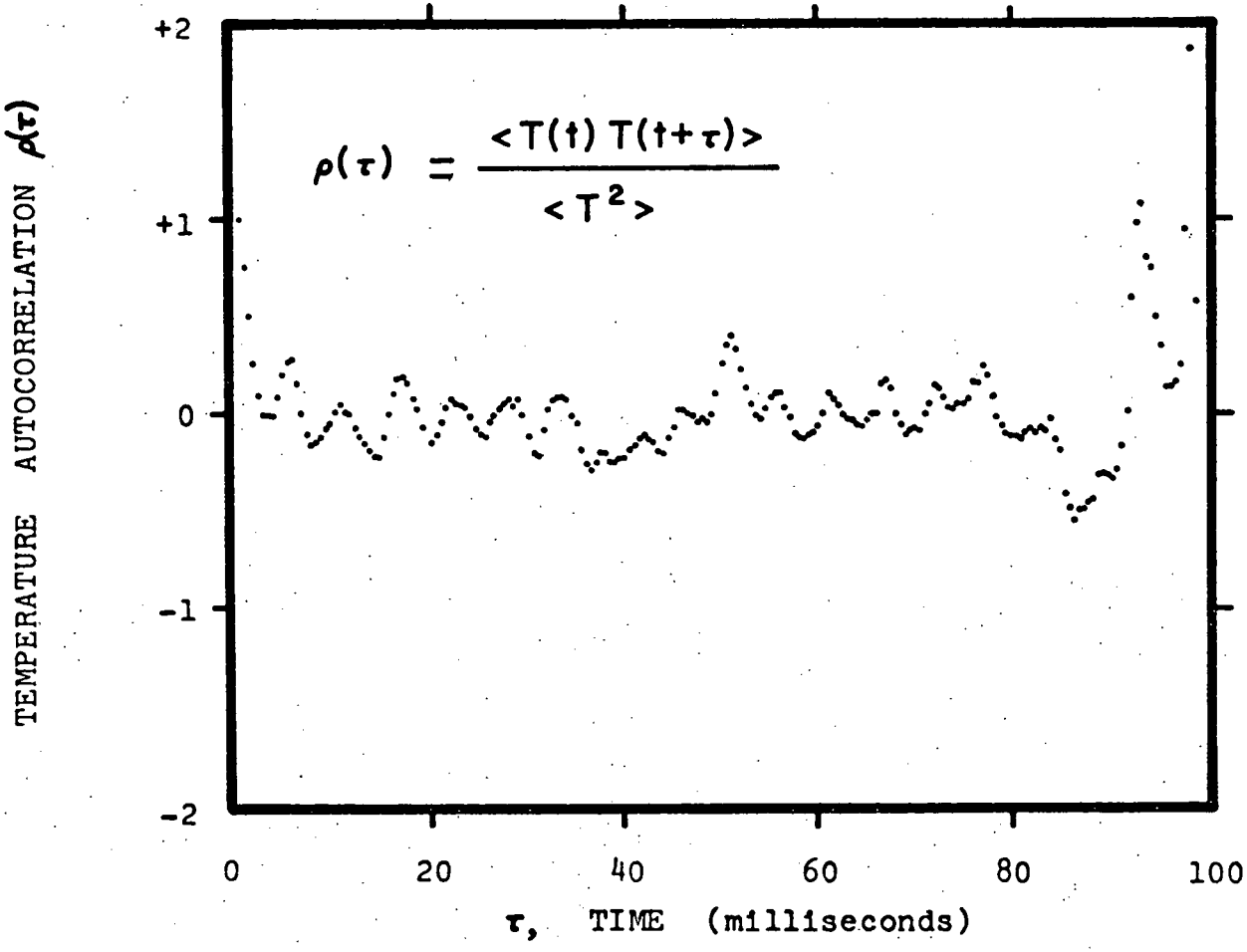

Fig. 4.20 Plot of the autocorrelation of the temperature trace in Fig. 4.10. The autocorrelation is calculated on a computer with a digitalized version of Fig. 4.10. The autocorrelation is quoted in the figure, where τ is the autocorrelation variable.

4.2.1 Noise and Errors

The noise in the power spectral density (PSD) studies originates from a variety of sources. The sources and their spectral bandwidths are illustrated in Figure 4.21. A troublesome inlet manifold vibration at the flow rates above Re = 10 000 has limited the experiments to being run below this Reynolds number. The frequency analysis is found to be very noise-free above 500 Hz.

The error in the RMS amplitude display of the frequency analyzer is about $\pm$10 %. Subsequent squaring of the RMS amplitude yields an error of $\pm$20 %. The subtraction of a background curve yields an error of $\pm$28 % in the final PSD curve. Furthermore, the PSD curves must be normalized to unit area, but the full range of the curve is not quite known --especially from 0 Hz to several hundred Hz. This affects the results in a small, but unknown way. Also note that the error in the measurements which drop below the sensitivity of the analyzer becomes equal to the measurement itself. For example, the background trace in Fig. 4.22 above approximately 1 kHz drops below the analyzer sensitivity. In this way, the high frequency tails are generally more subject to error than the low frequency shoulders in the PSD curves.

4.2.2 Power Spectral Density Mapping

The PSD is mapped for Re = 10 000 at four points in the

Fig. 4.21 Frequency bandwidths of the components in the temperature analog.

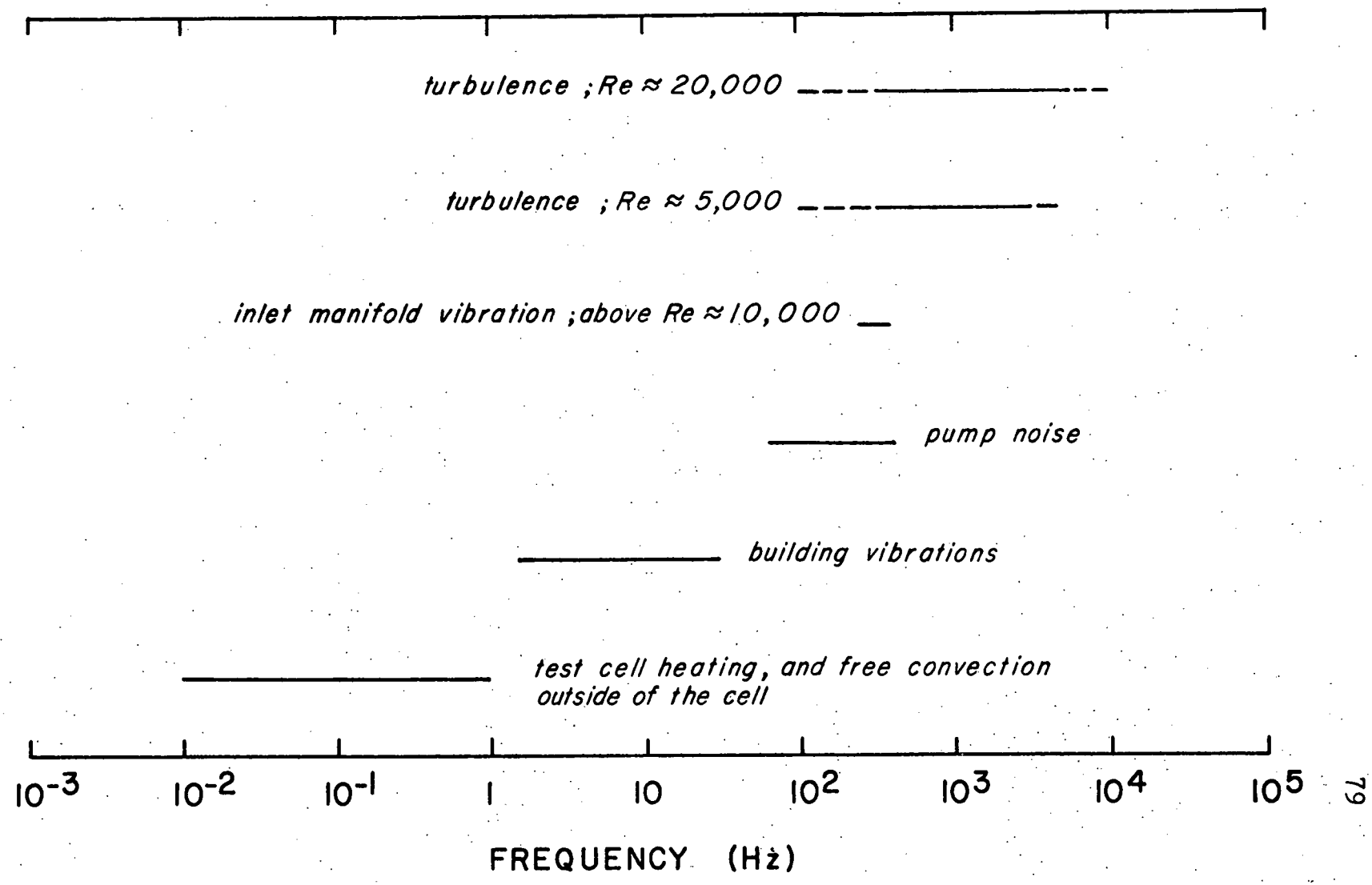

flow, as shown in Figures 4.22 through 4.29. Figs. 4.22, 24, 26, and 28 show the smoothed temperature spectra in the upper curves, and the smoothed background spectra in the lower curves. Each of the background curves are subtracted from the signals above them, the resultant curves are normalized to unit area and plotted in Figs. 4.23, 25, 27, and 29, respectively. A 300 Hz component, and its 600 Hz harmonic, are abundant in the data of point F. A reduced 300 Hz component is found at point B. An even smaller 300 Hz component is present at station A, and no measurable component is detected at station C. Points D and E experience no temperature fluctuations above background. These results agree with the average temperatures at the stations given in Table 4.1.

4.2.3 Effect of Increasing Temperature Upset

The effect of the inlet temperature upset is demonstrated in Figure 4.30. As the hot leg temperature rises above the 65 ^{0}F ambient air temperature, the relative mean-square fluctuations increase broadly over all of the sampled frequencies. When the curves are plotted as PSD curves in Fig. 4.31, the temperature upset has no definite effect on the PSD of the turbulence. That is, the temperature upset does not drive any measurable instabilities in the flow with bouyant forces.

The information foregone by normalizing the PSD curves

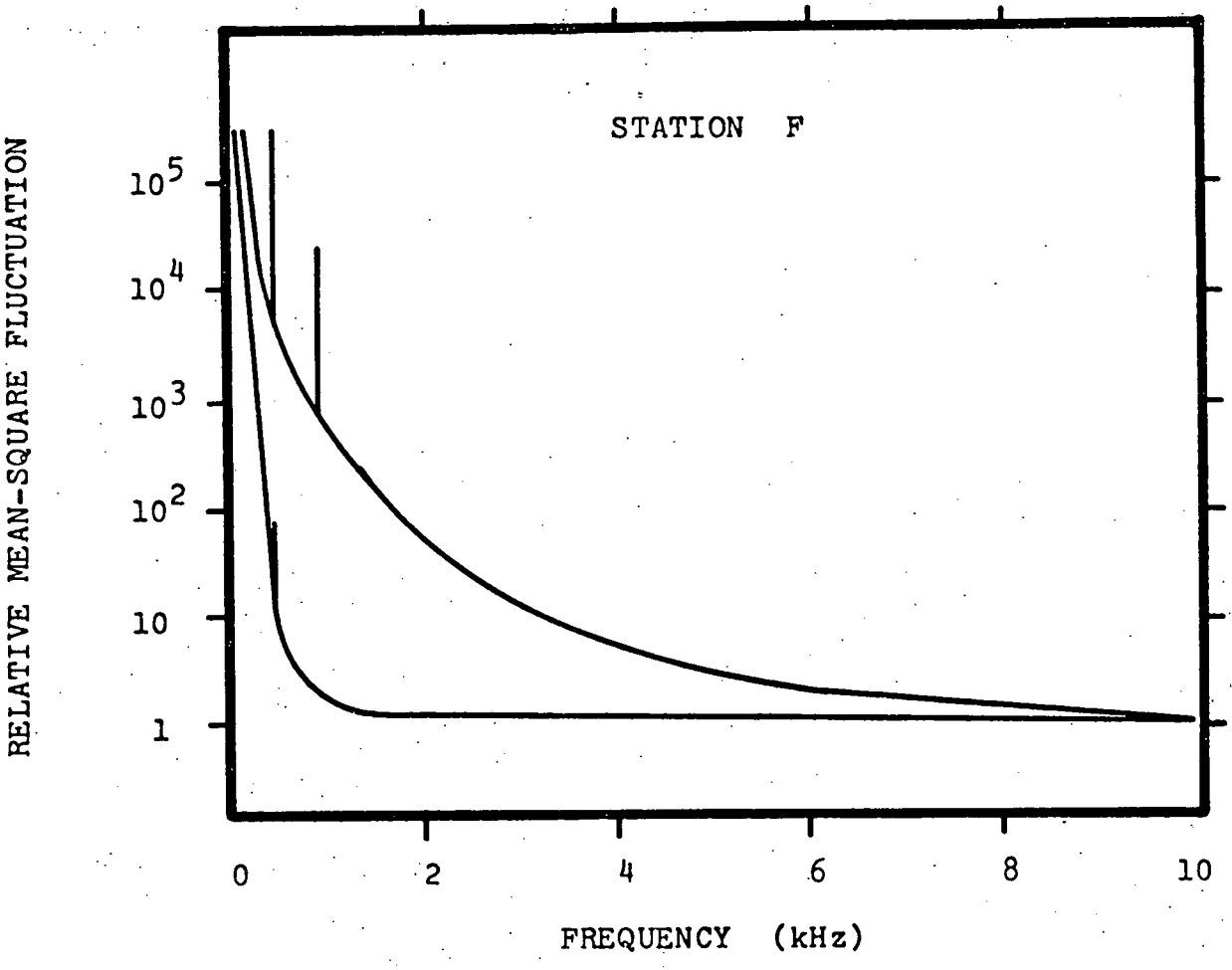

Fig. 4.22 Smoothed curves of the photographs of the relative RMS fluctuation, plotted as mean-square fluctuation. Lower trace--background spectra; upper trace--temperature spectrum.

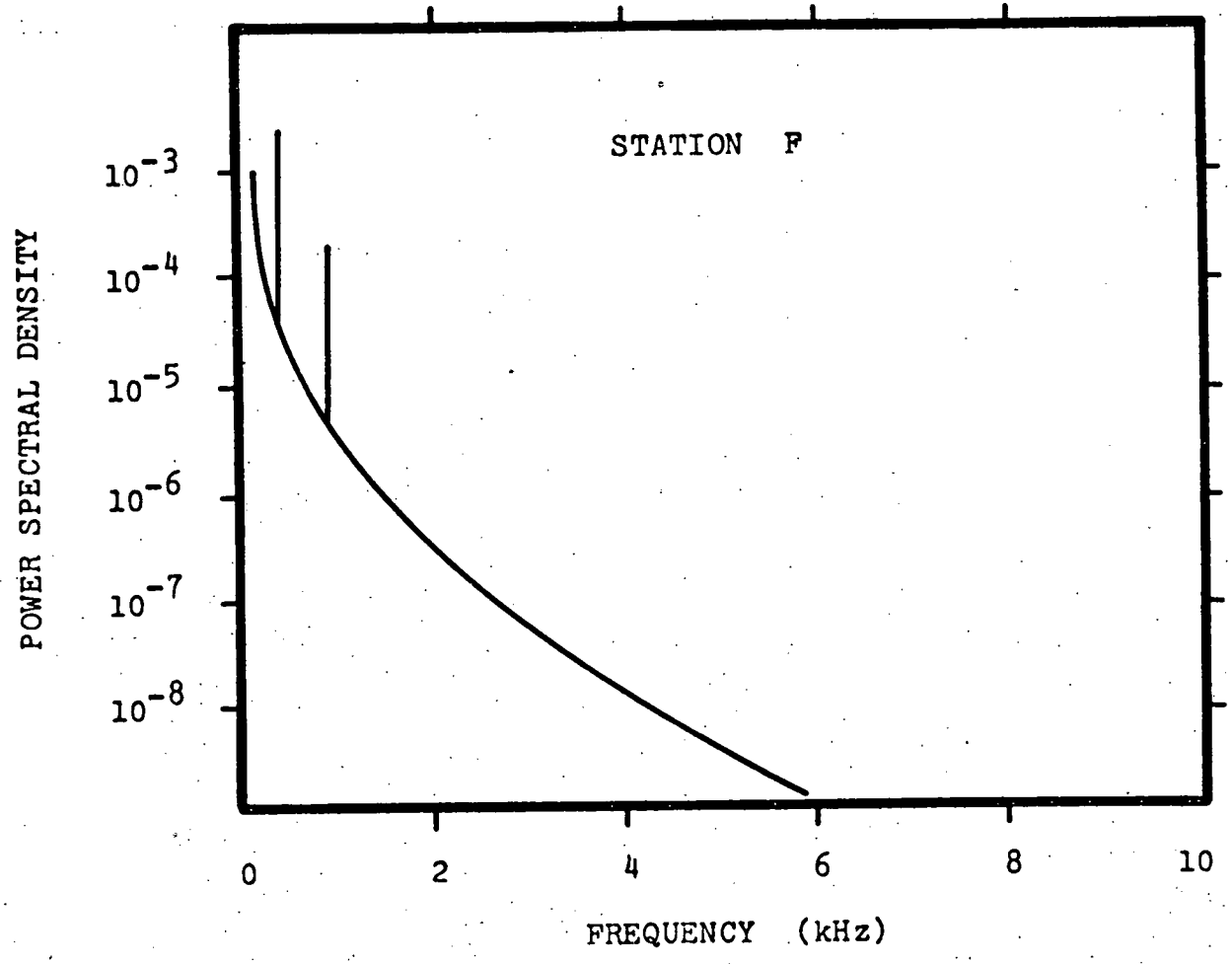

Fig. 4.23 Power spectral density curve; Re = 8800; heated inlet at 153 ^{o}F.

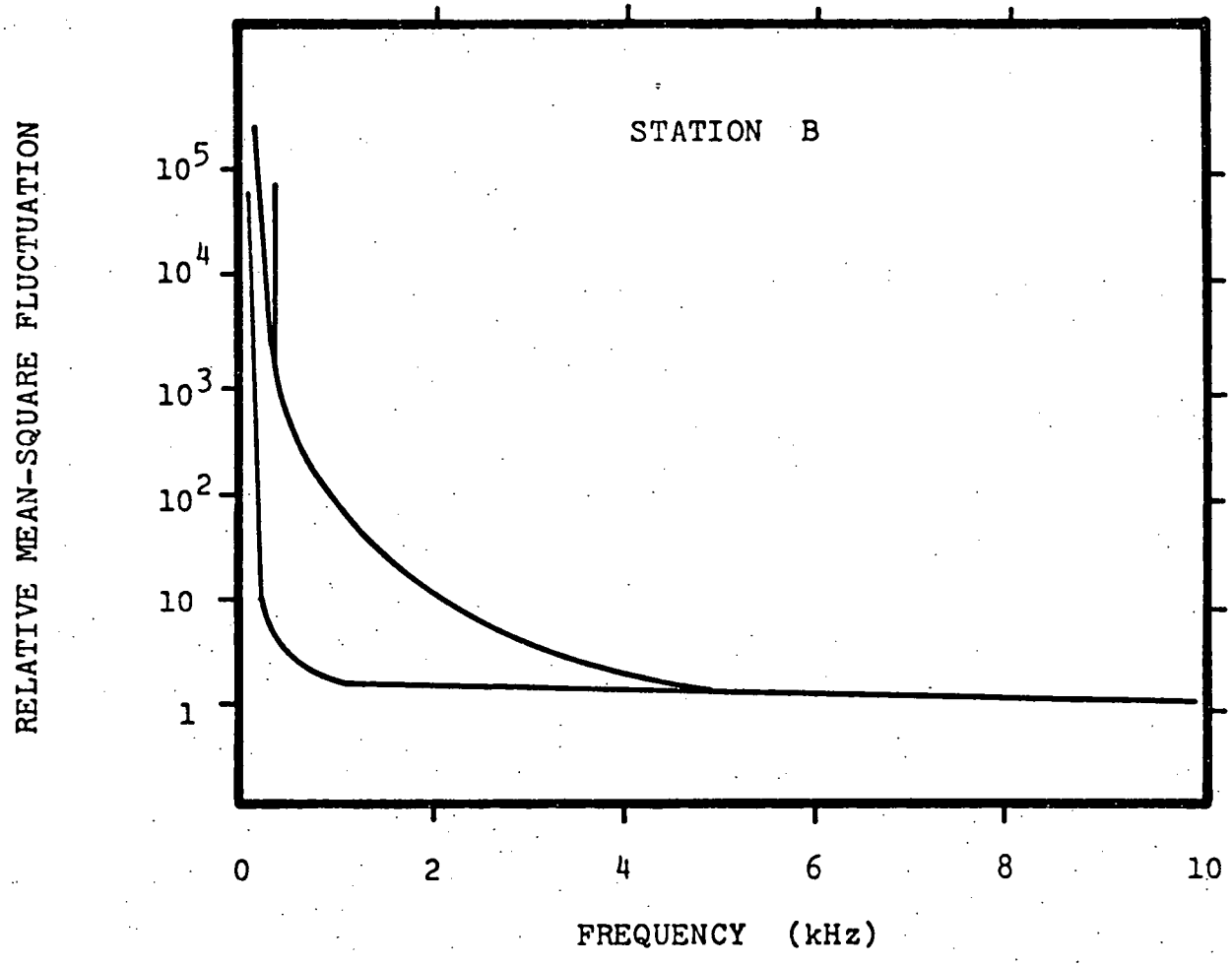

Fig. 4.24 Smoothed curves of the photographs of the relative RMS fluctuation, plotted as mean-square fluctuation. Lower trace--background spectrum; upper trace--temperature spectrum.

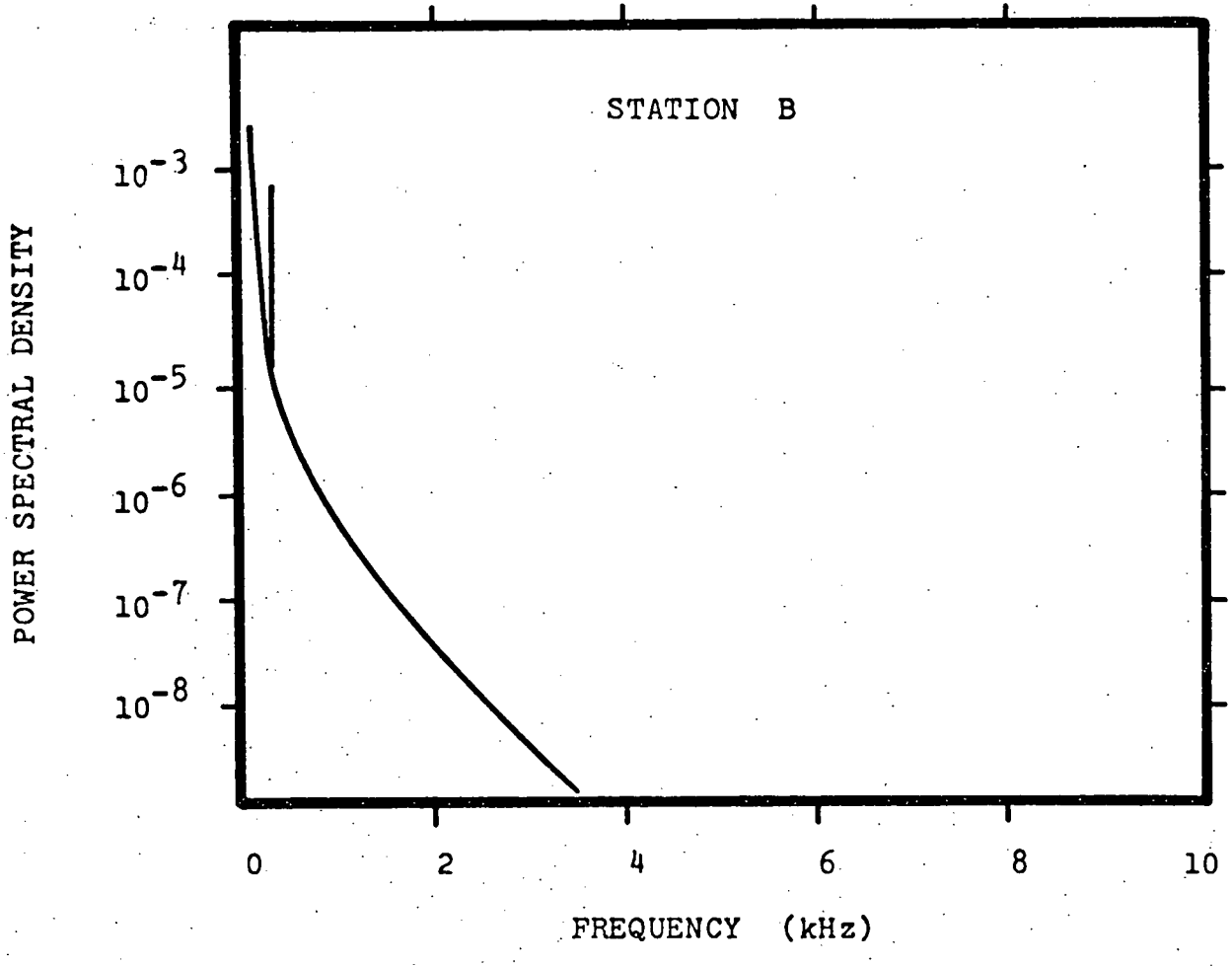

Fig. 4.25 Power spectral density curve; Re = 8800; heated inlet at 145 ^{o}F.

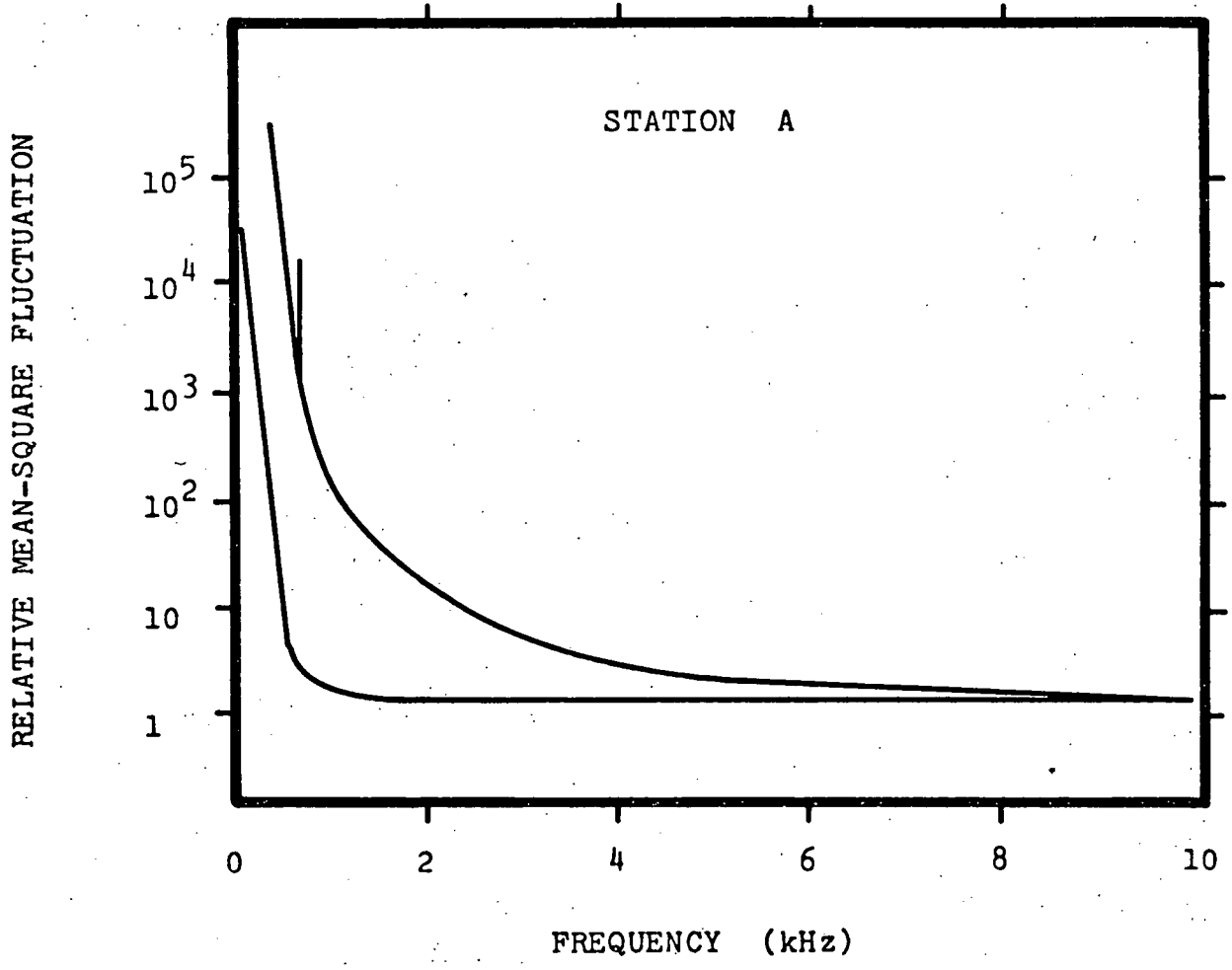

Fig. 4.26 Smoothed curves of the photographs of the relative RMS fluctuation, plotted as mean-square fluctuation. Lower trace--background spectrum; upper trace--temperature spectrum.

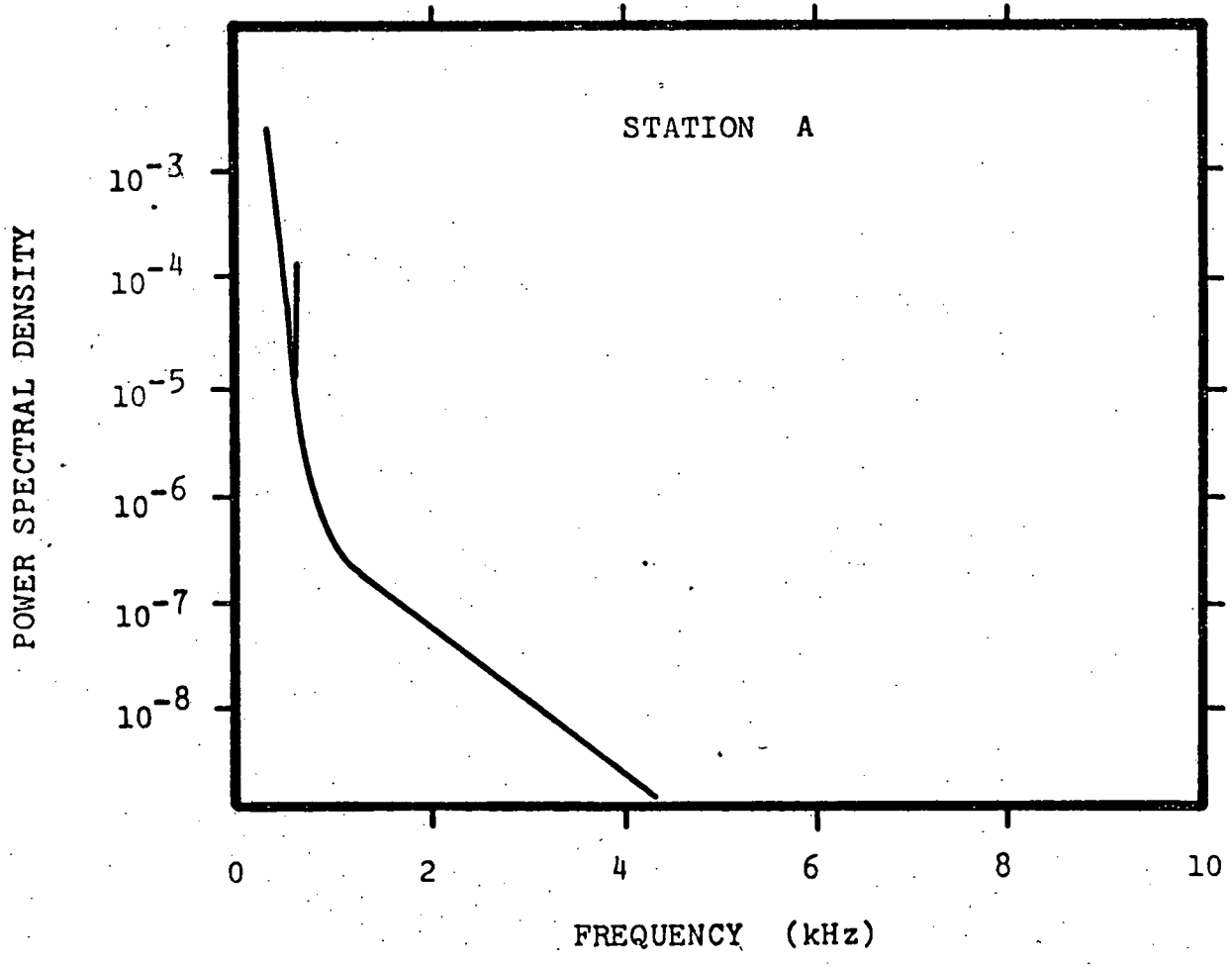

Fig. 4.27 Power spectral density curve; Re = 9300; heated inlet at 148 °F.

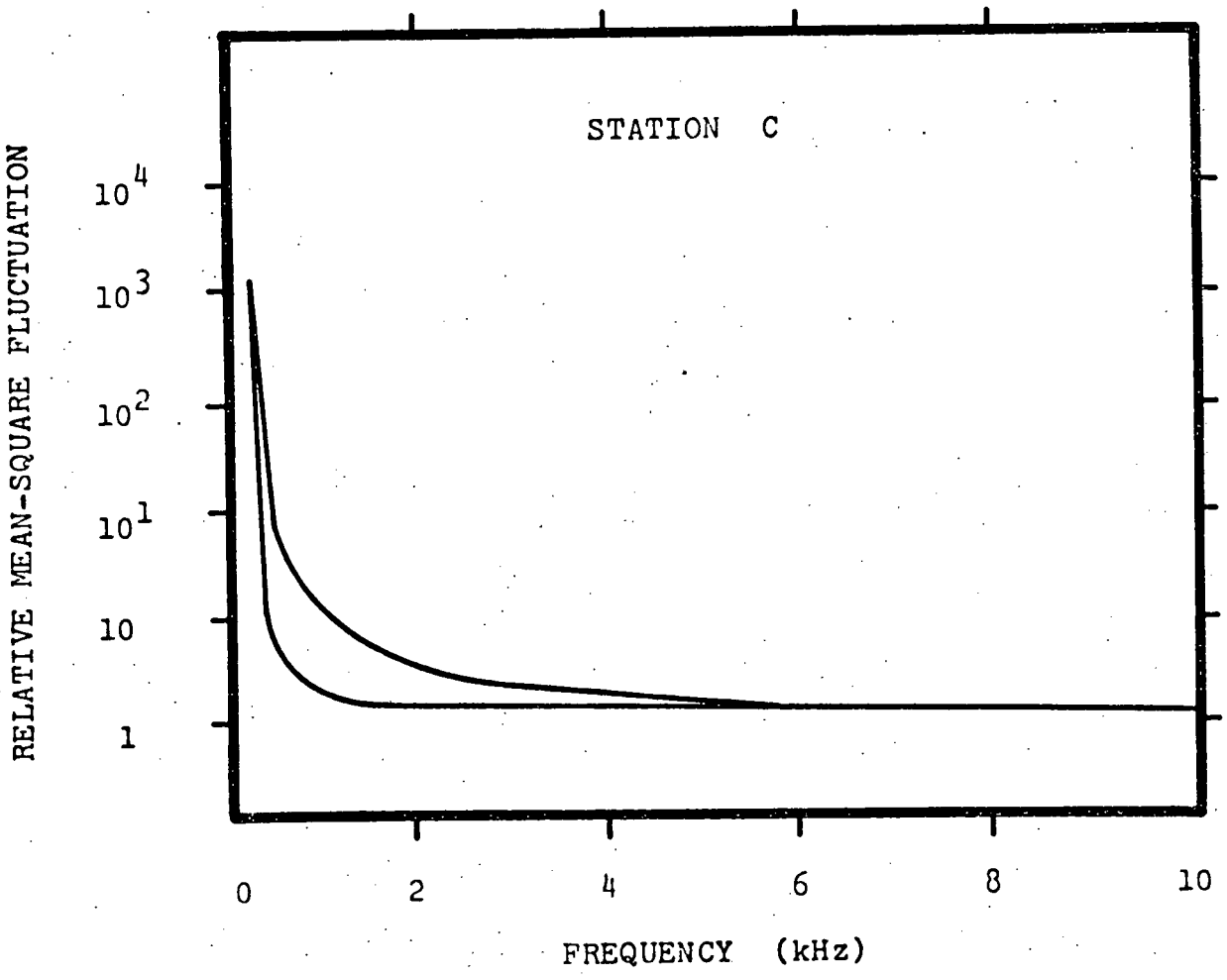

Fig. 4.28 Smoothed curves of the photographs of the relative RMS fluctuation, plotted as mean-square fluctuation. Lower trace--background spectrum; upper trace--temperature spectrum.

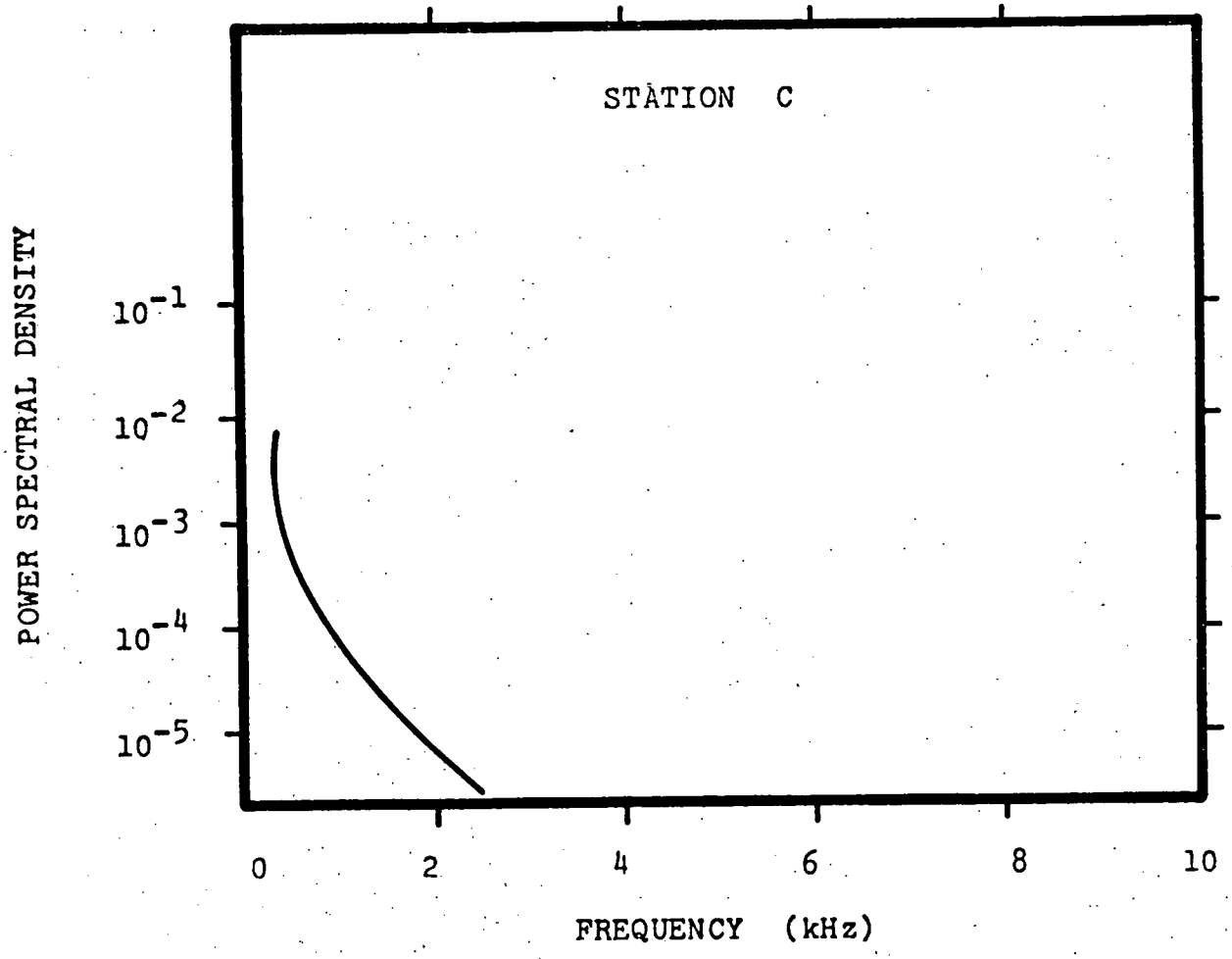

Fig. 4.29 Power spectral density curve; Re = 9800; heated inlet at 148 °F.

TABLE 4.1

Average Temperatures During Steady Flow Heating

Re = 9300

Ambient inlet at 65 °F

Heated inlet at 155 °F

Station	Average Temperature	
	°F	°C
A	117	47
A'	109	43
B	79	26
C	76	25
D	65	18
E	65	18
F	104	40

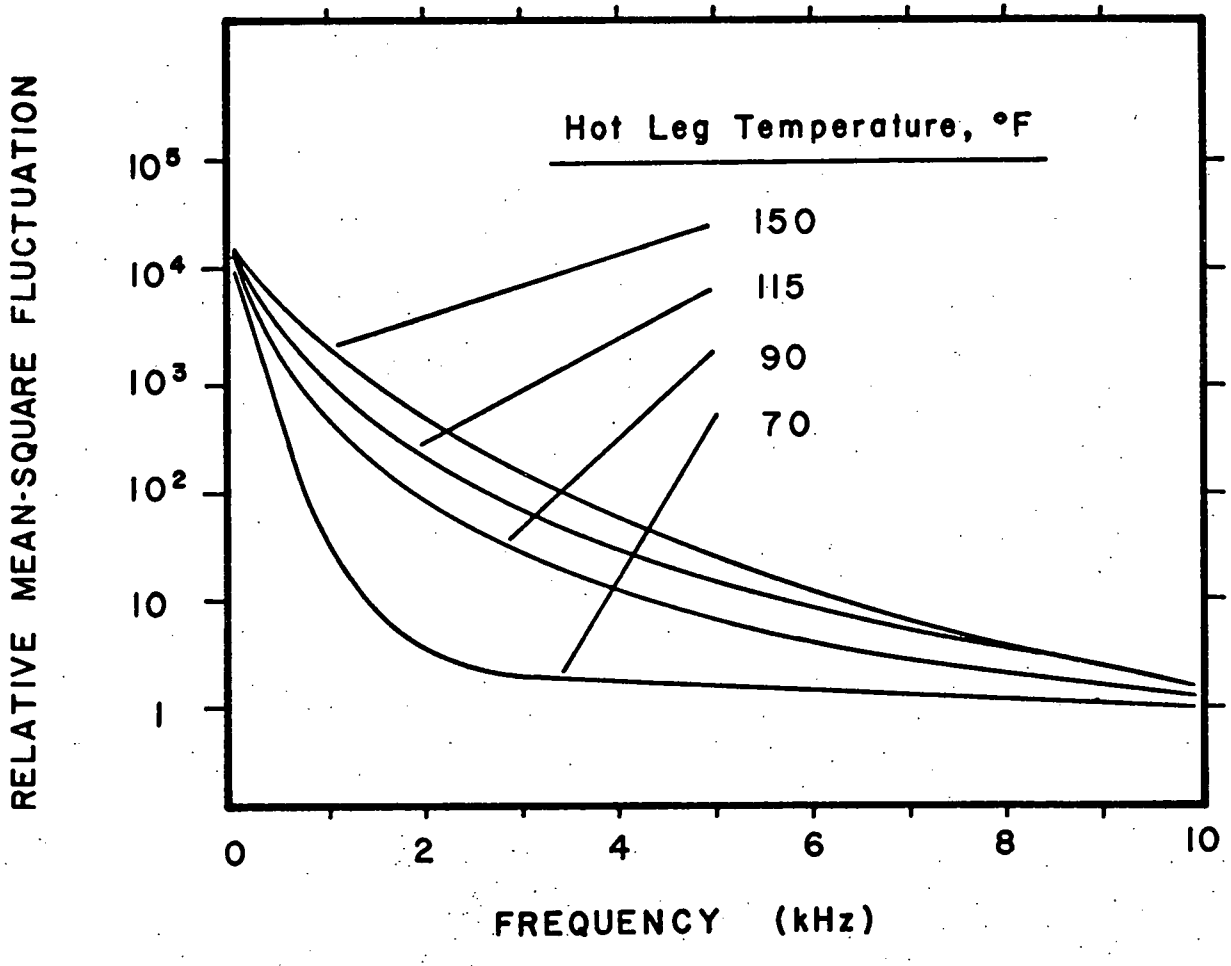

Fig. 4.30 Smoothed curves of the photographs of the relative RMS fluctuation, plotted as mean-square fluctuation. Bottom trace--background spectrum; upper traces--temperature spectra.

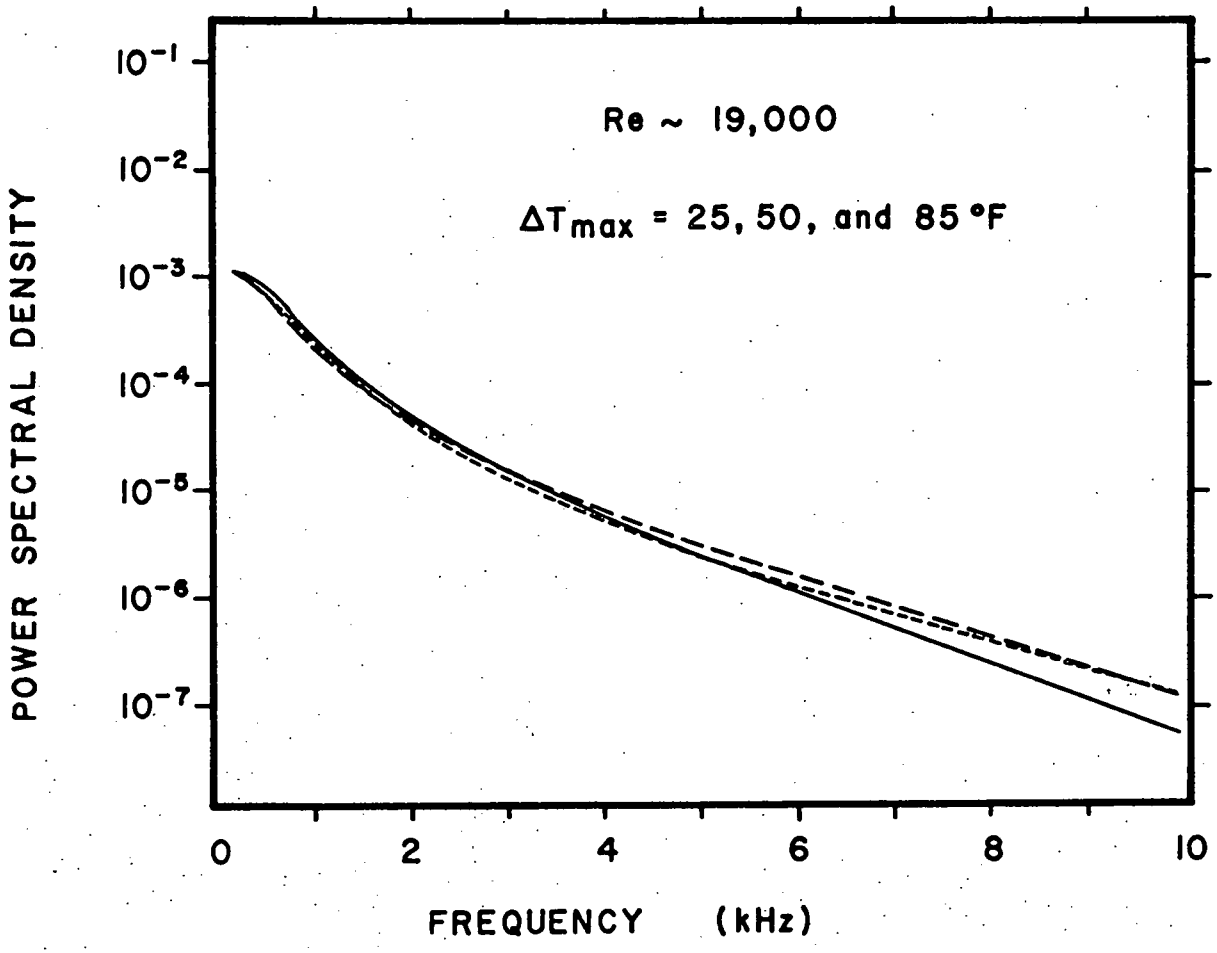

Fig. 4.31 Power spectral density curves at various inlet temperature upsets.

to unit area* has been regained in a different experiment. The spectrum analyzer is stopped at 1500 Hz, and is used to measure the value of the Fourier component at 1500 Hz for different values of the inlet temperature upset. This frequency is chosen becuase it occurs at the most sensitive (i.e., the highest signal to noise) portion of the technique. The output is smoothed for several seconds in an integrating circuit, and the resulting data is plotted against the applied temperature upset in Figure 4.32. Two separate regressions of the data are quoted on the figure. They indicate that the RMS fluctuation (at 1500 Hz) increases very nearly linearly with the temperature upset.

This result indicates an important trend of $\epsilon_{H1,1}$ (x_1 is taken horizontal, and parallel to the test cell faces). The definition in Eq. 1.1 can be redefined as:

$$\epsilon_{H1,1} = c_1(\underline{x})\sqrt{\langle v_1^2\rangle}\sqrt{\langle T^2\rangle}\Big/\left\langle \partial T/\partial x_1 \right\rangle \qquad (4.1)$$

where $c_1(\underline{x})$ is the correlation coefficient of temperature and the x_1 component of velocity. Separating the RMS magnitudes of the fluctuations from the correlation coefficient in the numerator allows the correlation coefficient to be interpreted in a simple way. The correlation coefficient is zero

---

* The PSD curves have unit area by convention.

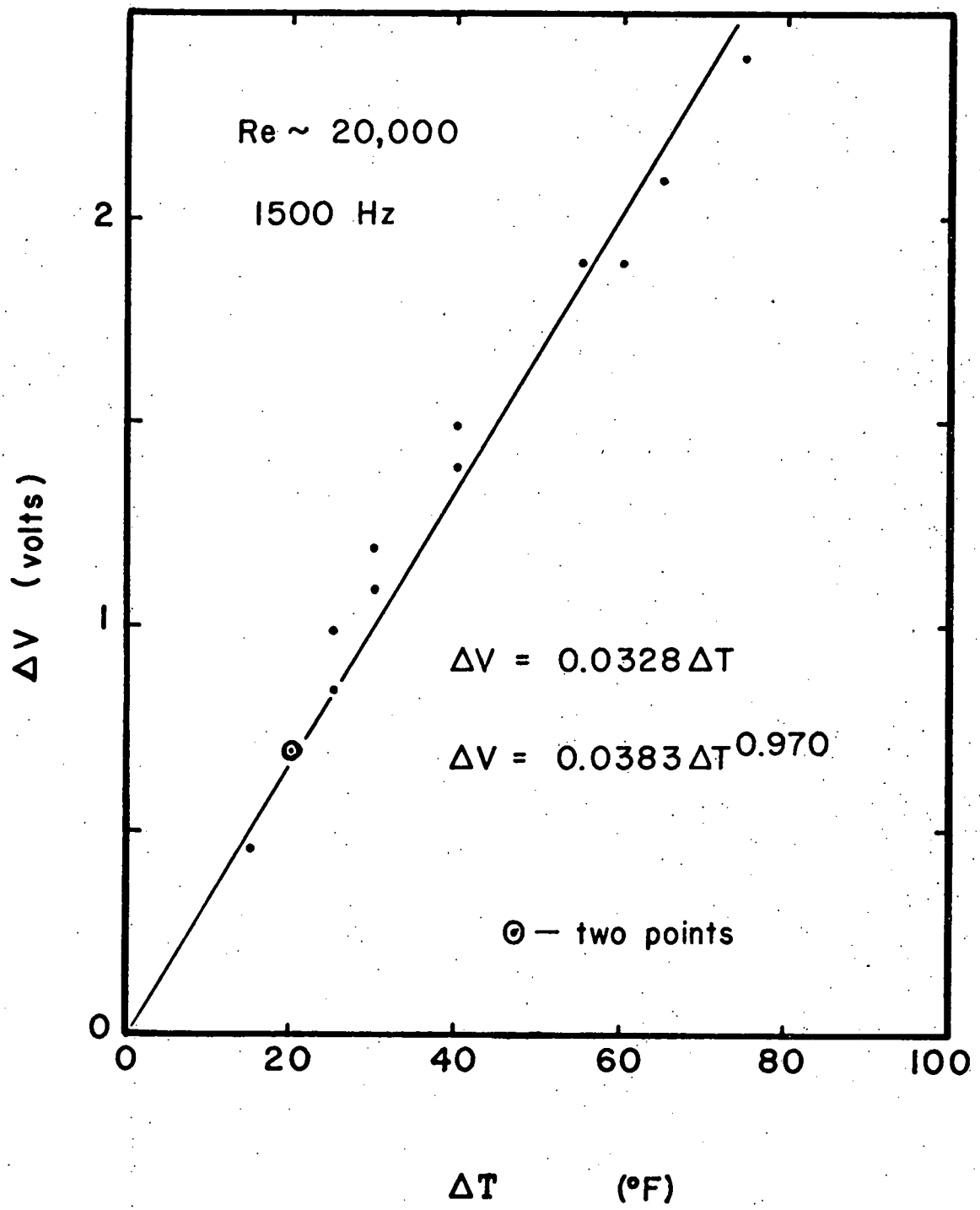

Fig. 4.32 Variation of the RMS fluctuation (measured as ΔV) in the temperature signal at 1500 Hz with applied temperature upset, ΔT. The data is modeled by the two different formulas.

when T and v_1 are totally uncorrelated, and it is equal to one when they are perfectly correlated. This correlation coefficient should not depend on the RMS temperature fluctuations, inasmuch as the temperature does not measurably affect the turbulent mixing. The denominator can be approximated as $\Delta T/S$ in the horizontal direction across the width of the shear layer, S, where ΔT is the inlet temperature upset. Again, S should not depend upon the RMS temperature fluctuations, since the temperature does not measurably affect the turbulently mixing. Experimentally, it is seen that $\sqrt{\langle T^2 \rangle} \sim \Delta T$, which uncouples the 1,1 component of the eddy diffusivity of heat from the inlet temperature upset--at least at stations similar to station A.

4.2.4 Effect of Increasing Reynolds Number

The qualitative effect of the Reynolds number on the PSD is found by comparing Figures 4.25 and 4.31. By doubling the Reynolds number, the high frequency tail of the PSD is extended. This agrees with an intuitive picture of the turbulence, where a higher Reynolds number corresponds to more fine-scale fluctuations in the flow.

5. CONCLUSIONS

1. The temperature measurement method presented in this work is an effective, and potentially, a very accurate way to implement an unintrusive turbulent temperature measurement.
2. The accuracy of the temperature analog, in its linear region, is about ± 5 ^{o}F (3 ^{o}C), with most of the noise originating from building vibrations and room noise affecting the interferometer. The accuracy may be improved in a straightforward manner, by seeking a quieter room, and by upgrading the optical bench.
3. The frequency response of the temperature analog is limited only by the choice of the photodetector.
4. The results demonstrate that the temperature upset in the test cell does not drive any instabilities in the flow. In effect, the temperature serves only to "color in" the turbulent mixing that is driven almost solely by the shearing of the inlet flows.
5. The fluctuating temperature has a strong position dependence in the test cell. A large 300 Hz component in the power spectral density is generated in the inlet shearing layer, and it decays as the flow progresses.
6. The results of Section 4.2.3 indicate that the eddy diffusivity of heat is independent of the temperature upset, at least at the point that has been investigated in the inlet region.

7. No information has been obtained about the position dependence of the eddy diffusivity of heat, or about its relation to the eddy diffusivity of momentum. Combined velocity and temperature measurements are needed for this.

8. It is recommended that in future experiments, the hot and cold inlet flows be switched. The central 2 in. inlet would be held at ambient air temperature, and the two 1 in. outer inlets would be heated. This will produce an unsteady density distribution in the test cell, and should further enhance the effect of the temperature upset on the turbulent mixing.

6. AN ADVANCED DESIGN

An untested design is proposed here to set the drift, vibration, and wall heating problems to rest. The system shown in Fig. 6.1 acts like two separate interferometers--one is tucked inside the other. The inner interferometer has an extremely narrow field, exactly like the one in this work. Its output intensity is reflected out of the wide beam by a very small mirror (say the polished end of a wire), onto detector #1. The outer interferometer is a field-widened system, with a field that is much larger than the characteristic wavelengths of the finest fluctuations in the flow. Such a field might be several inches in diameter. Both of the interferometers occupy the same four basic optical components. Thus, the outer interferometer experiences all of the same phase fluctuations as the inner interferometer except for the turbulence, which is spatially averaged by the optics of detector #2. One of the mirrors is mounted on a piezoelectric transducer (PZT), which controls the path length of the reference arm. Several standard fringe-following techniques are available[18,19,20,21] to control the PZT with the output of the outer, field-widened interferometer. In this way, most of the phase variation that is not due to the fluctuating temperature is subtracted from the inner interferometer--including the exact bench vibrations. The wall heating would not be exactly counteracted, inasmuch as the

wall heating is not uniform over several inches.

In this design, the average temperature of the flow is still lost (it gets subtracted away by the feedback system), but the fluctuating temperature stays right side up because the system is never allowed to drift onto the next fringe. More importantly, the output of the inner interferometer is very nearly a pure analog of the fluctuating temperature, at any frequency.

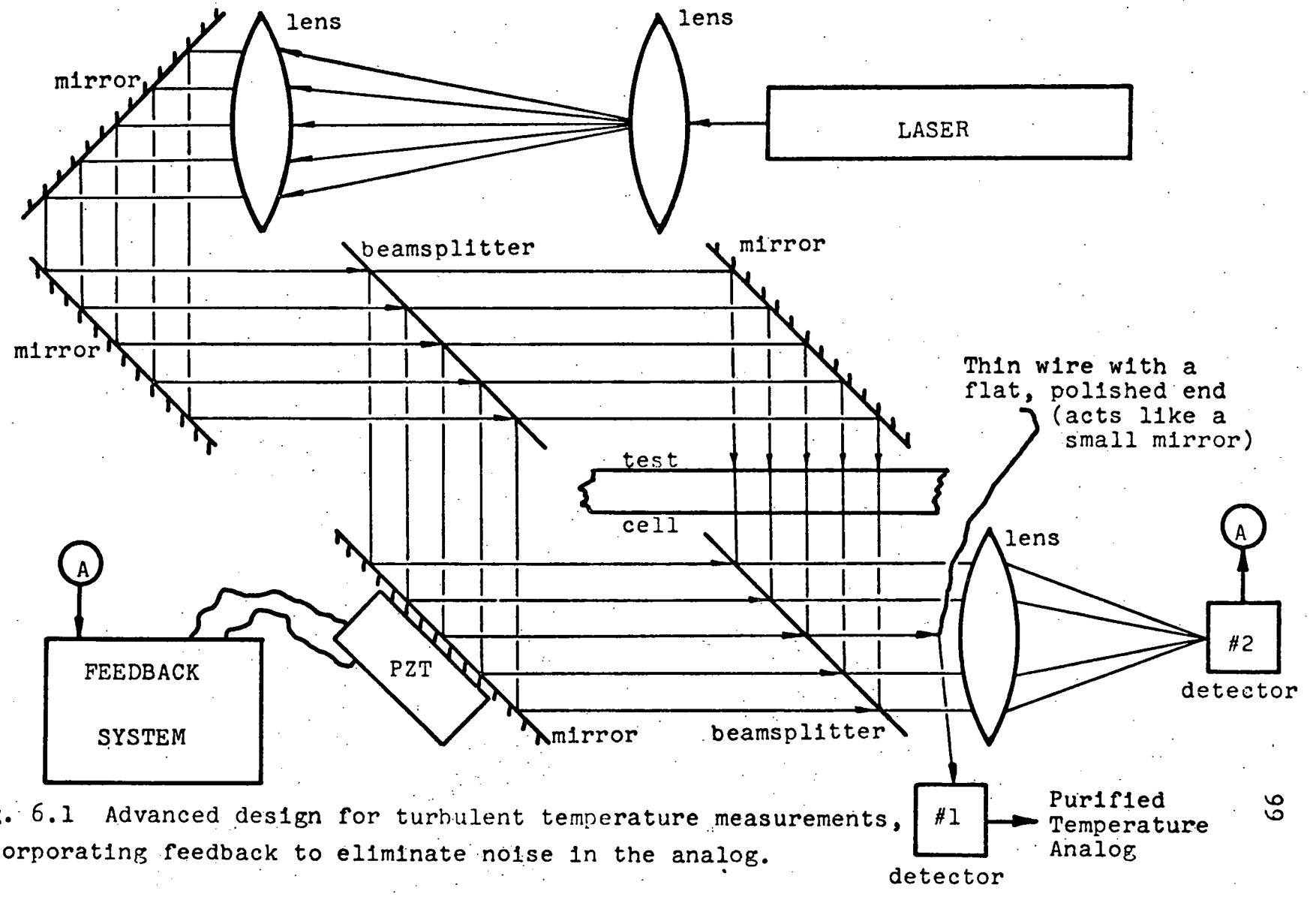

Fig. 6.1 Advanced design for turbulent temperature measurements, incorporating feedback to eliminate noise in the analog.

APPENDIX

Listing of the Computer Program that Calculates the Autocorrelation of the Temperature Analog

The program rejects the first moment of the data, and then samples the data two points at a time--the points are separated in time by τ, the autocorrelation variable. AVAUTO is the autocorrelation function, and SAMPLS is the number of pairs of points used to construct the autocorrelation.

```
      REAL MEANSQ
      INTEGER TAU,SAMPLS
      DIMENSION TEMP(200),AUTO(200),NTEMP(200)
      READ (5,100) (NTEMP(I),I=1,200)
  100 FORMAT (40I2)
      AVG=0.
      SUM=0.
      DO 5 I=1,200
    5 SUM=SUM+NTEMP(I)
      AVG=SUM/200
      DO 10 I=1,200
   10 TEMP(I)=NTEMP(I)-AVG
      SUMSQ=0.
      DO 15 I=1,200
   15 SUMSQ=SUMSQ+TEMP(I)**2
      MEANSQ=0.
      MEANSQ=SUMSQ/200
      WRITE (6,200) MEANSQ,AVG
  200 FORMAT ('1MEANSQ = ',F5.2,'  AVG = ',F5.2,'0')
      WRITE (6,250) (TEMP(I),I=1,200)
  250 FORMAT (5F10.3)
      WRITE (6,275)
  275 FORMAT ('1       TAU    AVAUTO      SAMPLES')
```

```
      DO 20 J=1,199
      TAU=J
      SAMPLS=200-J
      DO 25 K=1,SAMPLS
   25 AUTO(K)=TEMP(K)*TEMP(K+TAU)/MEANSQ
      AVAUTO=0.
      DO 30 L=1,SAMPLS
   30 AVAUTO=AVAUTO+AUTO(L)
      AVAUTO=AVAUTO/SAMPLS
   20 WRITE (6,300) TAU,AVAUTO,SAMPLS
  300 FORMAT (I10,F10.5,I10)
      STOP
      END
```

REFERENCES

1. K. Johannsen, "Heat Transfer Analysis of Reactor Fuel Rod Bundles," Notes E.1-4, MIT Course 22.313, Spring, 1975, p. 8.

2. M. Born, and E. Wolf, Principles of Optics, Fifth Ed., Pergamon, New York, 1975.

3. D.J. Hayes, "Instrumentation for Liquid Sodium in Nuclear Reactors," Jour. Phys. E, 7:69, Feb., 1974.

4. G. Hughes, "Detection of Rapid Electrical Conductivity Fluctuations in High Temperature Liquid Metals," Jour. Phys. E, 5:349, April, 1972.

5. J.C. LaRue, T. Deaton, and C.H. Gibson, "Measurement of High-Frequency Turbulent Temperature," Rev. Sci. Instr., 46:757, June, 1975.

6. R.W. Oliver, and A. Stott, "An Optical Thermometer: the Design, Construction and Calibration of a Photometric Temperature Scale for use with a Thermometric Solution," Jour. Phys. E, 7:275, April, 1974.

7. R.S. Hickman, and L. Liang, "A Comparison of Temperature Measurement of Oxygen in the 0-0 and 0-1 Rotational Bands using Laser Raman Spectroscopy," Rev. Sci. Instr., 45: 1580, Dec., 1974.

8. R.G. Bennett, and M.W. Golay, "Development of an Optical Method for Measurement of Temperature Fluctuations in Turbulent Flows," Trans. ANS, TANSAO 22:581 Nov., 1975.

9. A. Miller, E.K. Hussmann, and W.L. McLaughlin, "Interferometer for Measuring Fast Changes of Refractive Index and Temperature in Transparent Liquids," Rev. Sci. Instr., 46:1635, Dec., 1975.

10. W.E. Forsythe, Smithsonian Physical Tables, Ninth Ed., Washington, D.C., Smithsonian Inst., 1956, Tables 553 and 554.

11. G.E. Fishter, "Refractometry," in Applied Optics and Optical Engineering, Vol. IV, R. Kingslake, ed., Academic Press, New York, 1967, pp. 375ff.

12. A.H. Cook, The Interference of Electromagnetic Waves, Clarendon Press, Oxford, 1971, pp. 78ff.

13. F.D. Bennett, and G.D. Kahl, "A Generalized Vector Theory of the Mach-Zehnder Interferometer," J. Opt. Soc. Am., 43:71, Feb., 1953.

14. J.R. Meyer-Arendt, Introduction to Classical and Modern Optics, Prentice-Hall, Englewood Cliffs, N.J., 1972, pp. 225-228.

15. Ibid., p. 319.

16. R.L. Boxman, "Interferometric Measurement of Electron and Vapor Densities in a High Current Vacuum Arc," MIT Department of Electrical Engineering PhD Thesis, 1973.

17. H. Tennekes, and J. Lumley, A First Course in Turbulence, MIT Press, Cambridge, Mass., 1972, pp. 210ff.

18. F. Keilmann, "Infrared Interferometer with Output Proportional to Phase," Infrared Phys., 10:97, 1970.

19. G. Bouricius, and S. Clifford, "An Optical Interferometer Using Polarization Coding to Obtain Quadrature Phase Components," Rev. Sci. Instr., 41;1800, Dec., 1970.

20. M. Lavan, et. al., "Heterodyne Interferometer to Determine Relative Optical Phase Changes," Rev. Sci. Instr., 46:525, May, 1975.

21. T. Sato, et. al., "High-Speed Fringe Follower for Interferometry," App. Opt., 11:2918, Dec., 1972.